CHARACTERIZATION OF TWO NEW CLASSES OF PERIPLASMIC FERRIC BINDING PROTEINS

by

Stacey Anne Lisa Tom-Yew

B. Sc. The University of British Columbia, 2001

A THESIS SUBMITTED IN PARTIAL FULFILLMENT OF

THE REQUIREMENTS FOR THE DEGREE OF

DOCTOR OF PHILOSOPHY

in

THE FACULTY OF GRADUATE STUDIES

(Microbiology and Immunology)

THE UNIVERSITY OF BRITISH COLUMBIA

(Vancouver)

December, 2008

© Stacey Anne Lisa Tom-Yew, 2008

Abstract

Pathogenic bacteria acquire essential iron using specialized iron acquisition systems, such as the FbpABC transport system. The periplasmic FbpA protein delivers iron to the ABC transporter. FbpA proteins have two domains with the iron binding site located at the domain interface. A flexible inter-domain hinge region facilitates substrate dependent conformations. In general, the closed conformations are observed for holo FbpA proteins whereas the apo proteins exhibit increased hinge motion relative to the closed conformation. Closed conformations are likely important for initiating iron translocation across the inner membrane permease. Important bacterial pathogens such as *Campylobacter jejuni* and *Bordetella pertussis* contain previously uncharacterized FbpA proteins.

Using phylogenetic analyses, six FbpA classes were defined which vary in conservation of iron site ligands and utilization of a synergistic anion. Class I includes the anion-dependent *neisserial* FbpA (nFbpA). This thesis characterizes the Class III FbpA from *Campylobacter jejuni* (cFbpA) and the Class II FbpA from *Bordetella pertussis* (bFbpA). Visible spectroscopy showed high affinity iron binding of cFbpA. X-ray crystallography showed anion-independent iron coordination by cFbpA using a histidine and four tyrosine residues. Conformational analyses in solution by small angle x-ray scattering (SAXS) showed that cFbpA undergoes limited hinge motion in solution upon substrate binding. Furthermore, an iron uptake role is supported as a *cfbpA* deletion strain, constructed from *C. jejuni* 81-176, exhibited impaired growth under iron-limited conditions. Characterization of bFbpA by visible spectroscopy showed high affinity iron binding with carbonate, citrate and oxalate. Distinct holo conformations compared with

the apo conformation were observed for bFbpA depending on the synergistic anion. The closed conformation holo bFbpA crystal structure shows iron coordination by carbonate and three tyrosine residues. SAXS analyses also showed that oxalate and citrate treated holo bFbpA exhibit distinct conformations from apo bFbpA in solution. Furthermore, bFbpA undergoes large hinge motion in solution similar to nFbpA. Models for iron transport are proposed in which these holo complexes of bFbpA and cFbpA are candidates for initiating productive interactions with the permease.

Table of Contents

Abstract ii
Table of Contents iv
List of Tables vii
List of Figures and Illustrations viii
List of Symbols, Abbreviations and Nomenclature x
Acknowledgements xii

CHAPTER ONE: INTRODUCTION 1
1.1 The importance of iron for life 1
1.2 Iron availability 1
1.3 Iron acquisition systems in Gram-negative bacteria 2
1.3.1 PBP-dependent ABC transport systems 3
1.3.1.1 Overall structures of periplasmic binding proteins 5
1.3.1.2 Periplasmic binding proteins containing an α-helix hinge 5
1.3.1.3 Periplasmic binding proteins containing a β-strand hinge 7
1.4 Characterized FbpABC transport systems in bacteria 10
1.5 Characterization of FbpA 11
1.5.1 Closed conformation holo FbpA crystal structures 11
1.5.2 Elongated conformation FbpA crystal structures 12
1.5.3 Conformations of FbpA in solution 12
1.5.4 Visible spectroscopic properties of iron binding by FbpA proteins 13
1.5.5 High affinity iron binding by FbpA proteins 15
1.5.6 Effect of synergistic anions on iron binding by nFbpA 15
1.5.7 Effect of synergistic anions on iron release by nFbpA 17
1.5.8 Contribution of protein ligands and anion to iron transport by hFbpA 17
1.5.9 Proposed mechanisms for iron translocation by anion-dependent FbpAs 19
1.5.9.1 Conformation-dependent mechanism 19
1.5.9.2 Reductase mediated iron transport mechanism 20
1.5.9.3 Conformation and anion-independent mechanism 21
1.6 *Campylobacter jejuni* 22
1.6.1 *C. jejuni* iron acquisition systems 23
1.7 *Bordetella pertussis* 25
1.7.1 *B. pertussis* iron acquisition systems 26
1.8 Objectives of my Ph.D. thesis 29

CHAPTER TWO: MATERIALS AND METHODS 31
2.1 Chemical supplies and media 31
2.2 Bacterial strains and plasmids 32
2.3 Phylogenetic analyses 36
2.4 DNA manipulation 36
2.5 Protein expression and purification 40
2.6 Protein characterization 41
2.7 Iron binding analyses by visible spectroscopy 42
2.8 X-ray crystallography 44
2.8.1 cFbpA structures 44

2.8.2 bFbpA structures 46
2.9 Solution structure of cFbpA and bFbpA protein samples 48
2.9.1 Preparation of protein samples. 48
2.9.2 Small angle x-ray scattering 49
2.10 Function of cFbpA within *C. jejuni* 81-176 51
2.10.1 *C. jejuni* growth conditions 51
2.10.2 Transcription of cfbpA'ABC in *C. jejuni* 81-176. 52
2.10.3 Construction of the *C. jejuni* 81-176 cfbpA targeted deletion mutant (ΔcfbpA). 53

CHAPTER THREE: ANION-INDEPENDENT IRON COORDINATION BY THE *CAMPYLOBACTER JEJUNI* FERRIC BINDING PROTEIN 55
3.1 Introduction 55
3.2 Results 55
3.2.1 The 'as isolated' holo cFbpA crystal structure 55
3.2.2 Iron-binding 65
3.2.3 Sequence analyses 65
3.3 Discussion 72
3.3.1 Crystallographic characterization of iron transport proteins 72
3.3.2 The role of the synergistic anion in FbpA proteins 73
3.3.3 Anion-independence of cFbpA 74
3.3.4 Phylogenetic characterization of FbpA proteins 75
3.3.5 Subsequently characterized anion-independent FbpA proteins 79

CHAPTER FOUR: SMALL HINGE MOTION BY THE ANION-INDEPENDENT FERRIC BINDING PROTEIN FROM *CAMPYLOBACTER JEJUNI* 81
4.1 Introduction 81
4.2 Results 82
4.2.1 cfbpA'ABC transcription as an operon in *C. jejuni* 81-176. 82
4.2.2 Construction and verification of non-polar mutation of the ΔcfbpA strain 82
4.2.3 Impaired growth of the ΔcfbpA mutant under iron limitation. 85
4.2.4 Iron-reconstituted cFbpA crystal structure. 85
4.2.5 SAXS analyses of cFbpA and nFbpA 90
4.3 Discussion 96
4.3.1 cFbpA facilitates iron uptake in *C. jejuni* 81-176 96
4.3.2 SAXS analyses of flexible proteins 97
4.3.2.1 Anion-independent cFbpA undergoes small hinge motion 98
4.3.2.2 Anion-dependent nFbpA undergoes large hinge motion 98
4.3.2.3 Suggested role for anion in conformation 99
4.3.3 Iron transport models for Class III cFbpA and Class I nFbpA 100

CHAPTER FIVE: INFLUENCE OF SYNERGISTIC ANIONS ON CONFORMATION OF THE FERRIC BINDING PROTEIN FROM *BORDETELLA PERTUSSIS* 104
5.1 Introduction 104
5.2 Results 104
5.2.1 Visible spectroscopic analyses of iron and anion binding 104

5.2.2 Estimation of high iron binding affinity by iron chelator competition experiments 105
5.2.3 Overall structure of bFbpA 107
5.2.4 Apo bFbpA crystal structure 111
5.2.5 bFbpA:Fe:oxalate crystal structure 111
5.2.6 bFbpA:Fe:carbonate crystal structure 117
5.2.7 SAXS analyses of bFbpA 120
5.3 Discussion 126
5.3.1 Anion-dependent bFbpA undergoes large hinge motion in solution 126
5.3.2 Conformational flexibility of bFbpA 127
5.3.3 Role of anion in conformation 127
5.3.4 Iron transport model for Class II bFbpA 128

CHAPTER SIX: OVERVIEW AND FUTURE DIRECTIONS 131
6.1 Classification of FbpA proteins 133
6.2 Conformational differences across FbpA Classes 134
6.3 FbpA mediated iron acquisition within bacteria 135
6.4 Future directions 136

REFERENCES 139
Appendix I: Co-authorship Statement 151

List of Tables

Table 2-1 Bacterial strains used in this study 33

Table 2-2 Bacterial plasmids and clones used in this study 34

Table 2-3 Primers used in this study 39

Table 3-1 Data collection and refinement statistics for cFbpA 59

Table 3-2 Geometry of the cFbpA chain A iron binding site. 60

Table 3-3 Ligand to iron bond distances in cFbpA chain A 63

Table 3-4 Selected conserved residues that are not directly involved in iron binding within the FbpA Classes 77

Table 4-1 Data collection and refinement statistics. 89

Table 4-2 Radii of gyration for the SAXS protein samples 91

Table 5-1 Multiwavelength anomalous dispersion (MAD) data collection statistics for SeMet labelled apo bFbpA 109

Table 5-2 Data collection and refinement statistics. 110

Table 5-3 Geometry of the bFbpA:Fe:oxalate iron site. 115

Table 5-4 Geometry of the bFbpA:Fe:carbonate iron site. 118

Table 5-5 Radii of gyration for the SAXS protein samples. 122

Table 6-1 Comparison of the iron binding characteristics of nFbpA, bFbpA and cFbpA. 132

List of Figures and Illustrations

Figure 1-1 Iron acquisition utilizing the PBP-dependent ABC transport system in Gram-negative bacteria. 4

Figure 1-2 Representative PBPs containing an interdomain α-helix or β-strand hinge..... 6

Figure 1-3 Substrate-dependent conformations of FbpA proteins due to hinge motion..... 8

Figure 1-4 Comparison of the iron binding sites of hFbpA, YfuA, FutA1, and mFbpA. 14

Figure 3-1 The crystal structure of cFbpA and comparison of the iron site to hFbpA and mFbpA..... 57

Figure 3-2 A stereoview of the cFbpA chain A iron binding site..... 61

Figure 3-3 The angle formed between the His14 imidazole plane and the line joining His14 NE2 of cFbpA chain A with iron. 64

Figure 3-4 Anion-independent high-affinity iron binding to cFbpA. 66

Figure 3-5 Unrooted tree of FbpA sequences generated with TREE-PUZZLE (132). 67

Figure 3-6 Neighbor joining tree produced from ClustalW (151). 69

Figure 3-7 Representative alignment of a subset of FbpA sequences from Classes I to VI. 71

Figure 4-1 Genomic context of *cfbpA* and construction of the Δc*fbpA* strain. 83

Figure 4-2 Southern blot analyses of *C. jejuni* 81-176 (WT) and *ΔcfbpA* strain..... 84

Figure 4-3 Impaired growth of the Δc*fbpA* mutant in biphasic MH-TV media plus desferal. 86

Figure 4-4 Least-squares superimposition of the N-terminal domains of holo cFbpA (1Y4T, chain A, cyan) and iron-reconstituted cFbpA (magenta). 87

Figure 4-5 A stereoview of the 5 protein ligands coordinating iron in iron-reconsituted cFbpA. 88

Figure 4-6 Guinier plots of apo and holo nFbpA and cFbpA. 92

Figure 4-7 Solution X-ray scattering of apo and iron bound nFbpA and cFbpA. 93

Figure 4-8 Comparison of theoretical scattering from crystal structures and *in silico* models (colored lines) with SAXS data (black lines) from nFbpA and cFbpA. 94

Figure 5-1 Iron binding properties of bFbpA:Fe:carbonate, bFbpA:Fe:oxalate, and bFbpA:Fe:citrate. 106

Figure 5-2 Least-squares superimposition of the N-terminal domains of apo bFbpA and bFbpA:Fe..... 108

Figure 5-3 Comparison of the iron binding sites of the crystal structures of A, apo bFbpA B, bFbpA:Fe:oxalate and C, bFbpA:Fe:carbonate and of D, a model based on SAXS data of a bFbpA:Fe:oxalate..... 112

Figure 5-4 Stereoviews of the iron binding sites of A, apo bFbpA B, bFbpA:Fe:oxalate and C, bFbpA:Fe:carbonate. 114

Figure 5-5 Experimental SAXS curves for bFbpA..... 121

Figure 5-6. Guinier plots of apo bFbpA, bFbpA:Fe:carbonate, bFbpA:Fe:oxalate and bFbpA:Fe:citrate. 123

Figure 5-7 Comparison of the theoretical scattering from crystal structures and *in silico* models (colored lines) with SAXS data (black lines) from bFbpA using Crysol (146). 125

List of Symbols, Abbreviations and Nomenclature

Å	Angstrom unit (1 Å = 0.1 nm)
alcABCDE	Biosynthesis pathway for the siderophore alcaligin in *B. pertussis*
ATP	Adenosine triphosphate
ABC transporter	ATP-binding cassette transporter
B- factor	Crystallographic thermal factor
bFbpA:Fe:carbonate	bFbpA treated with ferrous sulfate in the presence of ambient carbonate
bFbpA:Fe:citrate	bFbpA treated with Fe^{3+}-citrate
bFbpA:Fe:oxalate	bFbpA treated with Fe^{3+}-oxalate
BHI	Brain heart infusion media
bp	Base pairs
BSA	Bovine serum albumin
BtuF	Periplasmic binding protein for vitamin B_{12} from *E. coli*
CeuBCDE	Components for ABC transport system for enterochelin uptake in *C. jejuni*
CeuE	Periplasmic siderophore binding protein from *C. jejuni*
Δc*fbpA*	c*fbpA* targeted deletion mutant in *C. jejuni* 81-176
cfbpA'	Small ORF preceeding *cfbpABC*
CfhuABD	Ferrichrome uptake system in *C. jejuni*
CfrA	Outer membrane receptor for enterochelin uptake in *C. jejuni*
CFU	Colony forming units
ChaNR	Outer membrane associated heme binding lipoprotein and receptor for iron acquisition in *C. jejuni*
ChuABCD	ABC transport system for hemin uptake in *C. jejuni*
DIG	Digoxigenin
DSC	Differential scanning calorimetry
EDTA	Ethylenediaminetetraacetic acid
FbpA, prefixes: b, c, n, h, m	Periplasmic ferric binding protein, prefixes denote bacterial source. b, *B. pertussis*; c, *C. jejuni*; n, *N. gonorrhoeae*; h, *H. influenzae*; m, *M. haemolytica*
FbpB	Permease component of FbpABC transport system
FbpC	ATPase component of FbpABC transport system
FbpABC	FbpA-dependent ABC transport system
FhuD, FhuD2	Periplasmic component of ABC transport system for hydroxamate type siderophore uptake in *E. coli* (FhuD) and *S. aureus* (FhuD2)
FUR	Ferric uptake regulator
FutA1 (S. sp2)	Cytoplasmic FbpA from *Synechocystis* PCC 6803 encoded by *slr1295*
FutA2 (S.sp1)	Periplasmic FbpA from *Synechocystis* PCC 6803 encoded by *slr0513*
Fo, Fc	Observed and calculated structure factors
FPLC	Fast performance liquid chromatography

GBS	Guillain-Barré syndrome
H-bond	Hydrogen bond
HCl	Hydrochloric acid
HisJ	Periplasmic histidine binding protein in *Salmonella enterica* serovar *Typhimurium*
IPTG	Isopropyl β-D-1-thiogalactopyranoside
IsdE	Periplasmic heme binding protein from *S. aureus*
ITC	Isothermal calorimetry
Ka	Association constant
Kan	Kanamycin resistance gene
Kb	Kilobase pairs
LB	Luria-Bertani media
LOS	Lipooligosaccharide
LMCT	Ligand to metal charge transfer
MAD	Multi-wavelength anamolous dispersion
MBP	Periplasmic maltose binding protein
MEMα	Minimal essential media alpha
MH	Mueller-Hinton media
MH-TV	Mueller-Hinton media containing trimethoprim and vancomycin
NAD(P)H	Reduced form of Nicotinamide adenine dinucleotide phosphate
NTA	Nitrilotriacetic acid
OD_{600}	Optical density at 600 nm
OMP	Outer membrane protein
PBP	Periplasmic binding protein
PDB	Protein data bank
PhuT	Periplasmic heme binding protein from *P. aeruginosa*
PMSF	Phenylmethanesulphonyl fluoride
Q	Momentum transfer value
r.m.s.d.	Root mean squared deviation
SAXS	Small angle x-ray scattering
SeMet	Seleno-methionine
SDS-PAGE	Sodium dodecyl sulphate-polyacrylamide gel electrophoresis
ShuT	Periplasmic heme binding protein from *Shigella dysenteriae*
SSRL	Stanford synchrotron radiation laboratory
Tris	Tris(hydroxymethyl)aminomethane
UV	Ultraviolet
WT	Wild-type
YfuA	FbpA from *Y. enterocolitica*
2xYT	Yeast tryptone media

Acknowledgements

I would like to thank Dr. Michael Murphy for his supervision over the years. I am grateful to all of my committee members, Drs. Tom Beatty, Rachel Fernandez and Erin Gaynor for all of their advice and support. I also wish to especially thank Dr. Erin Gaynor who generously opened her lab to me and has offered valuable support for a substantial part of my thesis. I would like to thank Dr. Brian Shilton who collected the SAX data for me as well as provided SAXS resources and advice. I also wish to acknowledge Dr. John Smit for helpful discussions and the use of his lab equipment from time to time. I would also like to thank Dr. John Nomellini who was always willing to offer valuable cloning and PCR advice as well as share lab supplies and equipment. I am also grateful to all present and past members of the Murphy and Gaynor labs for their help and assistance.

Most importantly, I would like to thank my husband Mike, my parents, Jeffrey and Cecilia, and my brothers, James and Jonathan, for all of their love and support.

Chapter One: Introduction

1.1 The importance of iron for life

Iron acquisition is necessary for the survival of most organisms, including pathogens, due to the function of iron in metalloproteins for key processes including metabolism, electron transfer and oxidative stress (23). Iron is uniquely suited due to the redox potential of iron (+300 mV to -500 mV) (29). In metalloproteins, iron can therefore act as both an electron donor and acceptor.

1.2 Iron availability

Although iron is the fourth most abundant element in the Earth's crust, the amount of usable iron for organisms is limited. In aerobic and neutral pH environments, ferric ion (Fe^{3+}) is predominant and largely insoluble (10^{-18} M Fe^{3+} at pH 7, 10^{-8} M Fe^{3+} at pH 3) (23). Furthermore, within the biological environment, iron is toxic and can catalyze the formation of hydroxyl radicals via the Fenton reaction with hydrogen peroxide (59). Hence, intracellular iron is tightly regulated in organisms.

Within the human body, iron is further sequestered by host iron binding proteins (43). Iron is stored by ferritin within cells, especially in the liver, bone marrow and spleen (44). Haemoglobin and myoglobin utilize iron for the transport of oxygen (128). Iron is also sequestered by transferrin in the sera and lactoferrin in the mucosa (44, 160). Transferrins have two similar but not identical binding sites for iron with a binding constant of approximately 10^{20} M^{-1}, and exhibit surplus iron binding capacity since most of the transferrin in the host is not loaded with iron (123). Therefore, in addition to

distributing iron to various host cells for assimilation into proteins, by sequestering excess iron, transferrin also serves a host defense function (123).

1.3 Iron acquisition systems in Gram-negative bacteria

For pathogenic bacteria to grow and cause disease, iron must be acquired from host iron sources such as transferrin, hemoglobin and ferritin using specialized iron acquisition systems (23). Following entry into the human host, bacteria utilize a ferric uptake regulator (FUR) to up-regulate iron uptake systems and express virulence factors in response to iron levels (93). FUR senses extracellular iron levels indirectly by binding the available ferrous iron in the cytoplasm (93). The ability to exist as a monomer when iron-free and a dimer when iron-bound allows for regulation of genes in response to iron levels (93). Holo FUR binds to conserved DNA sequences called FUR boxes and typically acts as a repressor if the FUR box is located in the promoter region or as an activator if the FUR box is located upstream of the promoter region (93). For iron uptake systems, holo FUR acts as a negative regulator, allowing for up-regulation of iron acquisition systems when the cell is iron-limited (93).

The model for ferrous iron uptake is the FeoAB system from *Escherichia coli* (71) and *Salmonella enterica* serovar *Typhymurium* (154). In this model, ferrous iron diffuses across an outer membrane porin into the periplasm. FeoB, an inner membrane GTP binding protein, facilitates iron translocation across the inner membrane by an unknown mechanism (97). Currently, the function of FeoA is unknown.

As for the utilization of ferric iron complexes, iron uptake is facilitated by a combination of TonB-dependent outer membrane receptors and periplasmic binding protein (PBP)-dependent ATP-binding cassette (ABC) transporter systems. Additional iron uptake systems may also facilitate iron uptake, but are currently not well characterized. For example, obligate or opportunistic intracellular pathogens may utilize extracellular and periplasmic ferric reductases to facilitate iron uptake (101, 133). Furthermore, some bacteria may also acquire iron using homologs of the copper oxidase -dependent ferric uptake Ftr1p/Fet3p system of *Saccharomyces cerevisiae* (13, 112).

1.3.1 PBP-dependent ABC transport systems

The PBP-dependent ABC transport method is utilized to acquire iron from siderophores, low molecular weight Fe^{3+} iron chelators, and from host iron binding proteins such as haemoglobin, transferrin and lactoferrin (Figure 1-1) (123). Siderophores are secreted by bacteria to scavenge iron in the extracellular milieu from host iron sources *(23, 123)*. Outer membrane bacterial receptors bind the iron siderophore complexes or the host iron binding proteins and facilitate iron/iron complex transport across the outer membrane using energy transduced from the Ton system (123). The iron siderophore complex is translocated across the outer membrane intact (101) whereas free iron or heme is removed from the host iron binding proteins prior to translocation into the periplasm (123, 162).

Transport then proceeds from the periplasm to the cytoplasm by a PBP-dependent ABC transport system. The PBP is necessary for efficient iron or iron complex transport

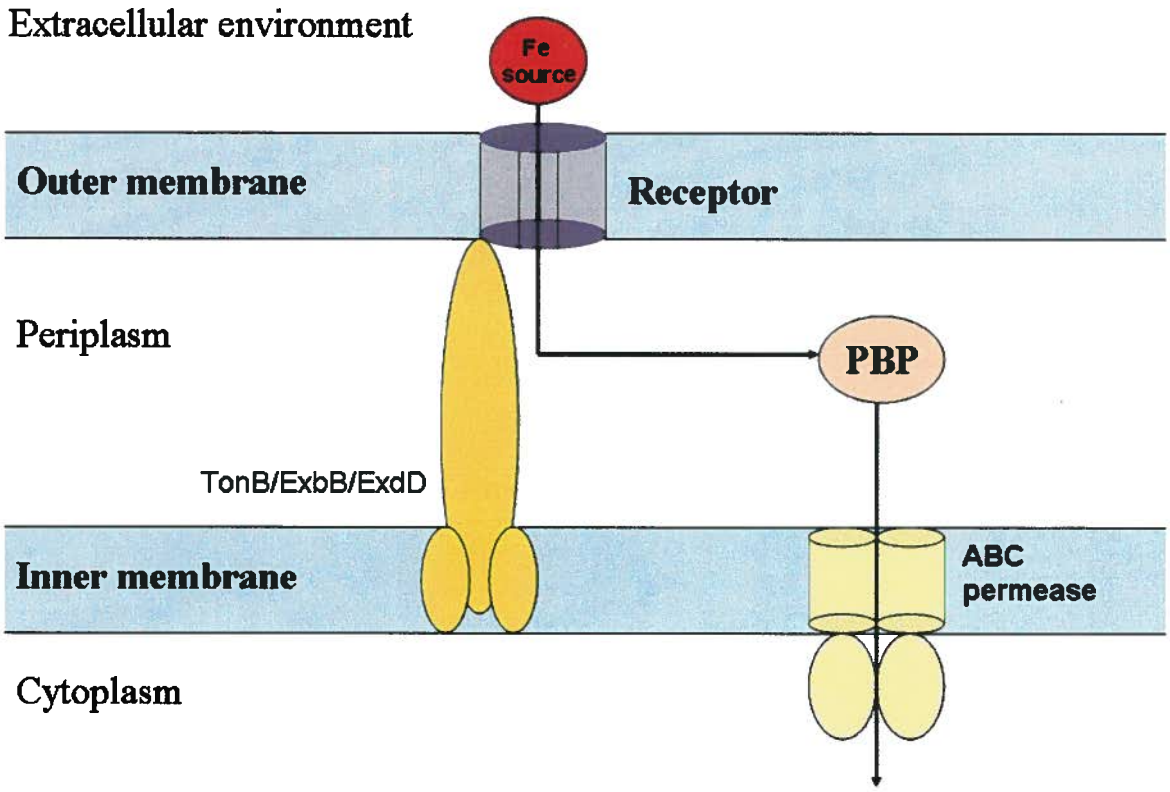

Figure 1-1 Iron acquisition utilizing the PBP-dependent ABC transport system in Gram-negative bacteria.

Following interaction of the iron source with the outer membrane receptor, the iron species is translocated (free iron, siderophore-bound iron, heme) across the outer membrane and into the periplasm. The PBP then binds and transports the iron species to the inner membrane permease for entry into the cytoplasm.

(123). The PBP binds the iron or iron complex and traverses across the periplasmic space to the inner membrane permease (ABC transport complex) (123). At the inner membrane, the holo PBP interacts productively with the permease, allowing for release of the iron or iron complex from the PBP for transport across the inner membrane (123, 134). The mechanism for translocation across the inner membrane is currently under investigation. Structural studies of PBPs yield insights into the mechanism of iron/iron complex transport (161).

1.3.1.1 Overall structures of periplasmic binding proteins

Common features of PBPs include two domains of similar topology connected by a hinge region with the substrate binding site located at the domain interface. Each domain consists of a central β-sheet flanked by α-helices and is an independent fold. The domains are connected by a hinge region within either two or three anti-parallel β-strands forming a small β-sheet or an α-helix (Figure 1-2).

1.3.1.2 Periplasmic binding proteins containing an α-helix hinge

Structurally characterized PBP members containing an interdomain α-helix hinge include the binding proteins of organic metal iron complexes such as the vitamin B_{12} binding protein (22), the siderophore binding proteins (CeuE from *Campylobacter jejuni* (104) and FhuD from *E. coli* (39)) and the heme binding proteins (PhuT from *Pseudomonas aeruginosa* and ShuT from *Shigella dysenteriae* (66)). Interestingly, the heme binding protein IsdE from the Gram positive *Staphylococcus aureus* is a PBP homologue and also exhibits an α-helix hinge (Figure 1-2, panel A) (56). Hinge motion is

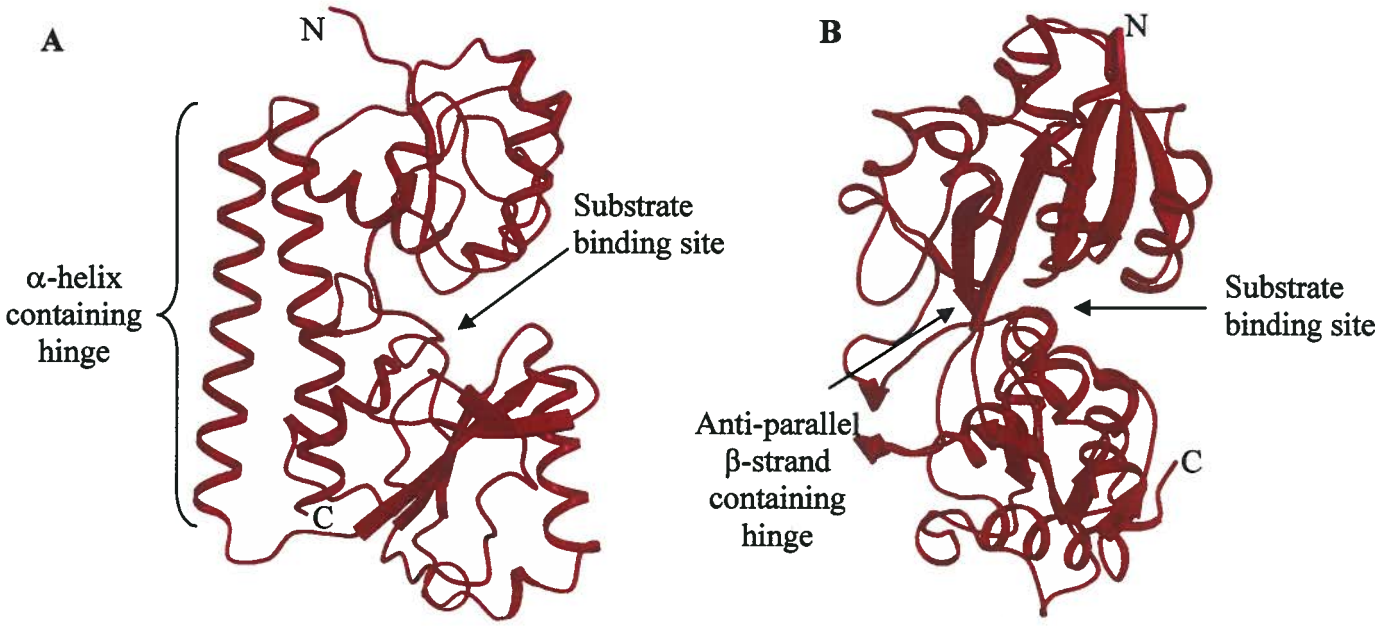

Figure 1-2 Representative PBPs containing an interdomain α-helix or β-strand hinge

A. Secondary structure of the heme binding protein IsdE (PDB ID 2Q8Q) from *Staphylococcus aureus* showing interdomain connection by an α-helix containing the hinge region. B. Secondary structure of the FbpA from *Haemophilus influenzae* (hFbpA) (PDB ID 1MRP) showing interdomain connection by two anti-parallel β-strands containing the hinge region. The images were generated using Molscript (87) and Raster3D (99).

proposed to be limited due to the rigidity of the α-helix. The limited hinge motion is also supported by molecular dynamics simulations of FhuD that show a 6° hinge motion (89).

1.3.1.3 Periplasmic binding proteins containing a β-strand hinge

PBPs containing a β-strand hinge region are further classified as either family 1 or family 2. Family 1 members are L-arabinose binding protein-like PBPs and are not known to transport iron or iron complexes. Family 2 members are phosphate binding protein-like PBPs and includes the ferric binding protein (FbpA) which is involved in iron transport (Figure 1-2, panel B). The domains of FbpA are connected by two anti-parallel β-strands which contain the hinge region, allowing for interdomain movement (161). Iron-bound (holo) FbpA typically exhibits a closed conformation (Figure 1-3 red), and in the absence of iron, the domains can move apart and exhibit an open conformation (Figure 1-3, blue).

Other members of the family 2 PBPs also exhibit substrate dependent conformations. For example, the well characterized maltose binding protein (MBP) exhibits a closed conformation when substrate bound and in the absence of substrate, the open conformation is observed due to hinge motion (149). These conformations have been observed both in crystal and in solution by small angle x-ray scattering (SAXS). The SAXS studies have additionally shown that apo MBP undergoes hinge motion in solution such that although the open conformation is dominant, sampling of the closed conformation is observed (122, 139, 149). These conformations are important for initiating and facilitating substrate transport across the inner membrane. The closed conformation allows for key residues from both domains of MBP to interact and initiate

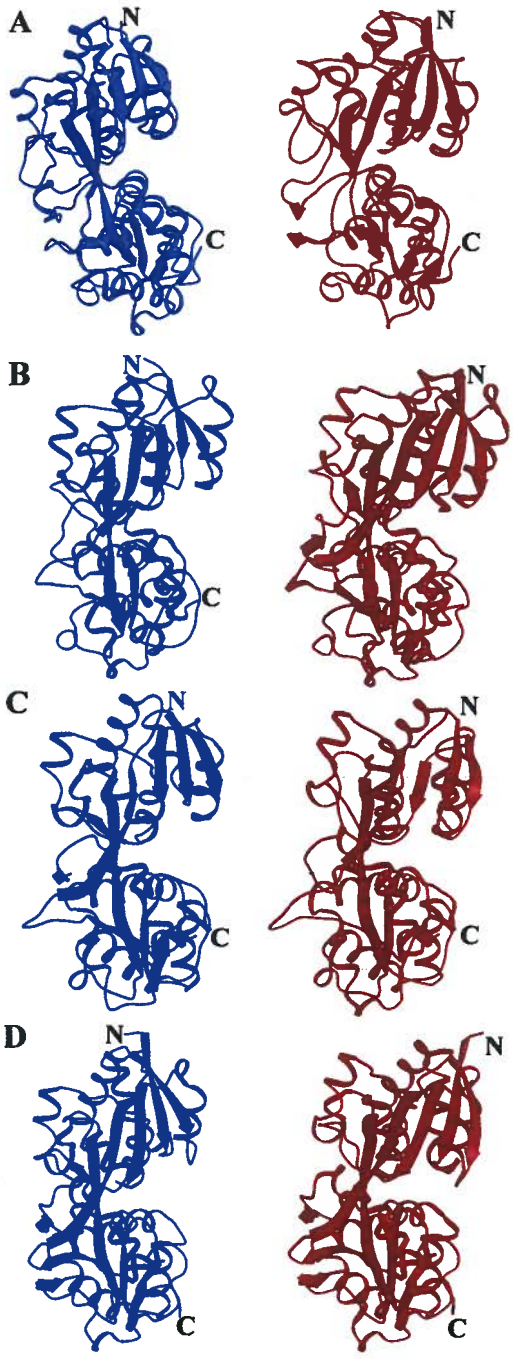

Figure 1-3 Substrate-dependent conformations of FbpA proteins due to hinge motion.

A, The open (PDB ID 1D9V) and closed (PDB ID 1MRP) conformations of FbpA proteins from *Haemophilus influenzae* (hFbpA). B, The open (PDB ID 2PT1) and closed (PDB ID 2PT2) conformations of FbpA from *Synechocystis* sp. PCC 6803 (FutA1). C, The open (PDB ID 2VOZ) and closed (PDB ID 2VP1) conformations of FbpA from

Synechocystis sp. PCC 6803 (FutA2). D, The open (PDB ID 1SI1) and closed (PDB ID 1SI0) conformations of FbpA from *Mannheimia haemolytica* (mFbpA). In all panels, the red crystal structures refer to the closed conformations. The blue crystal structures show interdomain separation due to hinge motion. The image was generated using Molscript (87) and Raster3D (99).

productive interactions with the permease (68). The open conformation facilitates substrate release to the permease for active transport across the inner membrane (111).

1.4 Characterized FbpABC transport systems in bacteria

Many bacteria, including pathogens, contain a FbpABC transport system. FbpA is the periplasmic component that is required for high efficiency iron uptake (77, 78) and is the initial iron acceptor protein in the periplasm (36). FbpB and FbpC comprise the permease and ATPase, respectively.

The FbpABC transport systems from *H. influenzae* (hFbpABC) and *Neisseria* sp. (nFbpABC) are the best characterized (1, 102). Reconstitution of the hFbpABC transport system in an *E. coli* strain deficient in siderophore production showed that the hFbpABC system was required for growth under iron limitation (1). In *H. influenzae*, the hFbpA and the hFbpC (ATPase) components were shown to be required for growth using transferrin as an iron source (78, 130). In *N. gonorrhoeae*, pulse chase experiments showed that the nFbpABC transport system was used to acquire radioactive iron from transferrin (36). nFbpC was shown to be a functional ATPase (92); however, nFbpC is not required for high affinity iron uptake suggesting that alternative ATPases may substitute for nFbpC (137). Recently in *C. jejuni*, the permease (cFbpB) was shown to be involved in iron acquisition from transferrin under iron limitation (103).

The FbpABC transport systems from the bacterial pathogens *Yersinia enterocolitica*, *Serratia marcescens*, *Actinobacillus pleuropneumoniae,* and *Mannheimia haemolytica* also facilitate iron acquisition; however, the iron sources have not been

identified. In *Y. enterocolitica*, the FbpA homologue (YfuA) was shown to facilitate iron uptake under iron-limiting conditions (80). As for the remaining bacteria, the FbpABC transport systems were reconstituted in *E. coli* strains and shown to support growth under iron limitation (8, 38, 79). Interestingly, the cyanobacteria *Synechocystis* sp. PCC 6803 also contains an FbpABC transport system shown to function in iron transport (72).

1.5 Characterization of FbpA

1.5.1 Closed conformation holo FbpA crystal structures

Native FbpA from *N. gonorrhoeae* as well as the recombinant FbpA protein isolated from the *E. coli* periplasm show iron bound in a 1:1 ratio with the protein (2, 129). Holo FbpA crystal structures in the closed conformation containing one bound iron are available for the FbpA proteins from *N. gonorrhoeae* (nFbpA), *H. influenzae* (hFbpA), *Y enterocolitica* (YfuA), *Synechocystis* sp. PCC 6803 (FutA1 and FutA2), and *M. haemolytica* (mFbpA) (Figure 1-3, red).

Similarities in iron coordination are observed for nFbpA, hFbpA and YfuA. The crystal structures of holo nFbpA (PDB ID 1D9Y) and holo hFbpA (PDB ID 1MRP) show iron bound in octahedral geometry by a histidine and a glutamate residue from the N-terminal domain and two tyrosine residues from the C-terminal domain. Completing the iron binding site is water and a phosphate synergistic anion (Figure 1-4, panel A). YfuA (PDB ID 1XVX) coordinates iron similarly to nFbpA and hFbpA using the same spatially equivalent residues. However, instead of a phosphate synergistic anion, an aspartic acid residue is used to coordinate iron (Figure 1-4, panel B).

As for the FbpA proteins from *Synechocystis* sp. PCC 6803 and *M. haemolytica*, differences in iron coordination are observed. FutA1 (PDB ID 2PT2) and FutA2 (PDB ID 2VP1) coordinate iron similarly in a distorted octahedral geometry, using a histidine and a tyrosine from the N-terminal domain, and three C-terminal domain tyrosine residues (Figure 1-4, panel C). mFbpA (PDB ID 1SI0) also coordinates iron in a distorted octahedral geometry; however, iron is coordinated using the three C-terminal domain tyrosine residues as observed in FutA1 and FutA2 and a synergistic carbonate anion. The N-terminal domain contributes indirectly to iron binding through hydrogen bonding with the carbonate anion (Figure 1-4, panel D).

1.5.2 Elongated conformation FbpA crystal structures

Compared with the closed conformation holo structures, additional crystal structures show interdomain separation due to rotation about the hinge region (Figure 1-3, blue). Relative to the respective closed conformation holo structures, the apo crystal structures of hFbpA, FutA1 and FutA2 show hinge angles of 20°, 16°, and 24°, respectively. Furthermore, an iron-bound mFbpA structure lacking the carbonate synergistic anion exhibits a hinge angle of 27° (Figure 1-3).

1.5.3 Conformations of FbpA in solution

Although crystal structures provide high resolution data, for proteins that can undergo large conformational changes such as the FbpA proteins, each crystal structure typically shows only one conformation that is accessible in solution.

The solution conformations have been characterized for nFbpA by trypsin digests and native gel electrophoresis. Limited proteolysis, using enzymes such as trypsin, have

been used to probe the conformational state of proteins in solution. Trypsin targets flexible regions and cleaves at the C-terminus of Lys and Arg residues. Following substrate binding, for proteins such as transferrin (28) and myoglobin (47), the regions susceptible to trysin digest in the apo form becomes more ordered and are therefore more resistant to trypsin digestion. For nFbpA, trypsin digests also showed that holo nFbpA is more resistant to trypsin digest compared with apo nFbpA, indicating a conformational change upon substrate binding (109).

Subsequent analyses of conformation were performed by native gel electrophoresis (17). In native gel electrophoresis, proteins retain conformational shape and migrate depending on charge and hydrodynamic size. Therefore, more compact conformations migrate faster on a native gel compared with elongated conformations. Phosphate-bound holo nFbpA migrated faster than apo nFbpA, showing that phosphate-bound holo nFbpA was more globular whereas apo nFbpA was more extended (17). Overall, these observations are consistent with the crystal structures showing closed conformations for holo FbpA proteins and more open and elongated conformations for the apo FbpA proteins; however, how well the available crystal structures represent conformations in solution is unknown.

1.5.4 Visible spectroscopic properties of iron binding by FbpA proteins

All of the FbpA proteins yield absorbance peak maxima in the 400 to 500 nm range, indicative of a ligand to metal charge transfer (LMCT), specifically a ferric iron:tyrosinate interaction (117). Phosphate-bound holo nFbpA and hFbpA gave absorbance peak maxima of approximately 480 nm (1, 108). All of the other FbpA

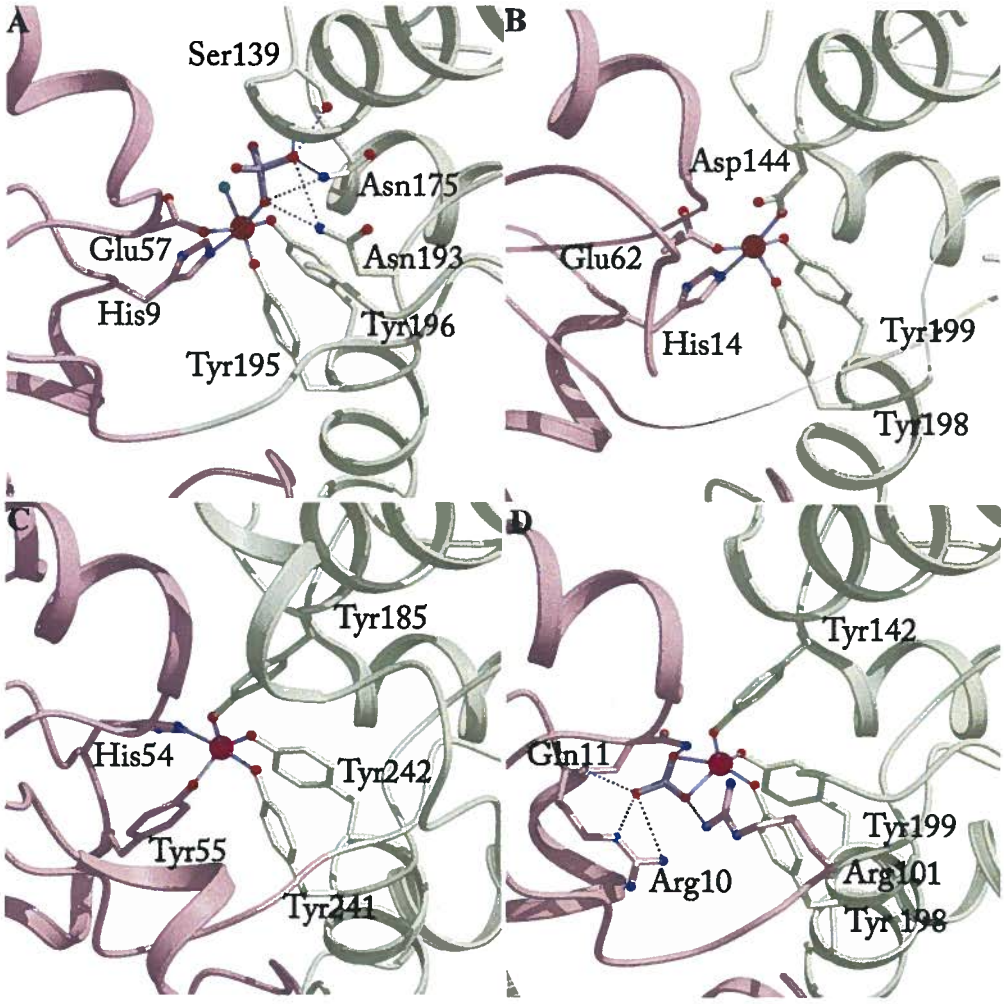

Figure 1-4 Comparison of the iron binding sites of hFbpA, YfuA, FutA1, and mFbpA.

A, hFbpA iron binding site. A water molecule is indicated by a green sphere. B, YfuA iron binding site. C, FutA1 iron binding site. D, mFbpA iron binding site. In all panels, the backbones of the N- and C- terminal domains are in light pink and khaki colours, respectively. H-bonds to the anion and ligand bonds to the iron atoms (red-pink spheres) are indicated by dotted and solid lines, respectively. The synergistic anions are coloured grey. The nitrogen and oxygen atoms of the residue side chains are coloured blue and red, respectively. The images were generated using Molscript (87) and Raster3D (99).

proteins yield significantly different absorbance peak maxima, reflecting altered ferric iron:tyrosinate bonds. Holo YfuA exhibits an absorbance maximum that is red shifted to 513 nm (142). Holo FutA1, holo FutA2 and holo mFbpA exhibit blue shifts in the absorbance maxima at 411 nm (86), 450 nm (12) and 419 nm (79), respectively.

1.5.5 High affinity iron binding by FbpA proteins

FbpA proteins bind iron with high affinity, similar to transferrin (36). The relative affinities for iron of the FbpA proteins have been estimated through competition with the low molecular iron-chelators (e.g. citrate) and monitoring iron removal by observing the decrease in absorbance peak by visible spectroscopy. By utilizing the iron binding affinity of the iron chelator (association constant (K_a) for citrate at pH 8 is10^{17} M^{-1}) and observing the concentration of chelator needed to remove 50% of the iron from FbpA at the same pH, the association constants for nFbpA, hFbpA, mFbpA and FutA1 were estimated at between 10^{18} and 10^{21} M^{-1} (1, 36, 42, 73, 79). For nFbpA, high affinity iron binding has also been demonstrated thermodynamically by isothermal titration (ITC) and differential scanning calorimetry (DSC) and similar binding constants are reported (17). For hFbpA, competitive iron binding experiments between holo and apo hFbpA also show similar high affinity iron binding (75).

1.5.6 Effect of synergistic anions on iron binding by nFbpA

In addition to phosphate, additional anions have also been shown to facilitate iron binding to nFbpA *in vitro*. Of the anions, phosphate is the most strongly bound anion, followed by arsenate, pyrophosphate, NTA, citrate, oxalate, and sulphate (42, 64). Holo nFbpA complexes with bound arsenate, pyrophosphate, NTA, citrate, oxalate and

sulphate exhibit different absorbance peak maximums between 468 and 495 nm (42, 64). Interestingly, unlike phosphate bound holo nFbpA which exhibits a more compact conformation in solution compared with apo nFbpA, native gel electrophoresis shows that NTA bound holo nFbpA exhibits an elongated conformation similar to apo nFbpA in solution (17).

Comparison of iron binding affinities of nFbpA in the presence and absence of phosphate obtained by ITC shows high affinity iron binding; however, phosphate increases the iron binding affinity by an order of magnitude (17). Interestingly, decreased iron binding affinity of approximately an order of magnitude was observed for anion binding nFbpA mutants exhibiting weaker phosphate binding (G140H and Q58R) compared with wild type nFbpA in the presence of phosphate (17).

As for the various holo nFbpA complexes, chelator competition experiments show high iron binding affinities that vary by over an order of magnitude with increasing iron binding affinity as the anion becomes more tightly associated with the protein (42, 64). In addition to modulating iron binding affinity, anions also affect the redox potential of the nFbpA complexes with redox potential increasing as anion affinity decreases (64).

Synergistic anions have also been proposed to have important roles in loading iron into nFbpA (48). In the presence of phosphate, the rate of iron loading of NTA chelated iron is increased, suggesting a catalytic role for phosphate in iron insertion. Mechanistically, phosphate is proposed to bind the anion binding site in the C-terminal domain, forming a transition-state-like structure for iron binding.

1.5.7 Effect of synergistic anions on iron release by nFbpA

The synergistic anion acts as a gatekeeper for iron release by modulating the rate of iron release (20, 41). In stopped flow pH jump measurements, protonation and release of the synergistic anion preceded iron release (20). Iron-chelator competition experiments using EDTA also showed that the synergistic anion is released prior to iron (41). Using the iron-chelator tiron, the identity of the synergistic anion was also observed to influence the rate of iron release, since tiron attacks the iron directly and is unable to act as a synergistic anion, unlike EDTA, which forms an EDTA-bound holo nFbpA intermediate (20, 41). Compared with phosphate-bound holo nFbpA, NTA-bound holo nFbpA was more labile (41).

1.5.8 Contribution of protein ligands and anion to iron transport by hFbpA

The contribution of each of the iron binding protein residues of hFbpA as well as the synergistic anion phosphate to iron transport was investigated (75, 76). hFbpA mutants of the iron (H9Q, H9A, E57A, Y195A, Y196A) and anion binding residues (Q58L, N175L, N193L) were constructed and mutants were analyzed by x-ray crystallography and in an *H. influenzae* bioassay (75, 76).

All of the hFbpA mutants exhibited high affinity iron binding in the order of WT=Q58L= N175L=N193L>H9Q>H9A=E57A>Y195A=Y196A as examined by citrate competition and competitive iron binding experiments between holo hFbpA and apo proteins (75, 76). All of the anion binding mutants bound iron with similar affinity to wild type hFbpA. Of the remaining protein residue mutants, the N-terminal domain mutants exhibited higher binding affinity compared with the C-terminal domain mutants.

The conservative mutation H9Q exhibited the next highest iron binding affinity, followed by H9A and E57A mutants which exhibited similar iron binding affinity. Mutation of each of the C-terminal domain tyrosine residues resulted in the most impaired iron binding ability.

Available crystal structures of the holo FbpA mutants exhibited hinge motions ranging from 20° to 22° (75, 76). The E57A and the Q58L mutants bound iron in the C-terminal domain using the two C-terminal domain tyrosine residues and phosphate (75). The N193L mutant bound iron using the two C-terminal domain tyrosine residues and exhibited no phosphate binding (76). The H9Q mutant bound iron using the two C-terminal domain tyrosine residues and an EDTA molecule introduced during the purification process (140). In the H9A and N175L mutants, the C-terminal domain binds ferric hydroxide clusters consisting of 3 and 4 ferric ions, respectively, with each of the tyrosine residues involved in binding a separate iron atom (143). In the H9A mutant, the iron cluster has two phosphate anions bound, of which one is located in the phosphate binding site and the other is located on the opposite side of the cluster (143). As for the N175L mutant, phosphate is not observed in the phosphate binding site but is located on the opposite side of the cluster, similar to the H9A mutant (143).

Growth under iron limited conditions showed that in addition to wild type hFbpA, only the conservative H9Q mutation and the anion binding mutations Q58L, N175L and N193L of FbpA could facilitate growth using transferrin as an iron source (75, 76). The other FbpA mutants involving mutations of the iron binding residues to Ala residues resulted in loss of growth using transferrin as an iron source (75). Growth on ferric citrate

was used to further elucidate the role of the iron site ligands. On iron limited media, growth of *H. influenzae* in less than 40 nmol ferric citrate requires a functional hFbpABC system (75). The H9A and the E57A hFbpA mutants were able to grow on 30 nmol ferric citrate, unlike the Y195A and the Y196A mutants (75). Overall, of the iron site ligands, the C-terminal tyrosine residues contribute the most to iron binding and transport in hFbpA.

1.5.9 Proposed mechanisms for iron translocation by anion-dependent FbpAs

1.5.9.1 Conformation-dependent mechanism

Although currently the mechanism for initiation of iron translocation through the permease is not known, iron transport may occur analogously to other better characterized ABC transport systems (69, 111). In this model, the closed conformation of the substrate bound PBP (holo FbpA) is important for initiating a productive interaction with the inner membrane permease prior to iron translocation across the inner membrane.

Support for this mechanism is derived from the classification of FbpA within family 2 of the PBP superfamily (148). Other members of this family 2, such as MBP and hisitidine binding protein (HisJ), also share a similar topology with FbpA including a hinge region consisting of either two or three β- strands.In the absence of substrate, PBPs such as MBP and HisJ typically exhibit open conformations and upon substrate binding, the domains rotate inwards to form a closed conformation (122, 139). For the maltose and histidine uptake systems, the closed conformations of the PBPs are important for interacting with the respective permeases, initiating ATP hydrolysis and facilitating substrate transport into the cell (37, 68, 94, 95, 166). By homology to PBP members, the

conformations of FbpA are likely to be important for initiating productive interactions with the permease (FbpB) and ATPase (FbpC) and facilitating iron transport.

1.5.9.2 Reductase mediated iron transport mechanism

This model proposes that iron transport across the inner membrane is facilitated by a reductase and synergistic anion exchange. This is due to the observation that nFbpA has an affinity for ferric iron that is 12 orders of magnitude greater than for ferrous iron (42). As well, all of the various anion-bound holo nFbpA complexes exhibit redox potentials greater than -300 mV, within the range of activity for NAD(P)H reductases.In addition, due to the proton motive force established by the electron transport chain, the local periplasmic micro-environment near the inner membrane is more acidic. The reduction in pH may facilitate iron transport through protonation of the iron site residues (144), increasing the redox potentials of the holo nFbpA complexes.

Furthermore, synergistic anion exchange has been proposed to facilitate iron transport across the inner membrane by allowing for more energy efficient ferric iron reduction and also for responding to the external environment (42). Since the identity of the bound synergistic anion influences iron binding affinities and redox potentials, synergistic anion exchange can destabilize the holo FbpA complex and provide the driving force for reduction of ferric iron to ferrous iron (42). The ability of nFbpA to bind a variety of synergistic anions is also proposed to be advantageous for utilizing available iron sources as the anion concentration of the periplasm likely reflects the external environment due to diffusion through outer membrane porins (42).

However, this mechanism has several drawbacks. One is the inability of cytoplasmic NAD(P)H and flavins to cross the inner membrane into the periplasm (101, 133). Alternatively, membrane bound ferric reductases or electron transfer proteins may be utilized; however, membrane bound ferric reductases facilitating extracellular or periplasmic reduction are currently not characterized in bacteria. Furthermore, electron transfer proteins mediating ferric reduction are yet to be identified (101, 133).

1.5.9.3 Conformation and anion-independent mechanism

In this model, iron translocation across the inner membrane relies primarily on differences in iron binding affinity between the open conformation of holo nFbpA and the permease (76). The permease is proposed to capture and stabilize an open conformation of holo nFbpA, prior to iron translocation. Furthermore, iron transport is not dependent on the presence of phosphate in the synergistic anion-binding site or the closed conformation of the holo protein (76).

This model was based on the results of the crystal structures of the hFbpA mutants of the iron and anion binding residues and the *H. influenzae* bioassay utilizing the hFbpA mutants (75, 76), as described in the contribution of protein ligands and anion to iron transport by hFbpA section. For this model to be supported, the conformations observed in the crystal structures of the hFbpA mutants, ranging from 20° to 22°, must represent the active conformations of the hFbpA mutants that facilitated growth in the *H. influenzae* bioassay. However, whether or not the crystal structures represented the active solution conformations in the periplasm is unknown.

1.6 Campylobacter jejuni

C. jejuni is a Gram-negative microaerophilic bacterium of the epsilon subdivision of proteobacteria. This bacterium is part of the normal intestinal flora of birds and other warm-blooded animals (33). In humans, however, *C. jejuni* is pathogenic and is the leading bacterial cause of human gastroenteritis in the developed world and a major cause of traveller's diarrhoea (153, 158). Currently, the reasons for the asymptomatic phenotype in birds versus disease phenotype in humans are unknown; however, the host immune response to *C. jejuni* infection has a role (165). Furthermore, infection of humans with *Campylobacter* sp. results in two disease manifestations, depending on socio-economic status which likely reflects the host immune status. In developing countries, watery diarrhoea is predominant, with illness more frequent in children through exposure to *C. jejuni* in contaminated water and contact with farm animals (33, 165). In industrialized countries, campylobacteriosis results in bloody diarrhoea and is usually the result of consumption of undercooked poultry (165). Although infection is rarely fatal in adults and is self-limiting, the course of infection lasts approximately a week with shedding of the organisms for a few weeks afterwards, leading to a considerable drain on the economy and public health resources (33). Furthermore, additional serious complications following infection include the post-infection development of autoimmune diseases such as Guillain-Barré syndrome (GBS) and acute motor axonal neuropathy (106).

Several factors have been shown to contribute to survival and pathogenesis of *C. jejuni* including motility, adhesion to and invasion across the intestinal epithelial cell

layer, and acquisition of iron (74, 165). Motility, provided by the polar flagella, is required to penetrate the mucus layer. The bacteria migrate towards more favourable oxygen levels (aerotaxis) and towards amino acids and components of the mucus layer (chemotaxis) (165). In chickens, the bacteria are primarily observed in the mucus layer (165). In the susceptible human host, following migration through the mucus layer, the bacteria are observed adhering to and invading the epithelial cell layer. The ability to invade the intestinal epithelial cell layer is correlated with the severity of disease presentation in humans (74). Invasion across the epithelial cell layer is facilitated by the flagella, which secrete the proteins FlaC and CiaB that are necessary for invasion, and also by additional surface components such as the lipooligosaccharide (LOS) and the capsule (165). Interestingly, these surface structures undergo phenotypic alterations that likely affect pathogenesis as well as immune evasion. For example, the flagellum undergoes phase variation allowing for a switch between non-motile aflagellated and motile flagellated states (63, 165). Furthermore, the LOS and capsule exhibits variability due to phase variation of the biosynthesis and modification genes (58, 165). Differences in invasive ability are also observed between *C. jejuni* strains. For example, the highly pathogenic strain *C. jejuni* 81-176 is highly invasive compared with other strains such as *C. jejuni* 11168 (10, 11).

1.6.1 C. jejuni iron acquisition systems

Following entry into the iron-restricted host environment, high affinity iron uptake systems are up-regulated by FUR in order to acquire the iron necessary for survival and colonization (107, 115). Bioassays, involving the feeding of iron sources to

C. jejuni strains seeded in iron restricted agar, showed the utilization of haemin, haemoglobin, hemin-hemopexin, haemoglobin-haptoglobin (118), enterochelin, ferrichrome (46), free ferrous and ferric iron (46). *C. jejuni* is also able to utilize transferrin, lactoferrin and ovotransferrin as iron sources as shown by bioassays involving growth of *C. jejuni* in an iron-limited defined broth (MEMα) supplemented with the above host iron binding proteins and radioactive iron uptake assays (103).

Among the different strains, variation is observed in the iron uptake system repertoire (107). Overall, iron uptake systems for free ferrous iron as well as haemin, haemoglobin, and enterochelin have been identified and shown to facilitate iron uptake from specified iron sources. Ferrous iron uptake is facilitated by the FeoB permease (107). Heme acquisition is facilitated from hemin and hemoglobin by ChuABCD, corresponding to the outer membrane receptor, inner membrane permease, ATPase and PBP of an ABC transporter system (126, 127). Enterochelin uptake is facilitated by CeuBCDE and CfrA, whereby CeuBC is the inner membrane permease, and CeuD, CeuE, and CfrA are the ATPase, PBP, and outermembrane receptor, respectively (115, 125). As for ferrichrome uptake, a putative ferrichrome acquisition system, CfhuABD, is identified in some strains (49).

Recently, iron uptake from the transferrin protein family in *C. jejuni* 11168 has been shown to also involve CfrA in addition to another outer membrane protein (encoded by *cj0178*) and a permease (encoded by *cj0174c*). *cj0178* is part of the ChaNR operon including a heme binding lipoprotein encoded by *cj0177* (35) and a Ton energy system encoded by *cj0179-cj0181* (103). *cj0174c* is part of a FbpABC transport system

(cFbpABC), where *cj0175c* is the PBP, and *cj0173c* is the ATPase. *cj0176c* is a short open reading frame (*cfbpA'*) of unknown function. Although all sequenced *C. jejuni* strains contain FbpABC homologues, a couple of strains are missing *cfbpA'*. Furthermore, when present, *cfbpA'* is variable in size, with most ORFs coding for less than 43 amino acids except for one ORF coding for 69 amino acids, suggesting that *cfbpA'* is unlikely to code for a functional protein. Interestingly, the proteins (encoded by the *cj0178* and the *cfrA* genes) involved in iron transport across the outer membrane in *C. jejuni* NCTC 11168 are missing in *C. jejuni* 81-176 (107). The role of the PBP, cFbpA, was not characterized.

1.7 Bordetella pertussis

The *Bordetella* sp. are Gram negative bacteria within the beta subdivision of proteobacteria. *B. pertussis*, *B. parapertussis*, and *B. bronchiseptica* are all respiratory pathogens of mammals. Based on genomic analyses, *B. bronchiseptica* is proposed to be the progenitor for *B. pertussis* and *B. parapertussis*, as these species exhibit gene loss and rearrangements compared with *B. bronchiseptica* (116).

B. pertussis is a strict human pathogen and is the causative agent of whooping cough, primarily a childhood disease (131). Prior to the development of a vaccine, infection in children and infants resulted in significant morbidity and mortality (81). Vaccination resulted in a large reduction in morbidity and mortality caused by *B. pertussis* infection in children (81). However, the vaccine exhibits variable efficacy and waning immunity is observed (81). Although infection in adults results in a persistent cough which is rarely fatal, adults may serve as an important environmental reservoir for

the bacterium (81). Further characterization of the pathogenic mechanisms and the requirements for survival will be useful in developing better treatments/vaccines for *B. pertussis*. As well, *B. pertussis* serves as a useful model and provides insights into other pathogenic bacteria.

B. pertussis uses the BvgAS two component phosphorelay system to express various adherence and virulence factors (83) . The bacteria first adhere to and colonizes the upper respiratory tract, through cell surface proteins, such as fimbriae, filamentous hemagglutinin and pertactin (24). Lipopolysaccharide and secreted toxins (tracheal cytotoxin, adenylate cyclase, dermonecrotic toxin and pertussis toxin) mediate ciliostasis, epithelial cell damage and mucus accumulation, resulting in impaired clearing of the bacteria from the respiratory tract (24).

1.7.1 B. pertussis iron acquisition systems

During colonization and infection, the survival and pathogenesis of *B. pertussis* rely on the acquisition of iron (24). *B. pertussis* can acquire iron from host iron sources such as transferrin, lactoferrin, hemin, and haemoglobin. Furthermore, *B. pertussis* can scavenge iron from the host environment through the production and secretion of the siderophore alcaligin (27) in addition to the utilization of the exogenous siderophores ferrichrome (121), and enterobactin (16). As has been shown for *B. bronchiseptica*, *B.pertussis* may also acquire iron utilizing siderophores that are structurally similar to enterobactin, such as corynebactin and salmochelin (6). Interestingly, iron may also be acquired from transferrin using the neuroendocrine catecholamine norepinepherine (6).

During the course of colonization and infection, the bacteria can encounter various iron sources. Upon entry into the respiratory tract, the majority of extracellular iron is bound by lactoferrin in the mucosa. Following epithelial cell damage, additional iron sources become available, such as transferrin, hemin and haemoglobin (24). Furthermore, enterobactin and structurally similar siderophores may be present in the upper respiratory tract produced either by the normal microbiota or transient bacteria, such as *E. coli* (6). Norepinepherine is present in the respiratory tract and stored in peripheral sympathetic nerve endings (7). In addition, ferrichrome may be present in the upper respiratory tract due to infection with fungi (155).

In *B. pertussis*, the only three iron acquisition systems that have been identified and characterized are for alcaligin, enterobactin, and heme (24). In addition to iron regulation by Fur, these systems also require the presence of the iron source for up-regulation (24). For the endogenous siderophore alcaligin, the biosynthesis pathway is encoded by the *alcABCDE* genes, identified by homology to components of other similar siderophore biosynthesis pathways, including the aerobactin system of *E. coli* (53, 120). Secretion of alcalgin is facilitated by the efflux pump *alcS* (25). As for alcaligin uptake, only the outer membrane receptor *fauA* is identified (26). Positive regulation of genes for alcaligin biosynthesis and transport is facilitated by the regulatory protein AlcR (120). PBP-dependent ABC transport systems for the import of ferric alcaligin into the cytoplasm have not been characterized.

Enterobactin uptake is facilitated by a proposed operon consisting of an outer membrane receptor *bfeA* and a putative periplasmic hydrolase *bfeB* (5). The regulatory

protein BfeR facilitates up-regulation of these genes (5). The receptor BfeA is required for enterobactin uptake (6) and can also transport other ferric catecholates including corynebactin, salmochelin as well as synthetic siderophores (6). The predicted periplasmic location of BfeB suggests that the BfeB hydrolase may be involved in partially degrading enterobactin and similar siderophores to linear products, prior to entry into the cytoplasm using a presently uncharacterized PBP-dependent ABC transport system (5). In pathogenic strains of *E. coli*, *Salmonella* sp., *Klebsiella* sp., a similar mechanism has been proposed for ferric salmochelin uptake that requires partial degradation of the siderophore by a periplasmic IroE hydrolase, a homolog of BfeB, prior to uptake by an IroC ATP-dependent permease (167).

Genes for heme transport and utilization are encoded within the *bhuRSTUV* operon (157). The heme transport and utilization operon is positively regulated by the HurI ECF σ factor and an inner membrane HurR anti σ factor. The outer membrane receptor, BhuR, is necessary for the acquisition of heme from various heme sources including hemin, haemoglobin, haemoglobin-haptoglobin, and hemin-BSA complexes (157). *bhuTUV* code for the periplasmic heme binding protein, permease and ATPase, respectively (157). Following heme transport across the inner membrane, BhuS is hypothesized to sequester the internalized heme to prevent heme toxicity (24).

Additional iron uptake systems that have not been characterized in *B. pertussis* include a FbpABC transport system. Homologues of an FbpABC transport system (bFbpABC) are present and the periplasmic component (bFbpA) may mediate iron uptake under iron limited conditions. A role for the FbpABC transport system in iron

uptake is supported by the observation that siderophores are not detected in the media when transferrin is bound to the outer membrane of *B. pertussis* (55, 124). This result suggests that iron uptake from membrane bound transferrin is mediated by a siderophore independent method where transferrin interacts with outer membrane receptors, similar to the FbpABC transport system from *Neisseria* sp. (45, 102).

1.8 Objectives of my Ph.D. thesis

FbpA proteins are present in diverse bacteria and are important for the acquisition of iron under iron limitated conditions (8, 36, 38, 78-80) . Important bacterial pathogens, such as *C. jejuni* and *B. pertussis*, contain uncharacterized FbpA homologues. The better characterized nFbpA and hFbpA proteins utilize an identical iron binding mechanism involving two N-terminal domain residues histidine and glutamate, two C-terminal domain tyrosine residues, water and a phosphate synergistic anion. Crystal structures of other FbpA proteins also show variation in the iron site ligands and in the utilization and identity of the synergistic anion. Currently iron transfer between the components and across the inner membrane is not well understood; however, the mode of iron binding and the conformations of FbpA proteins likely have crucial roles.

The overall goals of this thesis are to develop a classification scheme for FbpA proteins using bioinformatics and to elucidate the functional roles of cFbpA and bFbpA in iron transport. To elucidate the high affinity iron binding mechanisms of cFbpA, visible spectroscopy and x-ray crystallography were conducted on recombinant FbpA proteins. To demonstrate a role for cFbpA in iron acquisition in *C. jejuni* 81-176, a *cfbpA* deletion strain was constructed and grown under iron-limited conditions. To further

elucidate the role of substrate binding in defining the conformation of FbpA, in-depth conformational analyses were also conducted in solution by small angle X-ray scattering (SAXS) studies. For comparison, SAXS analyses were also conducted for nFbpA. As a tool, SAXS has been invaluable in characterizing the solution conformations of PBPs (138). Furthermore, SAXS data can be compared to the respective crystal structures. In addition, since an apo cFbpA crystal structure is not available, the SAX analyses provide insight into the apo conformation. Similarly for bFbpA, visible spectroscopy, x-ray crystallography and SAXS were conducted and compared and contrasted to data for cFbpA.

Chapter Two: Materials and Methods

2.1 Chemical supplies and media

All chemicals were obtained from Fisher Scientific and Sigma-Aldrich Inc, unless otherwise stated. Kits for the isolation of plasmids and clones (QIAprep spin miniprep kit) from *E. coli* as well as PCR cleanup (QIAquick PCR purification kit) were purchased from Qiagen. Genomic DNA from *C. jejuni* was obtained using the DNeasy Tissue kit from Qiagen. RNA was isolated using the RNeasy Mini Column obtained from Qiagen. For Southern blots, the Hybond-N+ nylon membrane was purchased from Amersham Biosciences. Probes for the Southern blots were labelled and detected using the DIG high prime DNA labelling and detection starter kit II from Roche Diagnostics. Factor Xa and thrombin, used to remove the six-histidine tag from recombinantly expressed proteins, were purchased from Haematologic Technologies. The Mono S HR 5/5 cation exchange column, the CM-Sepharose CL-6B resin and the Sephacryl S-200 were obtained from GE Healthcare. IPTG, ProBond nickel resin, Trizol reagent, and random hexamer mix were purchased from Invitrogen. Acrylamide and other electrophoresis reagents were purchased from Bio-Rad Laboratories Inc. Components for Luria-Bertani broth (LB) and 2 x YT (yeast, tryptone) media were obtained from DIFCO Laboratories. Mueller-Hinton (MH) and Brain Heart Infusion (BHI) media were purchased from Oxoid. For *E. coli*, antibiotics were used at the following concentrations: ampicillin, 100 μg/ml; kanamycin, 25 μg/ml. For *C. jejuni*, antibiotics were used at the following concentrations: trimethoprim, 5 μg/ml; vancomycin, 10 μg/ml; kanamycin, 50 μg/ml.

2.2 Bacterial strains and plasmids

Table 2-1 lists all of the *E. coli* and *C. jejuni* strains that were used in this study. *E. coli* DH5α was used for propagation of plasmids and clones. *E. coli* HMS174 (λDE3) and *E. coli* BL21 (λDE3) cells were used to express recombinant cFbpA from *C. jejuni* NCTC 11168 and bFbpA from *B. pertussis* Tohama I, respectively. cFbpA was also characterized in C. *jejuni* 81-176. *E. coli* bacterial stocks were stored at -80 °C in LB containing 11 % glycerol. *C. jejuni* bacterial stocks were stored at -80 °C in BHI broth containing 40% glycerol. Table 2-2 lists all of the plasmids and clones used in this study.

Table 2-1 Bacterial strains used in this study

Strain	Relevant characteristics	Reference
E. coli DH5α	General host strain for plasmid/clone propagation	Life Technologies
E. coli BL21 (λDE3)	Deficient in *lon* and *ompT* proteases. λ prophage contains T7 RNA polymerase gene.	Novagen (145)
E. coli HMS174 (λDE3)	RecA mutant. λ prophage contains T7 RNA polymerase gene.	Novagen (145)
C. jejuni NCTC 11168	Iron uptake systems include hemin uptake system (ChuABCD), enterochelin transport (CeuBCDE and CfrA), ferric uptake from transferrin/lactoferrin (cFbpABC and ChaNR). Lacks ferrichrome uptake system (CfhuABD).	National Collection of Type Cultures (NCTC) (50, 67)
C. jejuni 81-176	Highly invasive. Contains pVir plasmid that contributes to virulence and high level of invasion into intestinal cells. Iron uptake systems as for NCTC11168, except that ChaNR and CfrA are absent.	Isolated from raw milk outbreak (67, 85)
C. jejuni 81-176 *ΔcfbpA*	*cfbpA* targeted deletion mutant of *C. jejuni* 81-176.	This thesis

Table 2-2 Bacterial plasmids and clones used in this study

Plasmid or clone	Relevant characteristics	Reference
pBluescript II SK(-)	*E. coli* cloning vector. Contains ampicillin resistance gene.	Stratagene
pDrive	Cloning vector for direct ligation of PCR products. Vector contains single 3' U overhang at each end for ligation with the 3' A overhang of PCR products generated from non-proofreading DNA polymerases. Contains ampicillin and kanamycin resistance genes.	Qiagen
pET-28a(+)	*E. coli* expression vector containing T7 promoter. Contains N-terminal His tag coding sequence and option for C-terminal His tag coding sequence. Contains kanamycin resistance gene.	Novagen (145)
pET-28a(+)-cFbpA	The coding region of *cfbpA* lacking signal sequence cloned into a pET-28a(+) expression vector (NcoI and XhoI) in-frame with a C-terminal His tag.	This thesis (153)

Plasmid or clone	Relevant characteristics	Reference
pET-28a(+)-bFbpA	The coding region of *bfbpA* lacking signal sequence from *B. pertussis* Tohama I cloned into a pET-28a(+) expression vector (NdeI and XhoI) in-frame with an N-terminal His tag.	This thesis
pBluescript II SK(-)-cFbpA:Kan	pBluescript II SK(-) clone containing the *cfbpA* disruption construct. Used as suicide vector for construction of *C. jejuni* 81-176 *ΔcfbpA* strain. The *cfbpA* disruption construct consists of an internal deletion of 133 bp within *cfbpA* and replacement with a kanamycin resistance cassette (XmaI) from pUC18K2.	This thesis

2.3 Phylogenetic analyses

Protein sequences homologous to the FbpA from *H. influenzae* (ZP_00157690.1), *B. pertussis* Tomaha I (NP_880337.1), and *C. jejuni* NCTC 11168 (NP_281385.1) were identified in the nr database with the BlastP (3) portal at the National Institutes of Health (http://www.ncbi.nlm.nih.gov/BLAST/, verified Aug. 31st, 2008). FbpA homologs were selected from the 100 best hits from each BlastP search such that the sequences shared 75% identity or less, exhibited an E-value of 10^{-20} or less, and were annotated to identified prokaryotes. Protein sequences were aligned with ClustalW (65) using a gap opening penalty of 15 and a BLOSUM series matrix, followed by the generation of a neighbour-joining bootstrapped tree. The alignment was refined manually in BioEdit (60) to exclude the signal sequences. A second tree was made using maximum-likelihood analysis with TREE-PUZZLE 5.0 (132). The parameters used were 250000 puzzling quartets, exact parameter estimates and exact maximum likelihood. Subsequent BlastP searches using the same criteria and tree constructions were performed to find additional FbpA sequences.

2.4 DNA manipulation

Isolation of genomic DNA from C. jejuni. Purified genomic DNA from *C. jejuni* was isolated using the DNeasy Tissue kit from Qiagen following the instructions in Appendix E: Purification of genomic DNA from Gram-positive bacteria (http://www.his.se/upload/10412/MM2.pdf) with the following modifications. 1 ml of a 0.5 OD_{600} cell culture was harvested and lysed according to the manufacturer's

instructions. Following lysis, 10 µl of 10 mg/ml RNase A was added prior to the addition of proteinase K.

Cloning of cfbpA into a pET-28a(+) expression vector. Purified genomic DNA from *C. jejuni* NCTC 11168 was obtained from Dr. Erin Gaynor (University of British Columbia). The coding region of *cfbpA*, lacking the signal sequence, was amplified from *C. jejuni* NCTC 11168 using the cFbpA_For and cFbpA_Rev primers (Table 2-3). The primers include NcoI and XhoI restriction sites, for cloning into a pET-28a(+) expression vector in frame with a C-terminal His tag. The 3' primer also includes a Factor Xa site for removal of the His tag.

Cloning of bFbpA into a pET-28a(+) expression vector. Purified genomic DNA from *Bordetella pertussis* Tohama I was obtained from Dr. Rachel C. Fernandez (University of British Columbia). The coding region of *bfbpA*, lacking the signal sequence, was amplified by PCR using the bFbpA_For and bFbpA_Rev primers (Table 2-3). The primers include NdeI and XhoI restriction sites, for cloning into a pET-28a(+) expression vector in-frame with an N-terminal His tag.

Construction of the pBluescript II SK(-) clone containing the cfbpA disruption construct. The coding region of *cfbpA* lacking signal sequence was amplified by PCR, as described in the cloning of cFbpA into the pET-28a(+) expression vector section. The PCR fragment was then inserted into pDrive (Qiagen) and subcloned into pBluescript SK(-) using the EcoRV and BamHI restriction sites. The *cfbpA* disruption construct was generated by performing first inverse PCR of the pBluescript SK(-) (Stratagene) clone using the Inv_F and the Inv_R primers (Table 2-3). The primers were designed to include

425 bp and 396 bp of *cfbpA* flanking an internal deletion of 133 bp. Both primers included XmaI restriction sites for insertion of a non-polar kanamycin resistance cassette (lacking a promoter and transcription terminator) from pUC18K2 (98) to create the *cfbpA* disruption construct. Insertion of the kanamycin cassette was confirmed by restriction digestion and DNA sequencing. All clones and vectors were obtained following transformation of competent cells by heat shock or electroporation methods.

Table 2-3 Primers used in this study

Primer	5' to 3' sequence
Cloning	
cFbpA_For	AACTGCACCCATGGCTAGTGAGCTTAATATTTACTCAGC
cFbpA_Rev	ATACTCGAGGCGGCCTTCAATTCTAAAACCGACTTCATCGTA AATTT
bFbpA_For	ATGAAGCTTCATATGTCCGATGAGGTCAGCCTCT
bFbpA_Rev	ATACTCGAGTGCCGACAAACAAGGCAGT
Inverse PCR cloning	
Inv_F	ATGCCCGGGTTTGCAGGCGAAGCTAAATT
Inv_R	ATGCCCGGGGGAGCTGTAGCACTTCTCATAACA
c*fbpA* transcription	
cFbpA'tocFbpA_For:	TACTATGCGTTGGCTTTGCTTTTGCTT
cFbpAtocFbpA'_Rev:	GGAGCTGTAGCACTTCTCATAACAATTTCTCC
cFbpAtocFbpB_For:	CAGGCGAAGCTAAATTTGCAGTTATGAATAC
cFbpBtocFbpA_Rev:	AACCAATAAAGCTCCAGAAAAAATGGCAG
cFbpBtocFbpC_For:	TGGGTTATTCTATACCTGCTGCTGCTTTAGGGA
cFbpCtocFbpB_Rev:	AGCCACTCTTTGCGCTTGCCCTCCTG

2.5 Protein expression and purification

Expression and purification of cFbpA. Recombinant expression was performed in *E. coli* HMS174 (λDE3) cells. Growth media were supplemented with kanamycin. An overnight culture grown in LB was used to inoculate 2 x YT media for protein expression. Inoculated cultures were grown initially at 37 °C and then transferred to 30 °C. Cells were induced at an A_{600} of 0.5 to 0.6 with 0.5 mM IPTG and grown overnight. Cells were then suspended in a binding buffer containing 300 mM NaCl, 50 mM NaH_2PO_4 pH 7.9 and lysed at 4°C using an Avestin EmulsiFlex-C5 homogenizer. After pelleting cell debris, the soluble fraction was applied to a ProBond nickel resin column that was pre-equilibrated with binding buffer. The column was then washed with binding buffer followed by step-wise elution of the red cFbpA protein using increasing concentrations of imidazole in binding buffer. The histidine tag was removed by digestion with Factor Xa in 150 mM NaCl, 2 mM $CaCl_2$, 20 mM Tris-HCl, pH 7.5 overnight at 4 °C followed by inactivation with 1 mM phenylmethanesulphonyl fluoride (PMSF). To prepare the "as isolated" holo cFbpA protein, equimolar ferrous sulfate was then added to ensure that the sample was fully saturated with iron. Excess iron was then removed by buffer replacement with 20 mM Tris-HCl pH 7.5 utilizing an Amicon centrifugal filter unit.

Apo cFbpA was obtained by incubating the holo cFbpA with 1000 fold excess EDTA in 10 mM Tris-HCl pH 7.4 for 10 min. To remove the excess EDTA, the buffer was exchanged with 200 mM NaCl and 10 mM Tris-HCl, pH 7.4 by gel filtration using a Sephacryl S-200 column.

Expression and purification of bFbpA. Recombinant expression and purification of bFbpA is as described for cFbpA, with the following modifications. Recombinant expression was performed in *E. coli* BL21 (λDE3) cells. Following elution using imidazole, colorless apo-bFbpA protein was obtained. The histidine tag was removed by digestion with bovine alpha thrombin in 20 mM Tris-HCl, pH 7.0 overnight at 4 °C. The bFbpA protein was then applied to a Mono S HR 5/5 cation exchange column in 20 mM Tris-HCl, pH 7.0 and the flow-through fraction containing apo-bFbpA was collected.

Expression and purification of nFbpA. Recombinant phosphate-bound holo nFbpA from *Neisseria gonorrhoeae* was isolated by cell lysis with cetyltrimethylammonium bromide followed by one-step chromatography on CM-Sepharose CL-6B, as described previously (17).

2.6 Protein characterization

SDS-PAGE. For denaturation of protein, samples were boiled in 5x loading buffer (10 % (v/v) glycerol, 2 % (w/v) SDS, 5 % (v/v) β mercaptoethanol, 0.025 %(v/v) bromophenol blue, 62.5 mM Tris-HCl, pH 6.8) for 5 min. Samples were then applied to 12 % polyacrylamide gels electrophoresed in running buffer (192 mM glycine, 3 mM SDS, 24 mM Tris base pH 8.3) at 200V for approximately one hour. Visualization of the protein bands was facilitated by staining of the gel in Coomassie blue R solution and destaining in a solution containing 10 % (v/v) methanol and 7 % (v/v) acetate.

Bradford standard assay. Protein samples were quantified by the Bradford

Method (21). The Bio-Rad Protein Assay Dye Reagent Concentrate was utilized according to the manufacturer's instructions. Purified bovine serum albumin from Sigma-Aldrich was used for standards.

Mass spectrometry. The purity and homogeneity of the recombinant protein samples were analysed by SDS-PAGE and mass spectrometry. Protein samples of cFbpA and bFbpA prior to and following digestion with either FactorXa or thrombin, respectively, were characterized by mass spectrometry. The protein samples in 20 mM Tris pH 7.0 were injected onto a reverse phase column interfaced to an electrospray ionisation mass spectrometer. All mass spectrometry measurements were kindly conducted by Shouming He from the laboratory of Dr. Stephen Withers.

2.7 Iron binding analyses by visible spectroscopy

All of the visible spectroscopy experiments were conducted using a Varian Cary Bio50 UV spectrophotometer at room temperature.

Analyses of iron binding by cFbpA. Visible spectroscopic data were obtained using a 1 cm pathlength 80 µl quartz cuvette. The iron binding experiments were performed using 2 mg/ml (0.055 mM) apo protein in a buffer containing 200 mM NaCl, 10 mM Tris-HCl, pH 7.4. Visible absorbance was monitored for 10 min after the addition of an equimolar concentration of iron. The iron sources were ferric chloride, ferrous sulfate and ferric chloride chelated by a 100 M excess of oxalate. Following the 10 min incubation with ferrous sulfate, sodium bicarbonate was added to a final concentration of 5.5 mM and monitored for an additional 10 min.

Analyses of iron binding by bFbpA. Visible spectra were obtained using a 1 cm pathlength 1 ml quartz cuvette. The iron binding experiments were conducted in 200 mM NaCl, 20 mM Tris-HCl buffer, pH 7.0. To prepare the bFbpA:Fe:carbonate sample, equimolar ferrous sulfate was added to apo bFbpA in the presence of ambient carbonate. bFbpA:Fe:oxalate and bFbpA:Fe:citrate protein samples were prepared as described for bFbpA:Fe:carbonate followed by the addition of oxalic acid or sodium citrate to final concentrations of 3.6 mM and 1.3 mM, respectively. Visible spectra were monitored for 10 min. The final concentrations of the protein samples were 0.21 mM for bFbpA:Fe:carbonate (7.4 mg/ml) and bFbpA:Fe:oxalate (7.3 mg/ml) and 0.17 mM for bFbpA:Fe:citrate (5.9 mg/ml).

Iron affinity of cFbpA and bFbpA. Iron affinity was estimated through iron chelator competition experiments and comparison with phosphate-bound holo nFbpA. For estimation of cFbpA iron affinity, incremental amounts of sodium pyrophosphate from 0 to 7 mM were added to holo cFbpA and holo nFbpA in 30 mM NaCl, 10 mM Tris-HCl, pH 7.4.

For bFbpA:Fe:carbonate, bFbpA:Fe:oxalate and bFbpA:Fe:citrate, visible spectra were measured on a Varian Cary 50 Bio UV spectrophotometer using a 1 cm pathlength 80 µl quartz cuvette. Holo bFbpA protein samples were prepared by addition of equimolar ferrous sulfate to apo protein in the presence of ambient carbonate, 3.6 mM oxalate or 1.3 mM citrate in 20 mM Tris-HCl, pH 7.0. The iron affinity experiments were conducted using 2 mg/ml (0.057 mM bFbpA, 0.059 mM nFbpA) holo protein in a buffer containing 200 mM NaCl, 10 mM Tris-HCl, pH 7.4. For bFbpA:Fe:carbonate, iron

affinity was measured in the presence of ambient carbonate and 57 mM $NaHCO_3$. Iron affinity measurements for bFbpA:Fe:oxalate and bFbpA:Fe:citrate were carried out in buffer containing 3.6 mM oxalate and 1.3 mM citrate, respectively. Increasing concentrations of sodium pyrophosphate, from 0 to 30 mM, were added to the holo proteins and spectra of holo bFbpA and holo nFbpA were monitored at 416 nm and 480 nm, respectively.

2.8 X-ray crystallography

2.8.1 cFbpA structures

As isolated holo cFbpA. Protein treatment is as described in section 2.5. Crystals were grown at 19 °C by the hanging drop vapor diffusion method and micro-seeding. The reservoir contained 24% polyethylene glycol 4000, 0.1 M Tris-HCl pH 8, and 60 mM sodium acetate. Each drop was made from an equal volume of reservoir and a 15 mg/ml protein stock solution. Crystals were transferred to the reservoir plus 30% (v/v) glycerol as a cryprotectant and looped directly into a cryostream at 100 K. X-ray data were collected on a home laboratory source using a MAR345 image plate system. The data frames were indexed and the resulting intensities were scaled and merged with DENZO and SCALEPACK (113).

The crystal grew in space group $P2_1$ (a=54.45 Å, b= 90.70 Å, c=56.83 Å, and β=92.4 °) with 2 molecules in the asymmetric unit (solvent content of 38%). A comparative model of cFbpA was constructed using the apo bFbpA structure from *Bordetella pertussis* (PDB ID 1Y9U) as a template with SWISS-MODEL (135). Each of the 2 domains of the resulting cFbpA model was superimposed onto the corresponding

domains of *Haemophilus* holo hFbpA (PDB ID 1MRP) (32) to generate a model of the holo cFbpA. A molecular replacement solution was obtained using this model and the program MolRep (155) within the CCP4 suite of programs (40). Interpretable electron density maps were produced by 2-fold averaging using DM. The structure was refined to 1.8 Å resolution with O (70), CNS (30) and REFMAC (105).

Iron-reconstituted cFbpA. An equimolar concentration of ferric chloride chelated by 100 molar excess sodium oxalate was added to 10 mg/ml apo cFbpA in 20 mM Tris-HCl pH 7.5. Following 10 min incubation at room temperature and 2 h incubation on ice, the protein was dialyzed against 20 mM Tris-HCl, pH 7.4 overnight. Crystals were grown at 25°C by the hanging drop vapor diffusion method. The reservoir contained 24% PEG 4000, 0.1 M Tris-HCl pH 8.5 and 60 mM sodium acetate. Each drop was made from an equal volume of reservoir and a 9 mg/ml protein stock solution. Crystals were transferred to reservoir solution containing 30% (v/v) glycerol and immersed in liquid nitrogen. X-ray data was collected at 100 K at the Stanford Synchrotron Radiation Laboratory (SSRL) beamline 11-3 using an ADSC Quantum-4 CCD detector. The data were indexed and the resulting intensities were scaled and merged with DENZO and SCALEPACK (113). The iron-reconstituted cFbpA crystal grew in space group $P2_12_12_1$ (a=57.11 Å, b=54.74 Å, c=92.94 Å), with 1 molecule in the asymmetric unit (solvent content of 29%). A molecular replacement solution was obtained using the as isolated holo cFbpA coordinates (PDB ID 1Y4T) (153) and the program MolRep (155) within the CCP4 suite of programs (34). The structure was refined to 1.6 Å resolution using O (70), CNS (30), and REFMAC (105).

2.8.2 bFbpA structures

SeMet apo bFbpA. Seleno-methionine labeled (SeMet) apo bFbpA was obtained by expression of pET-28a(+)-bFbpA in *E. coli* BL21 (DE3) using a previously published procedure with minor modifications (156). Prior to the addition of SeMet, the culture was grown at 37 °C until an OD_{600} of 0.5. The cells were induced with 1mM IPTG and grown at 27 °C overnight. SeMet labeled apo bFbpA was isolated and purified as described for the unlabeled bFbpA.

SeMet apo bFbpA crystals were grown at 19°C by the hanging drop vapor diffusion method in a reservoir containing 34 % PEG 1500 and 100 mM MES pH 6.0. Each drop was made from an equal volume of reservoir and a 15 mg/ml protein stock solution containing 20 mM Tris-HCl, pH 7.0. Crystals were transferred to the reservoir plus 30% (v/v) glycerol and data were collected at 100 K. Multi-wavelength anomalous dispersion (MAD) data were collected at the SSRL beamline 9-2 at (Menlo Park, CA). The SeMet apo bFbpA crystal grew in space group $P2_12_12_1$ (a= 63.16 Å, b= 66.78 Å, c= 71.47 Å) with one molecule in the asymmetric unit (solvent content of 33 %). The data were indexed, scaled and merged with DENZO and SCALEPACK (113). Phases were estimated using the Solve package (150) and a model was built manually using the program O (70) and refined to 2 Å resolution using CNS (30) and REFMAC (105).

Apo bFbpA. Unlabeled apo bFbpA protein samples were prepared as described in the protein expression and purification section. Apo bFbpA crystals were prepared as described for the SeMet apo bFbpA crystals except that the reservoir contained 28% PEG 1500, 100 mM MES pH 6.0. X-ray data were collected at the SSRL beamline 9-1 and

processed using DENZO and SCALEPACK (113). The apo bFbpA crystal grew in space group $P2_12_12_1$ (a= 59.39 Å, b= 71.47 Å, c=74.82 Å) with one molecule in the asymmetric unit (solvent content of 37 %). A molecular replacement solution was obtained using the SeMet structure and the program MOLREP (155) within the CCP4 suite of programs (40). The structure was refined to 1.4 Å resolution with O (70), CNS (30) and REFMAC (105).

bFbpA:Fe:oxalate. Protein samples of bFbpA:Fe:oxalate were prepared by addition of oxalic acid to a final concentration of 3.6 mM and an equimolar iron:protein concentration of ferrous sulfate to unlabeled apo bFbpA in 20 mM Tris-HCl, pH 7.0. The bFbpA:Fe:oxalate crystals were prepared as described for SeMet apo bFbpA crystals except that the crystals were grown at 21°C in a reservoir containing 26% PEG 2000, 3.6 mM oxalate and 100 mM MES pH 6.0. X-ray data were collected at the SSRL beamline 1-5 and processed using HKL2000 (113). The crystal grew in $P2_12_12_1$ (a=59.24 Å, b=71.45 Å, c=74.98 Å) with one molecule in the asymmetric unit (solvent content of 36 %). A molecular replacement solution was obtained using the apo bFbpA structure (PDB ID 1Y9U) and the program MOLREP (155) within the CCP4 suite of programs (40). The structure was refined to 1.5 Å resolution with O (70), and REFMAC (105).

bFbpA:Fe:carbonate. Protein samples of bFbpA:Fe:carbonate were prepared by addition of an equimolar concentration of ferrous sulfate to unlabeled apo bFbpA in 20 mM Tris-HCl, pH 7.0. The crystals of bFbpA:Fe:carbonate were prepared as described for bFbpA:Fe:oxalate except that the reservoir contained 34% PEG 1500, and 100 mM Tris-HCl pH 9.0. X-ray data collection and processing are as described for

bFbpA:Fe:oxalate. The crystal grew in space group $P2_12_12_1$ (a=54.67 Å, b=57.28 Å, c=87.93 Å) with one molecule in the asymmetric unit (solvent content of 26 %). A model of the closed conformation of bFbpA was generated by superimposing each of the two domains onto the corresponding domains of holo FbpA from *C. jejuni* (PDB ID 1Y4T). A molecular replacement solution was obtained using this closed conformation model and the program MOLREP (155) within the CCP4 suite of programs (40). Refinement to 2.4 Å resolution is as described for bFbpA:Fe:oxalate.

2.9 Solution structure of cFbpA and bFbpA protein samples

2.9.1 Preparation of protein samples.

Recombinant apo bFbpA and apo cFbpA were produced as described in section 2.5. Iron loaded protein samples of bFbpA were obtained as described in section 2.7 (analyses of iron binding by bFbpA). Holo cFbpA was obtained by the equimolar addition of ferrous sulfate to apo protein. The protein samples in 200 mM NaCl, 20 mM Tris-HCl buffer, pH 7.0 were then applied to a 1.0 cm x 18.0 cm column containing Sephacryl S-200 (GE Healthcare) equilibrated and eluted with the same buffer. Oxalic acid and sodium citrate at final concentrations of 3.6 mM and 1.3 mM, respectively, were added back to the bFbpA:Fe:oxalate and bFbpA:Fe:citrate eluates. Apo and holo samples were confirmed by the absence and presence of absorbance peaks within the 400 to 500 nm range, respectively.

Phosphate-bound holo nFbpA was obtained as described in section 2.5. To obtain apo protein, a CM-Sepharose column with protein adsorbed was washed with 10 mM sodium citrate in a 10 mM Tris buffer, pH 8 followed by elution with 30 mM sodium

citrate in the same buffer. The protein samples in 200 mM NaCl, 20 mM Tris-HCl buffer, pH 7.0 were then applied to a gel filtration column as described for the cFbpA and bFbpA protein samples.

2.9.2 Small angle x-ray scattering

Scattering measurements were made at the BioCAT facility, beamline ID18, of the Advanced Photon Source at Argonne National Laboratory (Illinois). The X-ray wavelength of 1.03 Å and sample-detector distance of 1.8917 m were used to cover the range of momentum transfer values ($Q = 4 \pi \sin \theta/\lambda$, where 2θ is the scattering angle) from 0.08 to 2.50 nm^{-1}. Samples were held in a 1.5 mm quartz capillary at 20°C and moved continuously past the X-ray beam during the SAXS measurements to avoid local heating. Three successive exposures of 9.7 s were recorded for each sample. Recording of the relevant buffer preceded and followed the recording of each protein sample. Two dimensional images were recorded using a CCD detector. The data were integrated using the Fit2D program (61) and additional data processing (averaging of frames, beam intensity correction, buffer subtraction) was performed using Microsoft Excel spreadsheets.

Data were collected for apo bFbpA (1.2, 3.3, and 9.4 mg/ml), bFbpA:Fe:carbonate (0.9, 1.8, 3.7, and 7.4 mg/ml), bFbpA:Fe:oxalate (3.8 and 7.5 mg/ml), and bFbpA:Fe:citrate (3.0 and 6.1 mg/ml). No concentration-dependent changes in radius of gyration (Rg) were observed, and changes in the forward scattering, I(0), were proportional to concentration, demonstrating that bFbpA remains monomeric through the concentration range used for the SAXS measurements. For

bFbpA:Fe:carbonate, subsequent analyses were conducted using the SAXS data from the 7.4 mg/ml sample. For bFbpA:Fe:oxalate and bFbpA:Fe:citrate, composite data sets were produced using the low angle region from the lower protein concentration sample and the high angle region from the higher protein concentration sample. This approach reduces error in the data analyzed at high resolution, yet minimizing the scatter of aggregated protein at the low angle region. For apo bFbpA, a composite data set was produced from the 3.3 and 9.4 mg/ml samples. The other FbpA proteins were measured at only a single protein concentration, as follows: apo nFbpA, 5.7 mg/ml; holo nFbpA, 7.3 mg/ml; apo cFbpA, 5.9 mg/ml; and holo cFbpA, 5.9 mg/ml. Analyses were conducted within the range of momentum transfers judged to be contributed predominantly by monomers in solution: from 0.404 to 2.402 nm^{-1}, 0.459 to 2.498 nm^{-1}, and 0.279 to 2.156 nm^{-1} for the bFbpA, nFbpA and cFbpA protein samples, respectively.

FbpA molecular models, including dummy residues for disordered regions and iron for holo FbpA models and excluding crystallographic water molecules and synergistic anions, were evaluated using the program CRYSOL (146) with default parameters. Agreement between the theoretical scattering from a model and the experimental data is measured by the χ^2 value,

$$\chi^2 = \frac{1}{N-1}\sum_{j=1}^{N}\left|\frac{I(Q_j) - I_{\exp}(Q_j)}{\sigma(Q_j)}\right|^2$$

where for each momentum transfer value Q_j, the theoretical scattering is $I(Q_j)$, the experimentally observed scattering is $I_{exp}(Q_j)$, and the error for the experimental measurement is $\sigma(Q_j)$. For crystal structures containing multiple chains, chain A was selected. The closed models for bFbpA, nFbpA and cFbpA refer to PDB entry codes 2OWT, 1D9Y, and 1Y4T, respectively. Additional models exhibit interdomain displacements about the hinge region as compared with the closed models. The interdomain angles, calculated using DynDom (62), characterize the degree of interdomain displacement relative to the closed structure. Ajar models are characterized by a range of interdomain angles between the closed conformation and 50°. The ajar models include the apo bFbpA (PDB ID 1Y9U) and nFbpA (PDB ID 1R1N) crystal structures. A model is defined as open when the interdomain angle is greater than 50°. Open models as well as some ajar models are *in silico* manipulations involving interdomain displacement due to rotation about the respective hinge regions of apo bFbpA (PDB ID 1Y9U), nFbpA (PDB ID 1R1N), and cFbpA (1Y4T) using the program O (70).

2.10 Function of cFbpA within C. jejuni 81-176

2.10.1 C. jejuni growth conditions

Growth studies were conducted using the highly invasive *C. jejuni* 81-176 strain (11, 119). *C. jejuni* strains were grown microaerobically in a tri-gas incubator (Sanyo) under the following conditions: 82% N_2, 12% CO_2, 6% O_2 at 37°C. Bacteria were routinely cultured on MH agar plates containing trimethoprim and vancomycin (MH-TV).

Prior to initiation of iron-limited growth studies, bacteria were grown overnight in MH-TV biphasic media (5 ml MH-TV broth over 10 ml MH-TV agar) to an OD_{600} of approximately 0.2 and used to inoculate fresh MH-TV biphasic media to an initial OD_{600} of 0.025. Growth studies were conducted in triplicate in MH-TV biphasic media with iron limitation achieved by addition of 20 μM deferoxamine mesylate salt (Desferal) (Sigma). Growth was monitored at OD_{600} on a Biomate 3 UV-Vis spectrophotometer (Thermo Scientific), and Colony Forming Units (CFUs) were then enumerated on MH-TV agar plates by serial 10-fold dilutions. Data were analyzed by the paired Student t-test.

2.10.2 Transcription of cfbpA'ABC in C. jejuni 81-176.

C. jejuni 81-176 was cultured as described for the iron limited growth studies. The bacteria were harvested and RNA was isolated, as described previously (50). Briefly, frozen bacterial pellets were resuspended in 0.4 mg/ml lysozyme in Tris-EDTA buffer (10 mM Tris-HCl, 1 mM EDTA, pH 7.5) and incubated at room temperature for 5 min. The bacteria were then lysed by addition of a 20X volume of Trizol reagent (Invitrogen). Following chloroform extraction, an equivalent volume of 70% ethanol was added to the sample. The sample was then applied to an RNeasy Mini Column (Qiagen), and treated according to manufacturer's instructions, including on-column DNase treatment (Qiagen). Reverse transcription was performed using 1μg RNA sample and 4 μg of a random hexamer mix (Invitrogen). To elucidate if c*fbpA* is transcribed as part of an operon, PCR experiments were conducted on the *C. jejuni* 81-176 cDNA sample using primers (Table 2-3) to amplify the regions containing the junctions between c*fbpA'* (locus

tag *CJJ81176_0212*) and *cfbpA* (locus tag *CJJ81176_0211*), c*fbpA* and c*fbpB* (locus tag *CJJ81176_0210*), and c*fbpB* (locus tag *CJJ81176_0210*) and c*fbpC* (locus tag *CJJ81176_0209*). To ensure that genomic DNA was not a contaminant of the cDNA sample, amplification by PCR was also conducted using an equivalent amount of RNA sample.

2.10.3 Construction of the C. jejuni 81-176 cfbpA targeted deletion mutant (ΔcfbpA).

The *ΔcfbpA* mutant was obtained by natural transformation (159) of pBluescript II SK(-)-cFbpA:Kan. Briefly, *C. jejuni* 81-176 was grown for 14 hours overnight on MH-TV plates, re-plated in patches of approximately 2 cm in diameter on fresh MH-TV plates and grown for an additional 2 hours. 2 µl of a 8.9 mg/ml pBluescript II SK(-)-cFbpA:Kan was then added to *C. jejuni* 81-176 and mixed within the patch, followed by incubation for 4 to 5 hours. The bacteria were then harvested, plated onto MH-TV agar plates supplemented with kanamycin and incubated. Transformants were observed after two days. The Δc*fbpA* strain was confirmed by PCR using using the cFbpA_For and cFbpA_Rev primers (Table 2-3) and DNA sequencing.

Southern analyses were also conducted to verify the correct insertion of the kanamycin resistance cassette into *cfbpA*. Digoxigenin(DIG)-labeled probes for Southern blot analyses were generated using the DIG high prime DNA labelling and detection starter kit II. The *cfbpA* probe was prepared using the coding region of *cfbpA* (PCR amplified using cFbpA_For and cFbpA_Rev primers as described in Table 2-3) as a template. To ensure that the mutation occurred by a double crossover event, a probe was also generated using *pBluescript II SK(-)* as template. Chromosomal DNA from *C. jejuni*

81-176 WT and the Δ*cfbpA* mutant was isolated using the DNeasy kit, as described in section 2.4, and digested with HindIII and EcoRV. Following separation on a 1 % agarose gel, the DNA was transferred to a Hybond-N+ nylon membrane by capillary action. Prehybridization and overnight hybridization with the *cfbpA* probe were carried out at 40 °C followed by washing steps at 68 °C. Detection of hybridization signals was performed using the DIG high prime DNA labelling and detection starter kit II. For reprobing of the blot, the blot was stripped according to the instructions provided in the DIG high prime DNA labelling and detection starter kit II. Reprobing with the *pBluescript II SK(-)* probe was conducted as described for the *cfbpA* probe except that the prehybridization and overnight hybridization were conducted at 48 °C. Hybridization signals were detected as described for the *cfbpA* probe.

Chapter Three: Anion-independent iron coordination by the *Campylobacter jejuni* ferric binding protein

3.1 Introduction

In the human body, available iron is limited due to low solubility and sequestration by host iron binding proteins such as transferrin and lactoferrin (23, 123). High affinity iron acquisition systems, such as the FbpABC transport system, are utilized by bacterial pathogens to acquire growth essential iron (123). Periplasmic FbpA proteins are found in diverse bacteria and utilize different sets of ligands for iron binding (86, 142, 144).

Campylobacter jejuni is the leading cause of human gastroenteritis in developed countries (84) and requires iron for growth (158). Most *C. jejuni* strains do not secrete siderophores (46), but are able to obtain iron from exogenous siderophores (enterochelin and ferrichrome), haemin, haemoglobin, transferrin, lactoferrin as well as free ferric and ferrous ions (103, 158). *C. jejuni* contains an FbpABC transport system which facilitates iron acquisition from transferrin and lactoferrin (103).

To elucidate the role of cFbpA in iron transport, iron binding was analysed by x-ray crystallography and visible spectroscopy. In addition, a classification scheme for FbpA proteins was developed through phylogenetic characterization.

3.2 Results

3.2.1 The 'as isolated' holo cFbpA crystal structure

The overall structure of 'as isolated' holo cFbpA consists of 2 globular domains linked by 2 β-strands (Figure 3-1, panel A). The N-terminal domain is comprised of

residues 5 to 103 and 239 to 283. The remaining residues, 104 to 238 and 284 to 321, form the C-terminal domain. Each domain is formed from α–β–α units that contribute to form a central 5 stranded β-sheet surrounded by 6 α-helices in the N-terminal domain and a central 3 stranded β-sheet surrounded by 8 α-helices in the C-terminal domain. The hinge region, which may allow for domain movement, is located within the 2 interdomain β-strands. FbpAs are typically monomers and the 2 molecules in the asymmetric unit are essentially the same (0.26 Å r.m.s. deviation on α-carbons) and make few contacts. The cFbpA structure displays excellent stereochemistry, as shown by a Ramachandran plot, with 95.5% of the residues residing in the most favored regions and the remaining residues in the allowed regions (91). Data collection and refinement statistics are summarized in Table 3-1. All subsequent results are for molecule A.

The iron-binding site is located at the domain interface and the 5 coordinating residues originate from both domains (Figure 3-1, panel B). The coordination sphere is composed of His14 near the N-terminus and 4 Tyr residues, 1 from the N-terminal domain (Tyr15) and 3 from the C-terminal domain (Tyr146, Tyr202, Tyr203). His14 and Tyr15 are part of a long loop whereas Tyr146, Tyr202 and Tyr203 are contributed from the N-termini of 2 α-helices. The iron is coordinated in a distorted octahedral geometry with 1 absent site (Table 3-2). Surprisingly, no density is observed for an anion near the

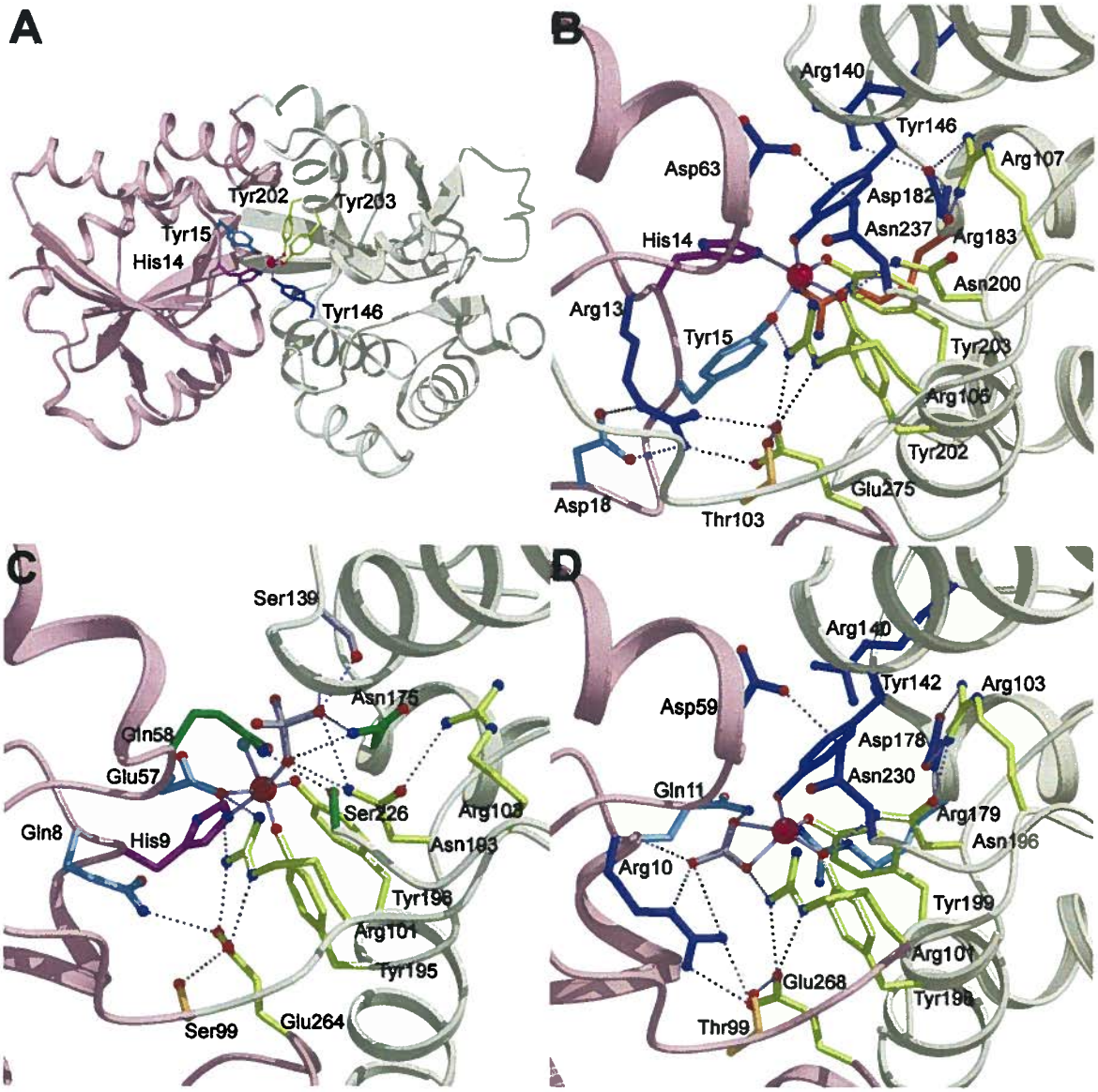

Figure 3-1 The crystal structure of cFbpA and comparison of the iron site to hFbpA and mFbpA.

In all panels, the backbones of the N- and C- terminal domains are in light pink and khaki colours, respectively. Yellow residues are conserved among most FbpAs with few exceptions. Dark pink residues are conserved among most Class I and III FbpAs. Dark purple residues are conserved generally among Classes II, III and IV FbpAs. Cyan residues are conserved with few exceptions within their respective Classes. Synergistic anions and a non-conserved residue are grey and functionally conserved residues are tan. H-bonds and ligand bonds to the iron (red-pink sphere) are indicated by dotted and solid lines, respectively. The nitrogen and oxygen atoms of the residue side chains are coloured blue and red, respectively. The images were generated using MolScript (87) and

Raster3D (99). A, The overall structure of cFbpA with the iron-binding site. B, cFbpA (Class III) iron-binding site. The orange residue is conserved in Class II FbpAs. C, hFbpA (Class I) iron-binding site. The blue sphere is a water molecule and green residues are conserved functionally in Class I FbpAs. D, The mFbpA (Class II) iron-binding site.

Table 3-1 Data collection and refinement statistics for cFbpA

Crystal	cFbpA
Wavelength (Å)	1.54179
Resolution range (Å)	16.0 – 1.8 (1.86 – 1.80)
R_{merge}	0.054 (0.254)
{I}/{σI}	15.5 (3.8)
Completeness (%)	93.8 (91.4)
Unique reflections	47929
Redundancy	7.7
R_{work}	0.164
R_{free}	0.203
r.m.s.d. bonds	0.01
Overall B-factor (Å^2)	18.9
B-factor of iron in each molecule (Å^2)	13.0, 12.7
Average B-factor of waters (Å^2)	28.2
Wilson B-factor (Å^2)	17.7
Coordinate error[a] (Å)	0.09
PDB ID	1Y4T

Note: The numbers in parenthenses refer to the highest resolution shell.

[a] Coordinate error derived from maximum likelihood refinement.

Table 3-2 Geometry of the cFbpA chain A iron binding site.

Iron ligand angles	Degrees
Tyr146OH-FE-Tyr203OH	110.6
Tyr146OH-FE-Tyr202OH	86.8
Tyr146OH-FE-Tyr15OH	107.6
Tyr146OH-FE-His14NE2	92.9
Tyr202OH-FE-Tyr203OH	97.8
Tyr203OH-FE-His14NE2	79.7
His14NH-FE-Tyr15OH	95.2
Tyr15OH-FE-Tyr202OH	86.8

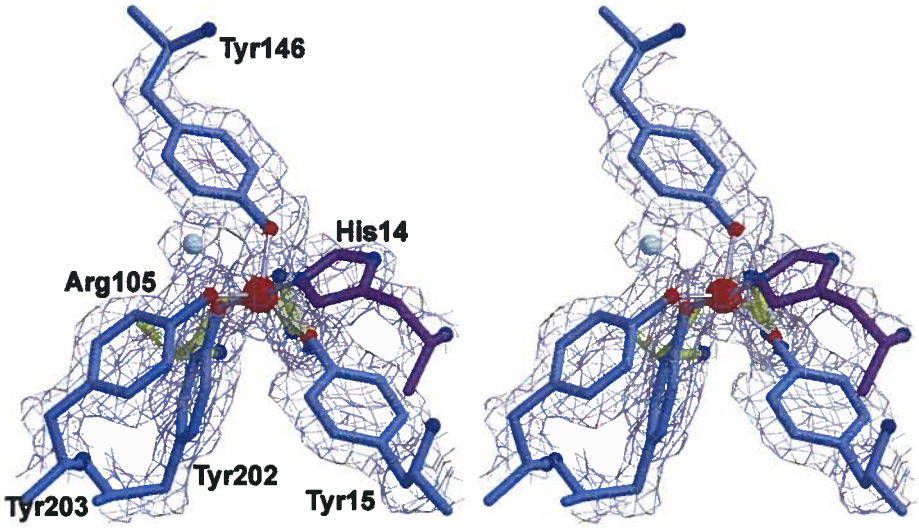

Figure 3-2 A stereoview of the cFbpA chain A iron binding site.

The 2 F_o-F_c representative electron density map is contoured at 0.8 σ. Tyrosines and water are dark and light blue, respectively. Histidine is purple, arginine is yellow and iron is represented by a red sphere. The nitrogen and oxygen atoms of the residues are coloured blue and red, respectively. The image was generated using MolScript (87) with changes by R. Esnouf and Raster3D (99).

iron-binding site in the *2Fo-Fc* map (Figure 3-2). The 4 coordinating Tyr residues are approximately 1.9 to 2.1 Ångström (Å) from the iron (Table 3-3) and have B-factors (measures of thermal motion and disorder) similar to that of the bound iron (13.0 $Å^2$). In contrast, His14 forms a weaker interaction with iron as shown by the increased ligand to iron bond distance (2.3 Å) and the elevated average B-factor of the imidazole ring (20.6 $Å^2$). Furthermore, the iron-histidine bond is 40° out of the imidazole plane. Instead, the imidazole plane of histidine approximately intersects with the OH atoms of Tyr146 and Tyr203 that are located 3.1 Å and 2.7 Å from His14 NE2, respectively (Figure 3-3).

Surrounding the iron site are networks of charged and polar amino acids (Figure 3-1, B). Most notably, 5 Arg residues (Arg13, Arg105, Arg107, Arg140, and Arg 183) are within 10 Å of the iron center. The closest non-coordinating group is the guanidinium of Arg105 (4.1 Å). Interestingly, Arg105 in the C-terminal domain is part of a relay of buried salt-bridges around one side of the iron site that includes the N-terminal domain residues Glu275, Arg13 and Asp18. In addition to connecting the N- and C-terminal domains, Arg105 lies within the hinge region. The N- and C- terminal domains are also connected through a H-bond interaction involving Asn237, also located in the hinge region but on the opposite strand, and Asp63 of the N-terminal domain. A third charge network involving Arg140, Asp182 and Arg107 is found solely in the C-terminal domain. In addition, 2 C-terminal domain residues form H-bonds with the OH atoms of the Tyr iron-ligands (the guanidinium of Arg105 with Tyr15 and the side chain amide of Asn200 with Tyr202).

Table 3-3 Ligand to iron bond distances in cFbpA chain A

Residue	Bond distance (Å)
His 14	2.3
Tyr 15	2.0
Tyr 146	2.0
Tyr 202	2.1
Tyr 203	1.9

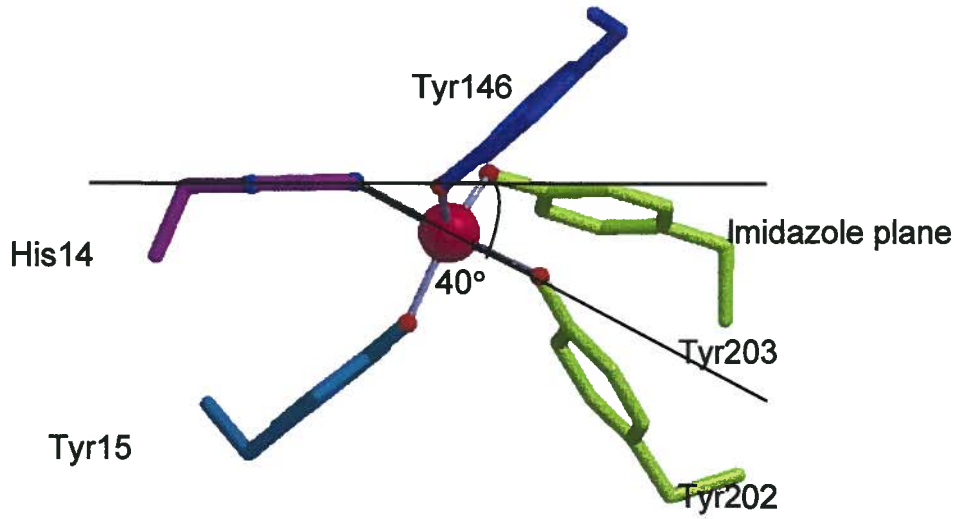

Figure 3-3 The angle formed between the His14 imidazole plane and the line joining His14 NE2 of cFbpA chain A with iron.

The color scheme is described in Figure 3-1. The iron ligands are labeled. The iron is represented by a red-pink sphere. The nitrogen and oxygen atoms of the residue side chains are coloured blue and red, respectively. The image was generated using Molscript (87) and Raster3D (99).

3.2.2 Iron-binding

The addition of iron to apo cFbpA gives an absorbance maximum at 440 nm, indicative of a ferric-tyrosinate interaction (117). Interestingly, addition of free ferrous iron or ferric iron chelated by oxalate results in significantly higher absorbance readings as compared to free ferric ions (Figure 3-4, panel A). Further addition of excess carbonate to the protein sample saturated with ferrous ions does not alter the absorbance reading.

Competition experiments with the iron-chelator pyrophosphate were used to define the affinity of cFbpA for iron (Figure 3-4, panel B). Increasing concentrations of pyrophosphate blue shifts and decreases the visible absorbance of both holo cFbpA and holo nFbpA. For holo cFbpA, a chelator:protein ratio of 2:1 reduces the initial absorbance reading to half. A ratio of 20:1 is needed for holo nFbpA indicating that the iron binding constant of cFbpA is likely within an order of magnitude of nFbpA.

3.2.3 Sequence analyses

The FbpA homologs found in the sequence database are derived from diverse prokaryotes including proteobacteria, cyanobacteria, Gram-positive bacteria and archaea. The trees generated by TREE-PUZZLE and ClustalW divide the sequences into 9 clusters (Figure 3-5 and Figure 3-6). Six Classes of FbpAs were defined on the basis of these 9 clusters as well as conservation of residues known to coordinate iron from the available FbpA crystal structures. The clusters correspond to individual classes except for Classes I, II and III which are composed of 2 clusters each. Classes I, II, and III contain more

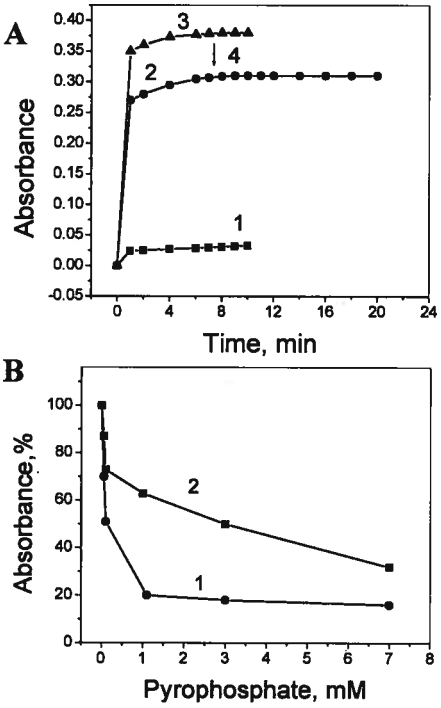

Figure 3-4 Anion-independent high-affinity iron binding to cFbpA.

A, Absorbance change at 440 nm of 0.055 mM apo cFbpA after the addition of 1) equimolar ferric chloride, 2) ferrous sulfate or 3) ferric oxalate in 200 mM NaCl, 10 mM Tris-HCl, pH 7.4. 4) Sodium bicarbonate (5.5 mM) was added after 10 min incubation of apo cFbpA with ferrous sulfate as indicated by arrow. B, Estimation of iron affinity to 1) cFbpA and 2) nFbpA by competition using sodium pyrophosphate.

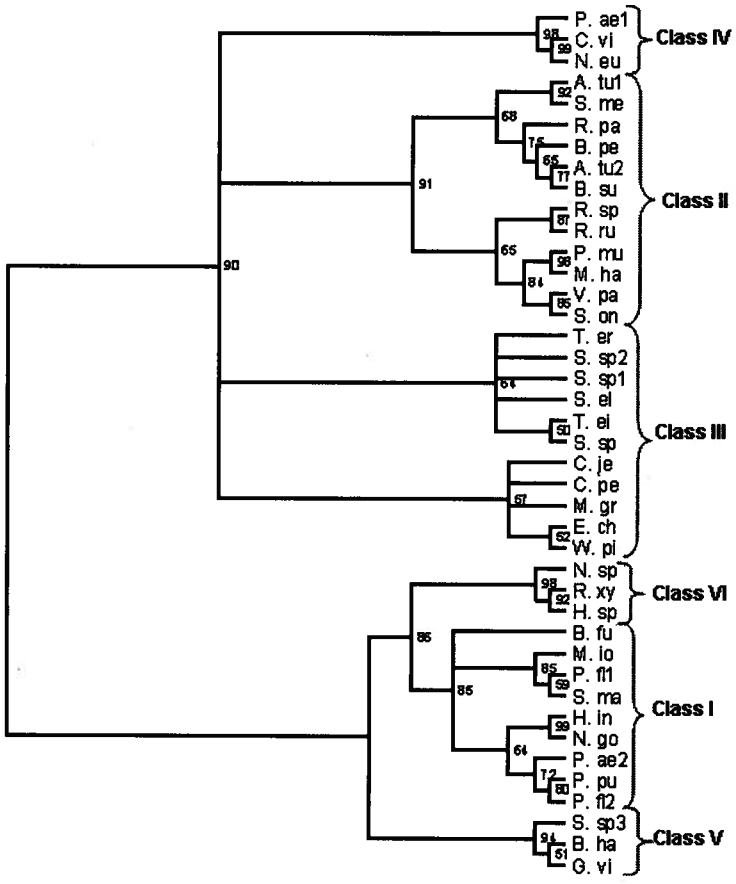

Figure 3-5 Unrooted tree of FbpA sequences generated with TREE-PUZZLE (132).

Six classes are indicated. The abbreviations used are (H.in) *Haemophilus influenzae* R2866 gi42632152. (N.go) *Neisseria gonorrhoeae* gi1098687. (P.ae2) *Pseudomonas aeruginosa* PA01 gi15599882. (P.pu) *Pseudomonas putida* KT2440 gi26991560. (P.fl2) *Pseudomonas fluorescens* PfO-1 gi23058165. (B.fu) *Burkholderia fungorum* gi22989044. (P.fl1) *Pseudomonas fluorescens* PfO-1 gi23060872. (R.xy) *Rubrobacter xylanophilus* DSM 9941 gi45546990. (M.lo) *Mesorhizobium loti* MAFF303099 gi13473018. (N.sp) *Nostoc* sp. PCC 7120 gi17228877. (G.vi) *Gloeobacter violaceus* gi37520583. (T.er) *Trichodesmium erythraeum* IMS101 gi23039548. (T.el) *Thermosynechococcus elongatus* BP-1 gi22298056. (S.sp) *Synechococcus* sp. PCC 6301 gi2125893. (B.pe) *Bordetella pertussis* Tohama I gi33592693. (A.tu2) *Agrobacterium tumefaciens* gi15887756. (R.pa) *Rhodopseudomonas palustris* CGA009 gi39937212. (A.tu1) *Agrobacterium tumefaciens* gi15887555. (S.me) *Sinorhizobium meliloti* gi15964482. (V.pa) *Vibrio parahaemolyticus* RIMD 2210633 gi28899265. (P.mu) *Pasteurella multocida* gi15601916. (M.ha) *Mannheimia haemolytica* gi3978164. (R.sp) *Rhodobacter sphaeroides* gi22959567.

(S.on) *Shewanella oneidensis* MR-1 gi24372333. (R.ru) *Rhodospirillum rubrum* gi22967044. (S.sp2) *Synechocystis* sp. PCC 6803 gi16329434. (E.ch) *Ehrlichia chaffeensis* gi4894577. (C.vi) *Chromobacterium violaceum* ATCC 12472 gi34497363. (C.je) *Campylobacter jejuni* subsp. jejuni NCTC 11168 gi15791562. (W.pi) *Wolbachia pipientis* wMel gi42520728. (B.su) *Brucella suis* 1330 gi23500440. (C.pe) *Clostridium perfringens* gi18309420. (H.sp) *Halobacterium* sp. NRC-1 gi15790051. (B.ha) *Bacillus halodurans* gi15613076. (P.ae1) *Pseudomonas aeruginosa* PA01 gi15600410. (N. eu) *Nitrosomonas europaea* ATCC 19718 gi30249032. (S.sp3) *Synechocystis* sp. PCC 6803 gi16330556. (M.gr) *Magnetospirillum gryphiswaldense* gi33945217. (S.sp1) *Synechocystis* sp. PCC 6803 gi16331793. (S.el) *Synechococcus elongatus* PCC 7942 gi45512924 (this record has since been replaced with gi46129860). (S.ma) *Serratia marcescens* gi134455. The tree was displayed with TreeView version 1.6.6 (114).

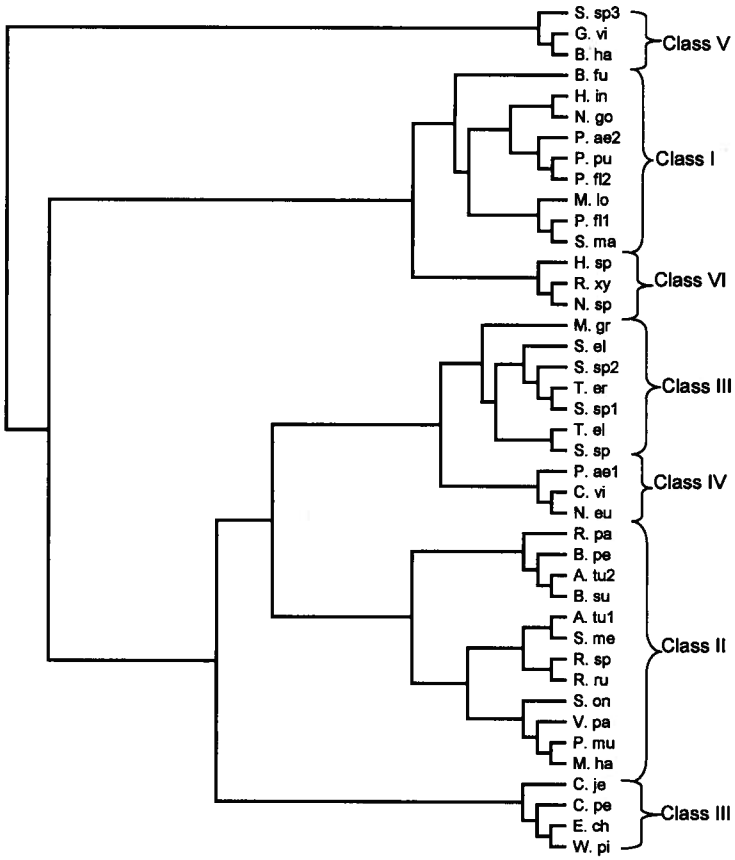

Figure 3-6 Neighbor joining tree produced from ClustalW (151).

Abbreviations are as for Figure 3-5. The tree was displayed with TreeView version 1.6.6 (114).

than 9 members each and include the structurally characterized nFbpA, mFbpA and cFbpA, respectively. Classes IV through VI contain 3 members each and are not yet structurally characterized. Class IV contains FbpAs from environmental bacteria whereas Class V and VI include FbpA homologs from prokaryotes that are non-pathogens as well as extremophiles and cyanobacteria.

The Class definitions are also consistent with observed insertions and deletions in the multiple sequence alignment (Figure 3-7). Sequences in Classes I, V, and VI have small deletions near alignment position 179 and only in Class I are 2 amino acids deleted. Furthermore, Class V has a 3 amino acid insertion relative to Classes I and VI near alignment position 235. Classes II and III are distinguished clearly from each other and all other FbpAs by single deletions at alignment position 39 and 214, respectively. Class IV can be distinguished from Classes II and III by a large deletion near alignment position 212.

Only 2 of the residues known to coordinate iron, Tyr202 and Tyr203 in cFbpA (Figure 3-1, panel B) corresponding to alignment positions 204 and 205 (Figure 3-7), are conserved in all except 1 FbpA sequence. The exception is the Class V FbpA from *Synechocystis sp.* PCC 6803 which appears to have diverged significantly from the family. A third Tyr coordinated to iron in *C. jejuni* (Tyr146) is conserved in half of the Classes (Class II, III and IV). The fourth iron ligand in cFbpA, Tyr15, is observed only in Class III and is conserved in most of these FbpAs. The remaining ligand, His14, is conserved in both Class I and most of Class III FbpAs.

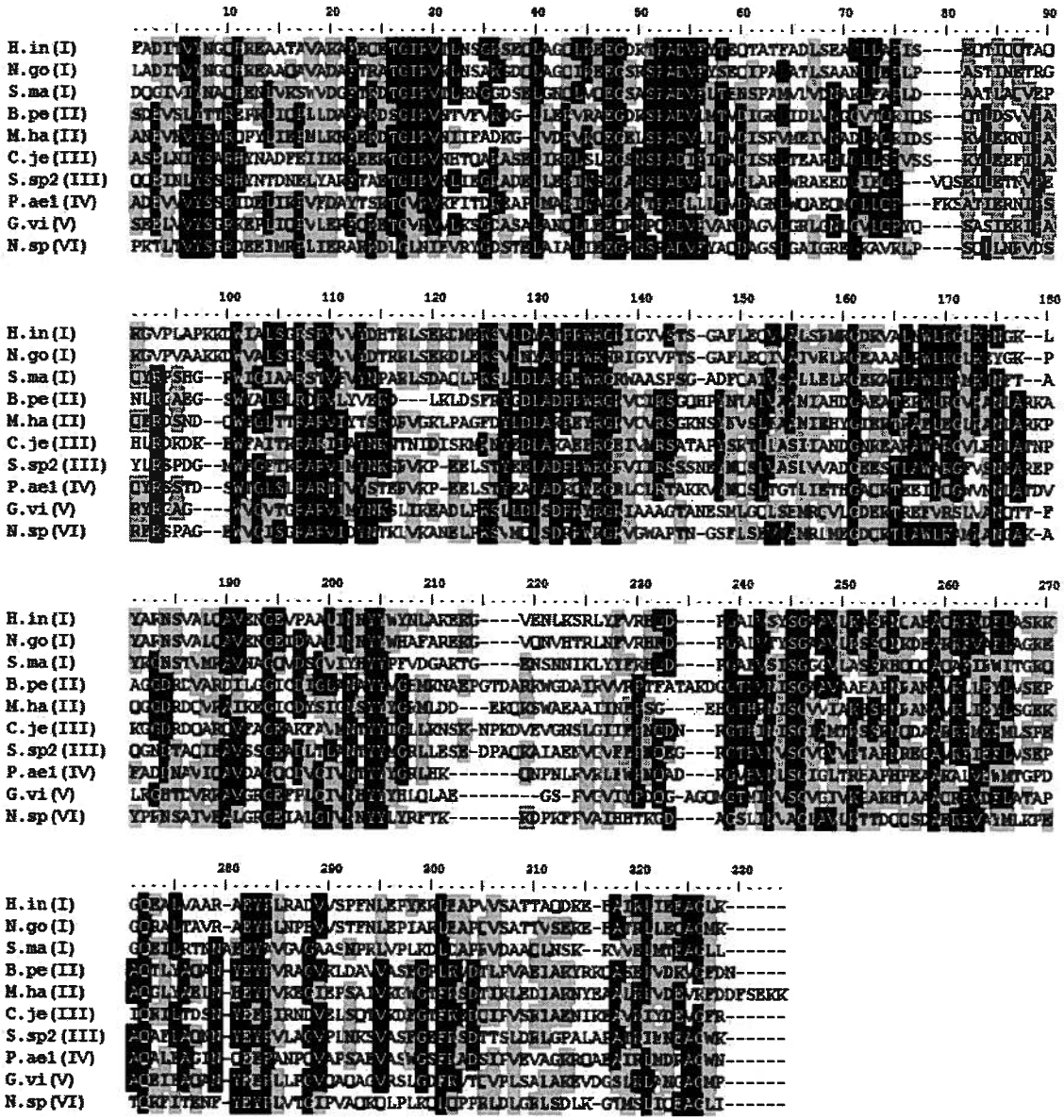

Figure 3-7 Representative alignment of a subset of FbpA sequences from Classes I to VI.

The abbreviations are as for Figure 3-5. The Class designation is indicated in parentheses. Black shading indicates absolutely conserved residues and grey shading indicates similar residues. The alignment was viewed using BioEdit (60).

3.3 Discussion

3.3.1 Crystallographic characterization of iron transport proteins

The obstacles that organisms face in the acquisition of ferric iron, due to its low solubility and reduction potential, are substantial. Consequently, iron binding and transport proteins bind iron with high affinity. The first picture by X-ray crystallography of a high affinity iron transport protein was of the mammalian transferrin-lactoferrin family (14). The transferrins show iron bound in an octahedral geometry not only by protein ligands (2 Tyr residues, a His and an Asp) but also by carbonate, a synergistic anion for iron binding. The crystal structures of bacterial iron transport proteins, hFbpA, nFbpA and mFbpA, also show iron bound using a combination of protein ligands and synergistic anions (1 His, 1 Glu, 2 Tyr residues, 1 water and 1 phosphate for hFbpA and nFbpA; 3 Tyr residues and 1 carbonate for mFbpA). Interestingly, the iron ligands in these bacterial FbpAs are not spatially equivalent to that of transferrin (32). As well, the carbonate binding site in mFbpA is displaced relative to the anion binding sites of hFbpA, nFbpA and transferrin. Nevertheless, these structures suggest an apparent requirement for a synergistic anion in ferric iron transport proteins. Surprisingly, the cFbpA structure in the closed conformation reveals unprecedented iron coordination incorporating only protein ligands. The unique iron binding mechanism in cFbpA establishes a new class of FbpAs, Class III.

The closed conformation of the crystal structure of iron-loaded cFbpA is defined in comparison to the holo hFbpA structure. Superimposition of 125 α-carbons from the cFbpA structure, representing the core of both domains, onto the equivalent α-carbons

from the hFbpA structure yields an r.m.s.deviation of 0.88 Å. In contrast, similar superimposition of both domains of the cFbpA structure with the apo hFbpA structure (1D9V) is not possible due to a 21° relative domain rotation about the apo hFbpA hinge region resulting in a more elongated conformation (31).

The unexpected result arising from the cFbpA structure is that iron is bound without the need for a synergistic anion in the closed conformation. Instead iron is coordinated solely by 5 protein derived ligands (His and 4 Tyr residues). Inspection of the absent site within the distorted octahedral geometry shows that anion access to this position is sterically hindered by the phenolate rings of Tyr15, Tyr202 and Tyr203 (Figure 3-2).

3.3.2 The role of the synergistic anion in FbpA proteins

The lack of a synergistic anion is surprising since these anions are thought to play critical roles in the initiation of iron binding and release in iron transport proteins. Carbonate is synergistic for iron binding to transferrin (136) and a low pH crystal structure suggests a role for bound carbonate in the initiation of iron release (96). For the Class I nFbpA, phosphate is proposed to pre-order the C-terminal iron half site (31) and facilitate iron binding by stabilizing a specific protein tertiary structure for iron binding (48). As well, phosphate is necessary for the stabilization of the closed conformation (17). Furthermore, the rate of iron release is influenced by the identity of the anion (41). In mFbpA (Class II), 3 C-terminal Tyr residues form the analogous half site eliminating the need for an anion (phosphate) at this position (141); however, a carbonate anion is

observed in the closed holo structure (PDB ID 1SI0) and is the only additional iron ligand (Figure 3-1, panel D) (144).

3.3.3 Anion-independence of cFbpA

Although a synergistic anion is not observed in the holo cFbpA structure, a combination of iron site residues conserved with either hFbpA or mFbpA may substitute for the functions of a synergistic anion. The presence of Tyr146 suggests a similar pre-ordered half site formed from 3 C-terminal Tyr ligands (Figure 3-1, panels A and B). As in hFbpA, the conserved N-terminal His14 (along with Tyr15 of cFbpA) creates a direct iron bridged link between the N- and C-terminal domains. In cFbpA, the near neutral pK_a of His and observed weaker interaction of His14 with iron in the crystal structure suggests a role for this residue in mediating iron release, similar to the role of carbonate in transferrin. Furthermore, the orientation of the histidine plane towards the Tyr146 and Tyr202 ligands suggests that these residues may interact in the process of iron binding and/or release.

That the anion is superfluous is further emphasized by spectroscopic observations that a synergistic anion is not required for high affinity iron binding to cFbpA (Figure 3-4). In addition, recombinant cFbpA is isolated from *E. coli* loaded with iron. These observations suggest a function for cFbpA as a component of a high affinity iron transport system in *C. jejuni*.

Binding studies show a preference by cFbpA for ferrous iron as opposed to the free ferric form (Figure 3-4, panel A), suggesting that cFbpA may facilitate ferrous iron

uptake in *C. jejuni*. In addition, cFbpA may be involved in the acquisition of the ferric form bound to biological chelators such as oxalate.

3.3.4 Phylogenetic characterization of FbpA proteins

Within the cluster containing cFbpA (Figure 3-5), 4 out of 5 sequences are from pathogenic bacteria proposed to have an intracellular stage within the host. Members of this cluster include *C. jejuni* and *C. perfringens,* for which the severity of infection is correlated with bacterial invasion (110, 164). *C. jejuni* is proposed to have an intracellular stage during invasion into the epithelium of the gut (82). *C. perfringens*, a Gram-positive anaerobe, is the causative agent of gas gangrene and has extensive invasive capacity (54). C. *perfringens* is proposed to exist within the cytoplasm of macrophages in the initial stage of infection (110). The remaining members are from *E. chaffeensis* and *W. pipentis* which are obligate endocellular symbionts. The unique structural and functional properties of cFbpA suggest a novel role for these FbpAs in iron uptake from within a host intracellular environment.

Ligand conservation is also observed within each of the different classes. Phylogenetic analyses of the Class III FbpAs show that the ligands are mainly conserved with few exceptions. One exception includes the FbpA homolog from *M. gryphiswaldense* that lacks the corresponding His14 and Tyr15 ligands due to a truncated amino terminus. Also, in the FbpAs from *W. pipientis* and *E. chaffeensis*, the residues aligned with His14 and Tyr15 of cFbpA are Lys and Glu indicating some change in iron ligation. The iron ligands observed within the crystal structures of Class I hFbpA and nFbpA and Class II mFbpA are conserved absolutely among the sequences of their

respective Class members. Classes IV through VI FbpAs likely coordinate iron differently than observed to date. The tree and conservation of known iron ligands suggest that Class IV FbpAs are similar to those from Class II; however, the residues in Class IV corresponding to those in the region around the carbonate anion in Class II are not conserved. Due to the limited number of members in Classes V and VI, only the 2 conserved tyrosines found across all classes can be readily identified as iron ligands. These 2 highly conserved tyrosines may then be used to construct a short sequence motif, N/YxYY, to identify new FbpA family members. Although Asn200 is not absolutely conserved since 3 out of 41 FbpAs contain a Tyr substitution, this Tyr is present in the FbpA from *Serratia marcescens* which is known to be involved in iron transport (9).

Interestingly, despite the different iron sites between the classes, nearby tertiary interactions are conserved. Comparison of the iron-binding site of cFbpA with the other classes shows that 6 residues are conserved among all FbpAs with few exceptions and all except Glu275 originate from the C-terminal domain (Figure 3-1, panel B, yellow; Table 3-4). Only 2 of these residues are iron ligands (Tyr202 and Tyr203). Conserved residues Arg105 and Arg107 are near these tyrosines and likely lower the pK_a of the phenolates to facilitate iron binding. Glu275 forms a conserved salt-bridge to Arg105. In the available crystals structures, Asn200 seems to assist in iron binding by either forming an H-bond to a Tyr ligand (Class II and III FbpAs) or by interacting with the synergistic anion (Class I FbpAs). Among FbpAs from Classes II, III, and IV, additional cFbpA iron site residues are fully conserved (Arg13, Tyr146, Asp182, Asn237) or mostly conserved (Asp63,

Table 3-4 Selected conserved residues that are not directly involved in iron binding within the FbpA Classes

FbpA Classes	Absolutely conserved	Mostly conserved (greater than 64 %)
Specific to Class III	-	Asp15 (18)
Between all Classes	Arg107 (105)	Arg109 (107), Asn202 (200), Glu281 (275)
All Classes except Class I	-	Arg10 (13), Asp60 (63), Asn243 (237) with one exception in one Class I FbpA
Class II, III, IV	Asp184 (182)	Arg142 (140)
Class II and III	-	Gln187 (185)

Note: Numbers refer to the position within the multiple sequence alignment (Figure 3-7). Numbers in parentheses refer to the corresponding cFbpA residues, where indicated.

Arg140) (Figure 3-1, panel B, dark purple). Hydrogen bonding networks that surround the iron site are composed of these residues along with the 6 residues conserved in most FbpAs. H-bonds linking the N- and C-terminal domains are formed from 4 of these residues (Arg13 and Glu275; Asp63 and Asn237) and are conserved between these Classes. Interestingly, in mFbpA the side-chain equivalent to Arg13 in cFbpA is displaced to form a H-bond to the synergistic carbonate; thus, 1 of the 2 H-bonds to the carboxylate group of Glu275 present in cFbpA is lost in mFbpA (Figure 3-1, panels B and D). These interdomain H-bond networks in the closed conformation are also maintained in Class I FbpAs using functionally equivalent residues (Figure 3-1, panel C).

Interestingly, some bacteria contain multiple FbpAs (Figure 3-5) spanning the different classes. Of the Class III cyanobacterial FbpAs, some are shown to function in iron uptake whereas others have adapted the iron binding function for alternative purposes. For example, *Synechocystis* sp. PCC 6803 contains 3 FbpAs, also known as IdiA homologs, 2 of which are members of Class III (S.sp1, S.sp2) and 1 is in Class V (S.sp3). The best characterized is S.sp2 (annotated in the genome sequence as slr1295) which is cytoplasmic and is involved in protecting photosystem II during iron limitation and oxidative stress (100). Although the exact mechanism by which S.sp2 protects photosystem II is not known (100), the iron binding properties are similar to other FbpAs (73). In contrast, S.sp1 (slr0513) is secreted into the periplasm (100, 152) and is likely a component of an iron uptake system (72). The sequences of both S.sp1 and S.sp2 have

iron ligands conserved with those of cFbpA suggesting similar iron coordination without a synergistic anion and mechanism of iron binding and release.

The conservation of the iron site between Class III FbpAs from *Campylobacter* and the cyanobacteria offers precedence for an evolutionary model whereby iron binding was present before the incorporation of various synergistic anion binding sites in other FbpAs. Cyanobacteria are believed to be the first oxygen evolving phototrophic organisms and may therefore be primarily responsible for the global conversion from an anoxic to oxic atmosphere (18). These microorganisms may have been the first to adapt to a reduced bioavailability of iron due to the local oxidation of ferrous to ferric ions (100). Thus, cyanobacteria may have developed one of the first iron uptake systems linking ferrous and ferric uptake, a component of which may have resembled cFbpA. Since early microorganisms exchanged genetic material through extensive lateral gene transfer (18), this early iron uptake system may have been readily acquired and modified by other prokaryotes. In contrast, a previous model proposed that FbpAs shared a common anion binding ancestor (32). Our model for FbpA evolution, involving divergence from an anion-independent iron binding protein ancestor, is more parsimonious.

3.3.5 Subsequently characterized anion-independent FbpA proteins

Since publication of this chapter (153), additional anion-independent FbpA proteins have been characterized. As predicted from the classification scheme, the crystal structures of the Class III FbpA proteins FutA1 and FutA2 from *Synechocystis* sp. PCC 6803 referred to in this chapter as S.sp2 and S. sp1, respectively, also show anion-

independent iron coordination similar to cFbpA (86). Furthermore, similarities in iron binding characteristics are observed between members of this class. For example, similar to cFbpA, FutA1 and FutA2 preferentially bind iron when presented in the ferrous form and free ferric iron poorly (12, 86). Furthermore, as observed for cFbpA, FutA2 binds ferric iron well when bound by a chelator (12).

Interestingly, a Class I FbpA from *Y. enterocolitica* (YfuA) was shown to coordinate iron without the requirement for a synergistic anion. YfuA is not shown in the phylogenetic tree due to the high sequence identity (87%) shared with the FbpA from *Serratia marcescens*. Iron was bound using the conserved protein residues (His, Glu, 2 Tyr residues) and water; however, instead of a phosphate anion, a spatially equivalent Asp is utilized to coordinate iron in a distorted octahedral geometry (142). Interestingly, this Asp is functionally conserved with the C-terminal iron binding residue Tyr 146 of cFbpA (alignment position 148 in Figure 3-7). All FbpA members within the same cluster as YfuA also show conservation of the Asp ligand, suggesting that this cluster within Class I may also coordinate iron without the requirement for a synergistic anion. As for the other Class I cluster that includes nFbpA and hFbpA, the Asp ligand is not conserved suggesting that this cluster utilizes a synergistic anion for iron binding.

Chapter Four: Small hinge motion by the anion-independent ferric binding protein from *Campylobacter jejuni*

4.1 Introduction

The ferric binding protein FbpA, classified within family 2 of the PBPs, is divided into six classes which vary in conservation of iron site ligands and utilization of synergistic anions. Based on homology to other PBPs, substrate-dependent FbpA conformations are important for productive interactions with the ABC transporters. To elucidate the function of the Class III anion-independent cFbpA in *C. jejuni* 81-176, a *cfbpA* deletion strain was constructed and characterized under iron-limitation. Furthermore, reverse transcription PCR was conducted to confirm that *cfbpA* is transcribed in an operon with ABC transporter genes, supporting a functional link. To elucidate the iron translocation mechanism of the anion-independent Class III cFbpA, conformational analyses of holo and apo cFbpA in solution using SAXS and x-ray crystallography were conducted. For comparison, SAXS analyses were also conducted for the Class I nFbpA from *Neisseria gonorrhoeae* that uses a synergistic phosphate. Interestingly, cFbpA undergoes limited hinge motion in solution whereas nFbpA undergoes large conformational changes. These differences suggest that the anion in nFbpA facilitates stabilization of an intermediate conformation for iron binding. The iron-reconstituted cFbpA crystal structure further supports the anion-independence of Class III cFbpA. The differences in conformational behavior of cFbpA and nFbpA suggest adaptation of the FbpABC transport mechanisms to acquire iron in different environments *in vivo*.

4.2 Results

4.2.1 cfbpA'ABC transcription as an operon in C. jejuni 81-176.

Sequence analysis suggests that *cfbpA* is the second gene of a c*fbpA'ABC* operon in *C. jejuni* 81-176 (Figure 4-1, panel A). To show that *cfbpA'ABC* are transcribed on a single transcript, regions containing the junctions between each of the genes were amplified by reverse transcription PCR (RT-PCR). PCR products were observed for each junction showing that *cfbpA'ABC* (locus tags *CJJ81176_0212* to *CJJ81176_0209)* is transcribed as an operon (Figure 4-1, panel B, WT). As a control, PCR reactions were also performed using the corresponding RNA sample as template. No PCR products were observed, indicating that genomic DNA was not a contaminant of the RNA sample (Figure 4-1, panel B, WT).

4.2.2 Construction and verification of non-polar mutation of the ΔcfbpA strain.

To explore the role of cFbpA in iron acquisition in *C. jejuni 81-176*, an internal region of 133 bp of *cfbpA* was deleted and replaced with a non-polar kanamycin resistance cassette (Figure 4-1, panel A). Southern analyses (Figure 4-2) also verified the correct insertion of the kanamycin resistance cassette into *cfbpA*. RT-PCR was used to verify that the *ΔcfbpA* strain did not disrupt transcription of the cFbpA'ABC operon (Figure 4-1, panel B, Δ*cfbpA*). The presence of PCR products corresponding to each gene junction, including the *cfbpBC* downstream of the disruption cassette, confirmed that the *ΔcfbpA* mutation is likely to be non-polar. PCR reactions using the corresponding RNA

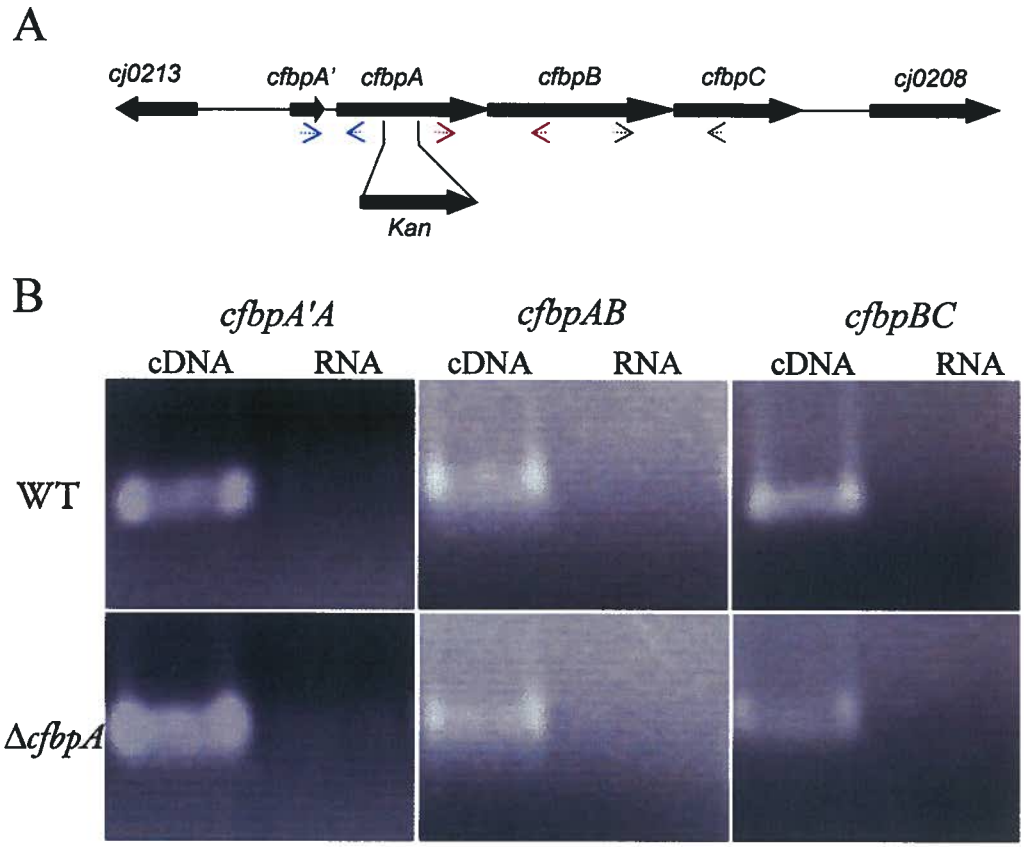

Figure 4-1 Genomic context of *cfbpA* and construction of the Δ*cfbpA* strain.

A, Genomic context of c*fbpA* in *C. jejuni* 81-176 wild-type (WT) showing the approximate location of the deleted region and insertion of the kanamycin cassette in the Δ*cfbpA* strain. The block arrows show the open reading frames. Panel A is not drawn to scale. B, Analysis of transcription of c*fbpA'ABC* in *C. jejuni* 81-176 WT and the Δ*cfbpA* strain by RT-PCR. Primer sets, indicated by the like colored dotted arrows in panel A, were used to amplify regions containing the junctions between *cfbpA'* and *cfbpA* (*cfbpA'A*, 572 bp), *cfbpA and cfbpB* (*cfbpAB*, 1015 bp), and *cfbpB* and *cfbpC* (*cfbpBC*, 864 bp). As controls, the corresponding PCR reactions were also conducted using RNA templates.

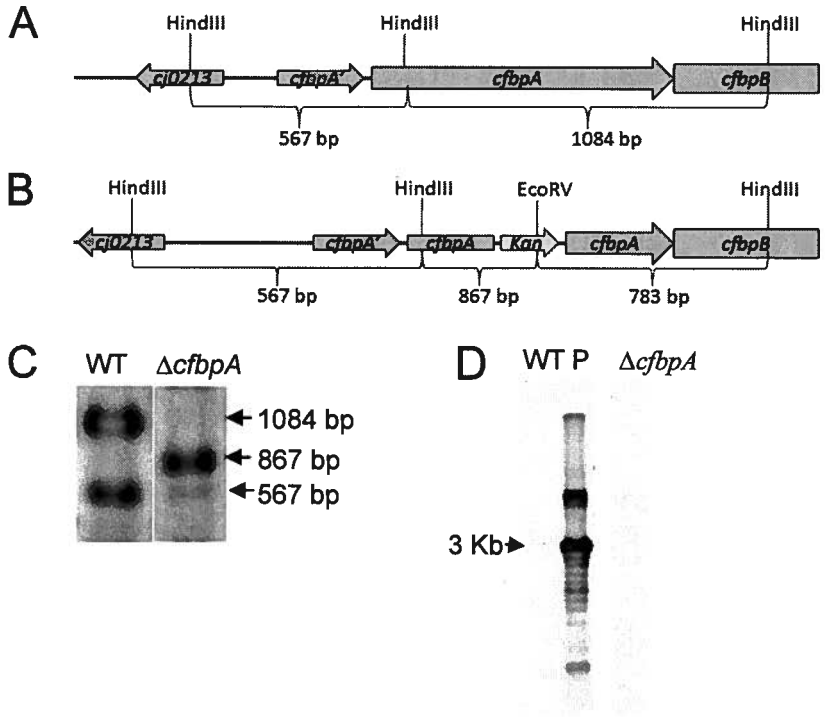

Figure 4-2 Southern blot analyses of *C. jejuni* 81-176 (WT) and *ΔcfbpA* strain.

The genomic DNA from WT and the Δ*cfbpA* strains were restriction digested with HindIII and EcoRV for Southern analyses. Panels A and B show the HindIII and EcoRV restriction sites (where present) of the *cfbpA* gene region in *C. jejuni* 81-176 (WT) and the Δ*cfbpA* strain, respectively. The corresponding sizes (bp) of the fragments produced following digestion with HindIII and EcoRV are shown. Gene names are indicated within the block arrows showing the open reading frame. *Kan* refers to the non-polar kanamycin resistance cassette. Panels A and B are not drawn to scale. C, Southern blot of the WT and the Δ*cfbpA* strains using the *cfbpA* gene as a probe. The arrows show the expected hybridization signals of the WT (1084 bp and 567 bp) and the Δ*cfbpA* (867 bp and 567 bp) strains. D, Southern blot of the WT and the Δ*cfbpA* strains using the *pBluescript II SK(-)* vector as a probe. P refers to the *pBluescript II SK(-)* vector control sample that is incompletely digested with EcoRV. As expected, no hybridization signals are observed for the WT strain. No hybridization signals are observed for the Δ*cfbpA* strain confirming that the insertion of the kanamycin resistance cassette occurred by a double crossover event. The arrow shows the expected hybridization signal for *pBluescript II SK(-)* vector digested with EcoRV.

did not yield amplicons, indicating no contaminating genomic DNA (Figure 4-1, panel B, Δ*cfbpA*). Quantitative RT-PCR could also be conducted to address the possibility that the insertion of the kanamycin resistance cassette into *cfbpA* may have affected transcript stability.

4.2.3 Impaired growth of the ΔcfbpA mutant under iron limitation.

Growth was monitored in biphasic MH-TV media by OD_{600} (Figure 4-3, panel A) and colony forming units (CFU)/ml (Figure 4-3, panel B) over 24 hours for *C. jejuni* 81-176 wild-type (WT) and Δ*cfbpA* strains. After 24 hours, growth was not monitored further due to oxidative stress effects. In iron-replete MH-TV media, both strains grew similarly. Addition of desferal to MH-TV media to achieve iron limitation also impeded the growth of both WT and Δ*cfbpA* strains. However, at 24 hours of incubation under iron limitation, impaired growth was observed and significantly fewer viable Δ*cfbpA* were recovered compared to the WT strain, indicating that the Δ*cfbpA* strain is more severely affected under the iron limited conditions compared to WT (Figure 4-3).

4.2.4 Iron-reconstituted cFbpA crystal structure.

cFbpA binds ferric iron rapidly when supplied in the form of a weak chelate such as ferric oxalate (153). Chelated ferric iron is present in iron rich media such as Mueller Hinton as well as in the intestinal environment. To explore the conformation and iron binding mechanism of cFbpA treated with ferric oxalate, the crystal structure was obtained. The iron-reconstituted cFbpA has two domains, linked by anti-parallel β strands containing the hinge region, with the iron binding site located at the domain

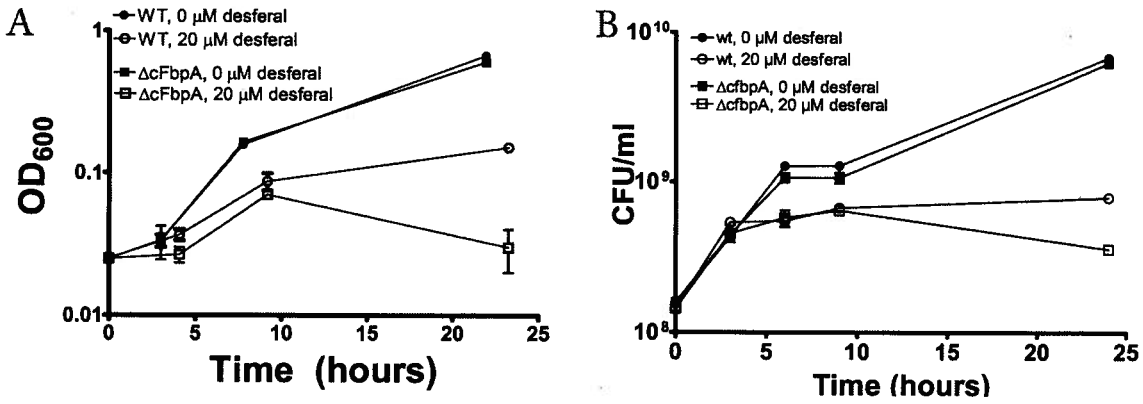

Figure 4-3 Impaired growth of the Δc*fbpA* mutant in biphasic MH-TV media plus desferal.

Wild-type (WT) *C. jejuni* 81-176 and the Δ*cfbpA* mutant were grown overnight in MH-TV biphasic media and diluted to 0.025 OD_{600} prior to the initiation of growth studies. *C. jejuni* 81-176 WT (•) and the Δ*cfbpA* mutant (■) were grown in MH-TV biphasic media. *C. jejuni* 81-176 WT (○) and the Δ*cfbpA* mutant (□) were grown in MH-TV biphasic media with iron chelated by 20 μM desferal. All assays were conducted in microaereobic conditions without agitation. Each data point is the mean and the error bars represent the standard error. A, Samples were grown in triplicate and OD_{600} measured at indicated time points over 24 hours of incubation. Student paired t-test shows statistically significant differences between WT and ΔcFbpA in MH-TV media plus 20 μM desferal at the 24 hour time point (two tailed p value = 0.0091). B, Samples were harvested at indicated time points over 24 hours of incubation and plated in triplicate to obtain CFU/ml. Student paired t-test shows statistically significant differences between WT and ΔcFbpA in MH-TV media plus 20 μM desferal at the 24 hour time point (two tailed p value = 0.0055).

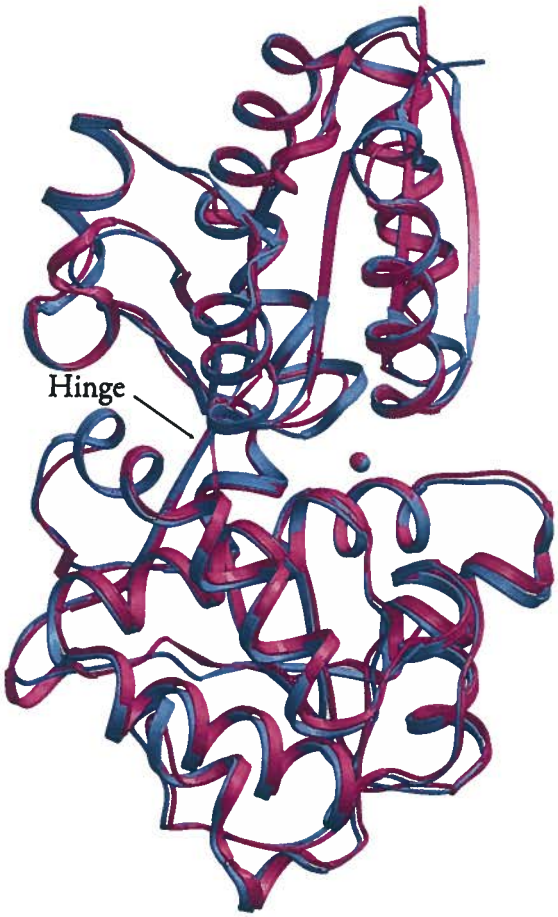

Figure 4-4 Least-squares superimposition of the N-terminal domains of holo cFbpA (1Y4T, chain A, cyan) and iron-reconstituted cFbpA (magenta).

Compared with holo cFbpA (1Y4T), the C-terminal domain of the iron-reconstituted cFbpA is rotated slightly towards the N-terminal domain to yield a more closed conformation. Iron and carbon atoms are colored to match the backbone of the respective structures. This figure was made using Molscript (87) and Raster3D (99).

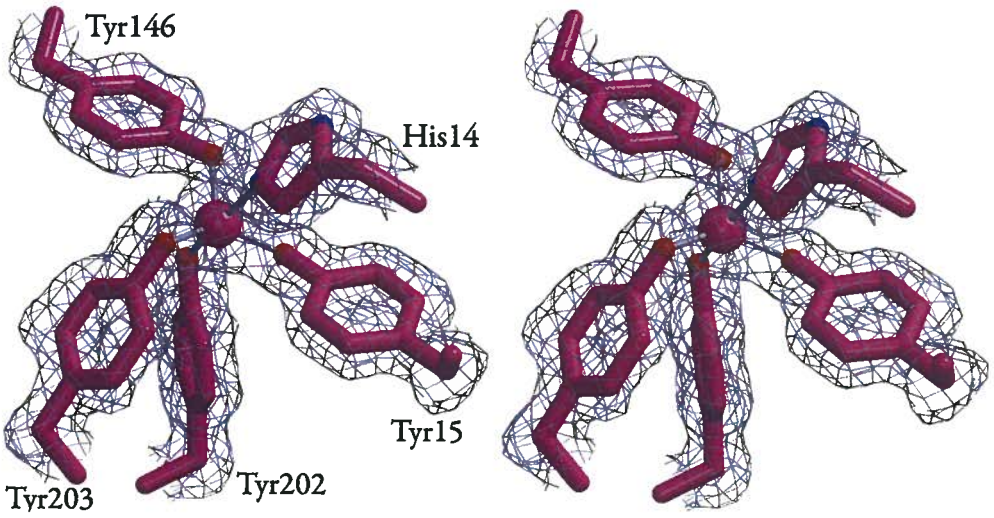

Figure 4-5 A stereoview of the 5 protein ligands coordinating iron in iron-reconsituted cFbpA.

The weighted $2F_o$-F_c electron density (gray) is contoured at 0.8 σ. The iron atom is represented as a magenta sphere. Carbon atoms are colored in magenta, the nitrogen atoms are colored in blue and the oxygen atoms are in red. This figure was made using Molscript (87) with changes by R. Esnouf and Raster3D (99).

Table 4-1 Data collection and refinement statistics.

Crystal	**cFbpA**
Wavelength (Å)	0.974609
Resolution range (Å)	48.8 – 1.6 (1.66 – 1.60)
R_{merge}	0.106 (0.196)
{I}/{σI}	8.6 (3.0)
Completeness (%)	90.9 (73.9)
Unique reflections	38962
Redundancy	12.9
R_{work}	0.145
R_{free}	0.186
r.m.s.d. bonds (Å)	0.02
Overall B-factor ($Å^2$)	15.5
B-factor of iron ($Å^2$)	10.4
B-factor of waters ($Å^2$)	27.7
Wilson B-factor ($Å^2$)	13.3
Coordinate error[a] (Å)	0.05
PDB ID	3E13

Note: Values reported in parentheses refer to the highest resolution shell.

[a] Coordinate error derived from maximum likelihood refinement.

interface (Figure 4-4). The N-terminal domain is comprised of a central 5 stranded β-sheet surrounded by 6 α-helices. The C-terminal domain is comprised of a central 3 stranded β-sheet surrounded by 8 α-helices. Iron is coordinated by two N-terminal domain His and Tyr residues and three C-terminal domain Tyr residues, in a distorted octahedral geometry (Figure 4-5). No density for oxalate is observed in the iron site. The iron-reconstituted cFbpA structure displays excellent stereochemistry, with 95.2% of the residues residing in the most favored region and the remaining residues in the allowed region of a Ramachandran plot (91). Data collection and refinement statistics are summarized in Table 4-1.

Least-squares superimposition of the α-carbon atoms of residues 5 to 321 of the iron-reconstituted cFbpA structure with those of the as isolated holo cFbpA structure (PDB ID 1Y4T) gave an r.m.s.d. of 0.43 Å showing that the backbones of these structures are very similar. However, the iron-reconstituted crystal structure has an overall conformation that is slightly more 'closed' when compared with as isolated holo cFbpA (Figure 4-4). The iron site ligands adopt similar conformations (Figure 4-5) as in the as isolated holo cFbpA structure (Figure 3-2).

4.2.5 SAXS analyses of cFbpA and nFbpA

SAXS is a low resolution method used to elucidate conformation and conformational changes of macromolecules in solution (147). To elucidate the conformations of cFbpA and nFbpA in solution under conditions similar to that of the periplasmic environment, SAXS data were collected at pH 7.0. For the nFbpA protein

Table 4-2 Radii of gyration for the SAXS protein samples

Protein	Radius of gyration, Rg (Å)	Change in Rg (Å)
Apo nFbpA	21.99 ± 0.01	0.91
Holo nFbpA	21.08 ± 0.01	
Apo cFbpA	21.40 ± 0.00	0.46
Holo cFbpA	20.94 ± 0.01	

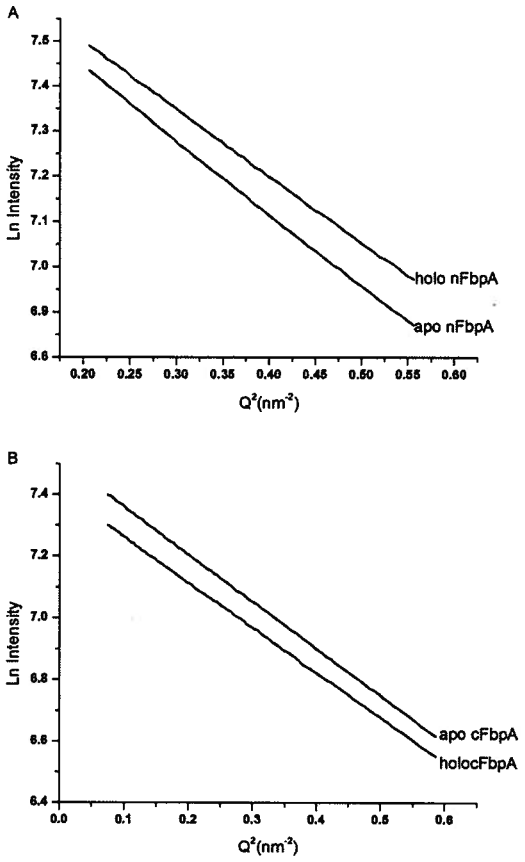

Figure 4-6 Guinier plots of apo and holo nFbpA and cFbpA.

A, Guinier plots of holo and apo nFbpA. B, Guinier plots of holo and apo cFbpA. The radius of gyration (Rg) was obtained from Crysol and was derived from the slope of the Guinier plot.

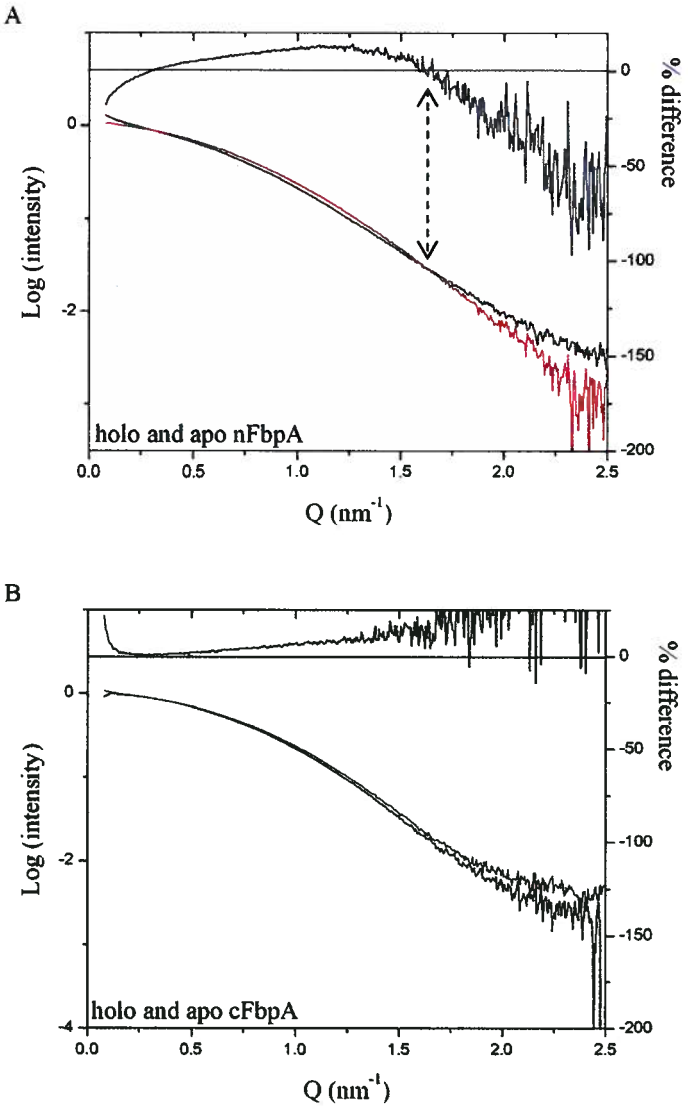

Figure 4-7 Solution X-ray scattering of apo and iron bound nFbpA and cFbpA.

A, The SAXS curves for holo and apo nFbpA showed a crossover (indicated by the dotted arrow) of the curves at 1.6 nm^{-1} typical for a protein that undergoes a large conformational change. B, Experimental SAXS curves of apo and holo cFbpA showed no crossovers indicating only small conformational changes in solution upon iron binding. In each panel, the SAXS curve for the iron loaded protein sample is red. The SAXS curve for the apo protein is black. The scattering curves are a plot of momentum transfer Q (a function of the scattering angle) versus the log of the scattering intensity. Differences between the scattering intensities for the holo and respective apo protein are plotted above as a percentage of the apo protein signal.

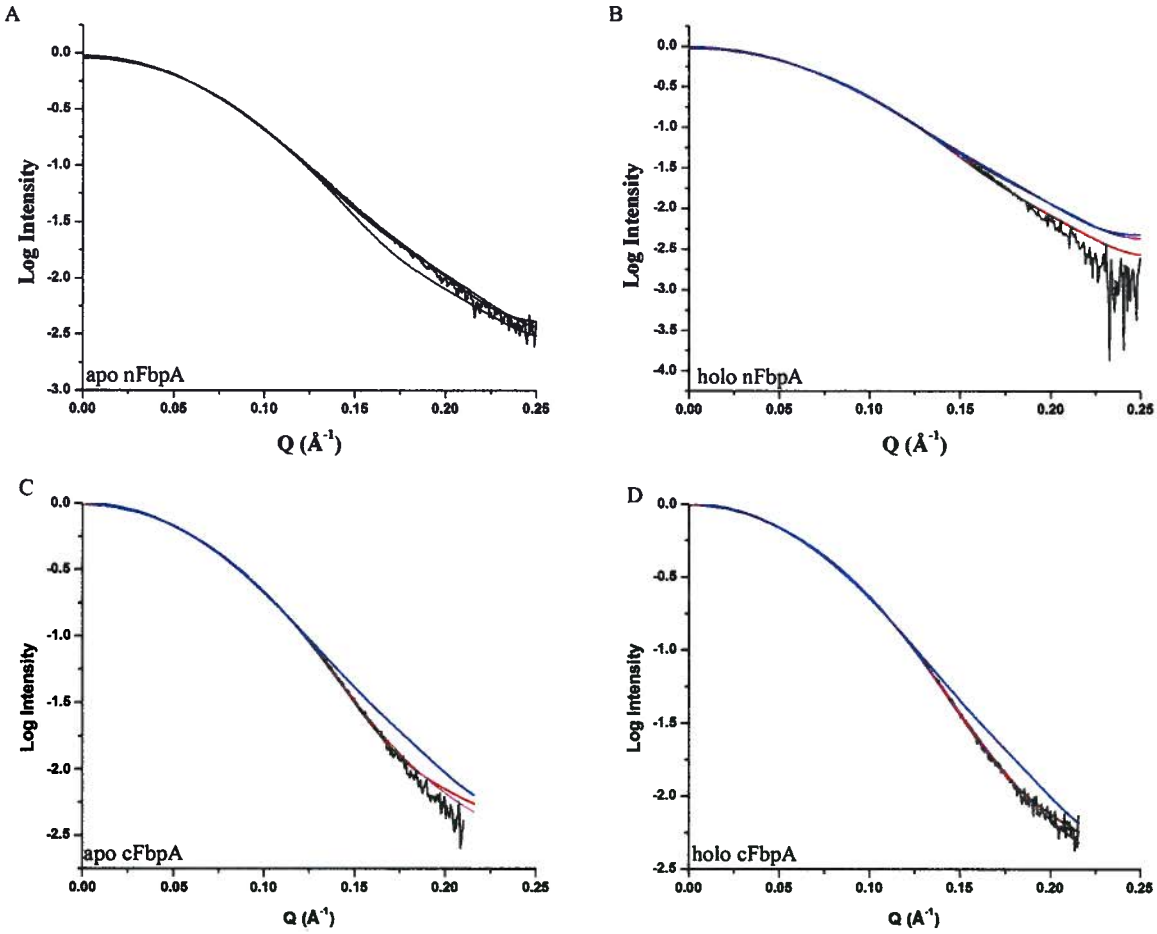

Figure 4-8 Comparison of theoretical scattering from crystal structures and *in silico* models (colored lines) with SAXS data (black lines) from nFbpA and cFbpA.

In all panels, the red curve refers to the closed crystal structure model, the purple curve refers to the ajar model and the blue curve refers to the open model. Interdomain angles for open and ajar models are given in parentheses. A, For the apo nFbpA SAXS data, fits of an *in silico* open model (57°), ajar crystal structure model (24°) and closed crystal structure model gave χ^2 values for the goodness of fit of 6.0, 9.4 and 15.9, respectively. B, For the holo nFbpA SAXS data, fits of the closed crystal structure model, ajar crystal structure model (24°), and an *in silico* open model (57°) gave χ^2 of 7.0, 6.7 and 7.7, respectively. C, For the apo cFbpA SAXS data, the fit of the ajar *in silico* model (15°), closed crystal structure model and open model (57°) gave χ^2 of 3.6, 5.1, and 10.3, respectively. D, For the holo cFbpA SAXS data, the fit of the closed crystal structure model, ajar *in silico* model (15°), and open model (57°) gave χ^2 of 3.1, 2.2, and 9.9, respectively.

samples, the radius of gyration (Rg) was reduced by 0.91 Å upon reconstitution with iron as calculated over the momentum transfer range of 0.459 and 0.756 nm^{-1} (Table 4-2, Figure 4-6). Comparison between the scattering curves of holo and apo nFbpA showed a crossover at a momentum transfer of 1.6 nm^{-1} (Figure 4-7, panel A), suggesting a large conformational change due to iron binding. In contrast, the iron-dependent reduction in the radius of gyration for the cFbpA protein samples was 0.46 Å as calculated over the momentum transfer range of 0.279 and 0.771 nm^{-1} (Table 4-2, Figure 4-6). The solution X-ray scattering curves of the holo and apo cFbpA samples were much more similar and no crossover was observed (Figure 4-7, panel B).

To further characterize the solution conformations of nFbpA and cFbpA, structural models were compared to the available SAXS data with the program Crysol. For apo nFbpA, a theoretical scattering curve of an *in silico* open model with an inter-domain angle of 57° provided a better fit to the SAXS data of apo nFbpA (χ^2=6.0, Figure 4-8, panel A blue) than the curves generated from the ajar crystal structure 1R1N with an interdomain angle of 24° (χ^2=9.4, Figure 4-8, panel A purple), or the closed crystal structure 1D9Y (χ^2= 15.9, Figure 4-8, panel A red). For the holo nFbpA SAXS data, the overall shape of the theoretical curve for the closed crystal structure model (χ^2=7.0, Figure 4-8, panel B red) provided a better fit than the ajar crystal structure (χ^2=6.7, Figure 4-8, panel B purple) and *in silico* open model (χ^2=7.7, Figure 4-8, panel B blue). However, all of the models did not fit as well in the high Q range (Q=0.15 to 0.25 $Å^{-1}$), implying additional conformational differences not included in the models.

The behavior of cFbpA in solution was distinct from that observed for nFbpA. For the apo cFbpA SAXS data, an *in silico* model with a 15° hinge angle provided a better fit to the SAXS data (χ^2=3.4, Figure 4-8, panel C purple) compared with the closed crystal structure (χ^2= 5.1, Figure 4-8, panel C red). For the holo cFbpA SAXS data, both the closed crystal structure of cFbpA (χ^2=3.1, Figure 4-8, panel D red) and the *in silico* model with a 15° hinge angle (χ^2= 2.1, Figure 4-8, panel D purple) provided good fits to the SAXS data. Additional *in silico* models with hinge angles greater than 15° provided poor fits to the SAXS data. In contrast to nFbpA, a model exhibiting a 57° angle (Figure 4-8, panel C blue) provided a poor fit to the apo cFbpA SAXS data (χ^2=10.3). This model also poorly fit the holo cFbpA SAXS data (χ^2=9.9, Figure 4-8, panel D blue).

4.3 Discussion

4.3.1 cFbpA facilitates iron uptake in C. jejuni 81-176

Here, we show that cFbpA mediates iron acquisition in *C. jejuni* 81-176 when grown in biphasic MH-TV media in the presence of 20μM desferal, an iron chelator (Figure 4-3). Subsequent iron transport across the inner membrane is likely facilitated by a cFbpA-dependent ABC transport system. RT-PCR reactions showed that *cfbpA* is co-transcribed with *cfbpA'*, *cfbpB*, and *cfbpC* in *C. jejuni* 81-176, suggesting a likely functional connection between these ABC transporter components (Figure 4-1, panel B). Furthermore, studies in another strain of *C. jejuni* (NCTC 11168) show that the permease component cFbpB, encoded by *cj0174c* of the cFbpABC transport system (*cj0176c-cj0173c*), facilitates iron uptake from lactoferrin (103). An outer membrane transferrin/lactoferrin receptor (encoded by *cj0178*) was identified and shown to have a

major role in iron uptake from lactoferrin and transferrin (103). In addition, an outer membrane enterobactin receptor CfrA also facilitated iron uptake from lactoferrin (103). Surprisingly, the outer membrane receptors encoded by *cj0178* and *cfrA* genes are missing in the highly invasive *C. jejuni* 81-176 strain (67). Currently for *C. jejuni* 81-176, the iron source(s) for cFbpA and the iron transport mechanism across the outer membrane are unknown. As for translocation across the inner membrane, iron import likely occurs through interaction of holo cFbpA with the permease. Based on homology with other PBP-dependent ABC transporters, the closed conformation of cFbpA likely initiates iron transport by promoting a productive interaction with the permease. In addition to conformation, the mode of iron binding influences the iron release mechanism (20).

4.3.2 SAXS analyses of flexible proteins

To gain insight into the role of cFbpA iron-dependent conformations in iron transport, small angle x-ray scattering (SAXS) studies were undertaken. For comparison with anion-independent cFbpA, SAXS analyses were also conducted with anion-dependent nFbpA. Conformational behavior in solution of PBPs such as MBP have previously been elucidated by SAXS (139). SAXS is especially useful for proteins with conformational flexibility, such as PBPs, since each crystal structure provides a snapshot of a conformation that is present in solution. For example, SAXS analyses of human apo lactoferrin show that both lobes adopt open conformations in solution (57). However, in one crystal form of apo lactoferrin, the C lobe has a closed conformation (4) whereas in another form, an open conformation is present (15).

4.3.2.1 Anion-independent cFbpA undergoes small hinge motion

Only small conformational changes were observed for cFbpA upon iron binding (Table 4-2, Rg decrease of 0.46 Å). Furthermore, no crossovers of the apo and holo cFbpA SAXS curves were observed, showing that cFbpA did not undergo large hinge motion upon iron binding. Also, fitting of models to both of the apo and holo cFbpA SAXS data further support a limited range of hinge motion. The acceptable models suggest that both the closed conformation observed in crystal as well as a conformation with a 15° hinge angle are accessible in solution for both apo and holo cFbpA (Figure 4-8, panels C and D). For both apo and holo cFbpA, models with greater than 15° hinge angles provided poor fits to the apo cFbpA SAXS data. Interestingly, a similar hinge angle of 16° has been observed previously in an apo crystal structure of another FbpA from *Synechocystis* sp. PCC 6803 (FutA1), which also binds iron without the requirement for a synergistic anion (86).

4.3.2.2 Anion-dependent nFbpA undergoes large hinge motion

The SAXS curves obtained for nFbpA showed the classic crossing over of the apo and holo curves (Figure 4-7, panel A) that is typically seen in periplasmic binding proteins which undergo large scale interdomain movement (138). For example, a crossover of the apo and substrate bound SAXS curves is observed for MBP which undergoes a 39 ° hinge motion upon substrate binding (138). In solution, holo nFbpA exhibited a more closed conformation compared with apo nFbpA, as shown by the decrease in the Rg by 0.91 Å (Table 4-2). These results are in agreement with a more closed conformation deduced from faster migration in native gels (109). Fitting of models

to the apo nFbpA SAXS data suggest that interdomain angles larger (greater than 57°) than observed in crystal for any FbpA are accessible in solution. For holo nFbpA, the closest fit to the SAXS data was achieved by the closed crystal structure. However, the closed structure could not provide a good match for the SAXS curve in the high momentum range (0.15 to 0.25 nm^{-1}) which may be due to the holo protein sampling open and ajar conformations while remaining primarily in the closed conformation in solution. Previously, Boukhalfa et al. suggested that holo nFbpA undergoes conformational changes between the open and closed states and that these conformational changes are proposed to explain the observed lability of the synergistic phosphate anion (20).

4.3.2.3 Suggested role for anion in conformation

Interestingly, conformational differences are observed between the anion-dependent nFbpA and anion-independent cFbpA. These differences suggest that the anion may have a role in effecting conformation. Previously for nFbpA, phosphate was proposed to enhance iron binding by stabilizing a specific protein structure (48). As well for mFbpA, the closed conformation crystal structure of formate-bound apo mFbpA also suggests a role for the anion in influencing protein conformation (144). Formate is structurally similar to carbonate and is bound in the carbonate binding site of apo mFbpA (144). Carbonate was therefore proposed to induce conformational changes of mFbpA prior to iron binding (144).

4.3.3 Iron transport models for Class III cFbpA and Class I nFbpA

The models proposed for Class III cFbpA and Class I nFbpA are based on the general principles of other characterized PBP-dependent ABC transport systems (69, 111). Overall, the substrate bound PBPs exhibit distinct conformations from the apo form which are then able to form productive interactions with the inner membrane permease. The differences in conformational behaviour for cFbpA and nFbpA suggest differences in the mechanisms for iron transport within *C. jejuni* and *Neisseria* sp..

For anion-independent cFbpA, the permease is proposed to form a productive interaction with only the closed conformation of holo cFbpA, since cFbpA does not utilize a synergistic anion in the iron-binding site and undergoes a limited conformational change between the holo and apo forms. Additional support for this model is derived from the iron-reconstituted holo cFbpA crystal structure (Figures 4-3, 4-4). cFbpA binds free ferric iron poorly; however, ferric iron is readily bound in the presence of a 100 molar excess oxalate (153). The crystal structure of the cFbpA reconstituted with ferric-oxalate shows iron bound similarly to as isolated holo cFbpA (1Y4T) (153). In both structures, iron is coordinated by only protein ligands and no synergistic anion. Thus, although oxalate facilitates iron loading, presumably by chelation, exchange with protein ligands is required upon formation of the closed conformation. Following initiation of productive interaction of the closed conformation holo cFbpA with the permease (cFbpBC), the mechanism of iron release is currently unknown.

For anion-dependent nFbpA, the permease is proposed to form a productive interaction with only holo nFbpA conformations distinct from apo nFbpA, such as

phosphate-bound holo nFbpA. This model therefore proposes that although nFbpA may bind iron using other synergistic anions (42, 64), only the holo nFbpA complexes that yield conformations distinct from apo nFbpA are candidates for initiating productive interactions with the inner membrane permease. A previous model for iron transport across the inner membrane by nFbpA involves synergistic anion exchange since the anion identity influences iron binding affinity and reduction potential (64). This proposal does not exclude the possibility that additional anions may be involved in the iron release process following productive interaction with the permease.

Since nFbpA and hFbpA are located within the same Class I FbpA and bind iron similarly using conserved iron site ligands and a phosphate anion, FbpA mediated iron transport across the inner membrane is likely to be similar in both *Neisseria* sp. and *H. influenzae*. Recently for hFbpA, another model was proposed whereby the role of the inner membrane permease is to capture and stabilize an open conformation of holo hFbpA prior to iron translocation (76). Subsequent iron transfer to the permease is proposed to be facilitated by the lower iron binding affinity of hFbpA in the open conformation compared with the higher iron binding affinity of the closed conformation of hFbpA. This model was derived from mutagenesis studies of *H. influenzae* strains harboring mutated hFbpA proteins impaired for phosphate binding. In proposing this model, the open conformers observed in crystal structures of the mutated hFbpA proteins are assumed to be representative of the active conformations that facilitated iron acquisition in a *H. influenzae* bioassay (76).

Although the conformations observed in the crystal structures are likely present in solution, our SAXS results of apo and holo nFbpA showed that the available crystal structures are not fully representative of the conformations seen in solution. Furthermore, native gel experiments show that holo nFbpA in the absence of a synergistic anion exhibit conformations present in both of the apo and phosphate-bound holo nFbpA protein samples (17). Thus, in addition to the open crystal conformations of the mutated holo hFbpA proteins, other conformations distinct from the apo conformation may also be present within the bacterium. Therefore, the observance of open crystal structure conformations cannot exclude the possibility that other conformations are initiating productive interactions with the permease. hFbpA mediated iron transport may therefore occur similarly to the model proposed for nFbpA, in which holo protein conformation(s) distinct from the apo protein conformation initiate productive interactions with the inner membrane permease. Following the initiation of ATPase activity, the permease may then stabilize an open conformation of holo hFbpA prior to iron translocation. The lowered iron binding affinity of hFbpA in the open conformation may then facilitate iron transfer to the permease. Interestingly, diminished growth of the *H. influenzae* strains expressing mutated hFbpA versus wild-type hFbpA proteins was observed (76). The diminished growth may be attributable to the decreased stabilization of the closed conformation affecting efficiency of initiation of iron transport; furthermore, the loss of the phosphate binding site may also have additional effects possibly impacting the mechanism of iron transfer to the permease.

Overall, for both of the anion-independent cFbpA and anion-dependent nFbpA, the permease is proposed to form productive interactions with holo conformations that are distinct from the apo conformations. For nFbpA, phosphate likely facilitates iron transport *in vivo* since the conformation of phosphate bound holo nFbpA is distinct from the apo conformation. Additional synergistic anions have the potential to facilitate iron transport in vivo if the holo complexes exhibit distinct conformations from apo nFbpA. As for anion-independent cFbpA, only the closed conformation of holo cFbpA is likely to form a productive interaction with the permease.

Chapter Five: Influence of synergistic anions on conformation of the ferric binding protein from *Bordetella pertussis*

5.1 Introduction

The potential role of bFbpA in iron uptake in *Bordetella pertussis* is unknown. Therefore, to elucidate the iron binding properties and mode of iron binding by the Class II bFbpA in iron transport, visible spectroscopy and x-ray crystallography was conducted. In-depth conformational analyses were also conducted in solution using SAXS. High affinity iron binding was observed utilizing carbonate, citrate and oxalate as synergistic anions. Carbonate, citrate and oxalate bound holo bFbpA complexes each produce distinct conformations that differ from that of apo bFbpA. A model for Class II FbpA iron transport is proposed where these holo complexes are candidates for initiating productive interactions with the permease. The predominant holo bFbpA complex likely reflects the composition and concentration of anions in the diverse periplasmic environment.

5.2 Results

5.2.1 Visible spectroscopic analyses of iron and anion binding

The addition of ferrous sulfate to apo bFbpA in the presence of ambient carbonate (bFbpA:Fe:carbonate) gives a stable absorbance maximum at 416 nm (Figure 5-1, panel A), which is indicative of iron oxidation to give a ferric-tyrosinate interaction (117). bFbpA treated with ferrous sulphate and oxalate (bFbpA:Fe:oxalate) yields an absorbance maximum at 438 nm whereas bFbpA treated with ferrous sulphate and citrate (bFbpA:Fe:citrate) gives an absorbance maximum at 428 nm (Figure 5-1, panel A). The

shifts in the absorbance maxima from 416 nm indicate that both anions are likely interacting directly with the bound iron. The anions acetate, glyoxylate, succinate, salicylate, lactate and pyrophosphate do not shift the absorbance maximum from 416 nm and are therefore likely not synergistic for iron binding to bFbpA (data not shown). All of these experiments were done in the presence of ambient carbonate and oxygen.

5.2.2 Estimation of high iron binding affinity by iron chelator competition experiments

To estimate iron affinity, competition experiments were conducted with the iron chelator pyrophosphate (Figure 5-1, panel B). Increasing concentrations of pyrophosphate decreases the visible absorbance of holo bFbpA (curves 1 to 4) and holo nFbpA (curve 5). Pyrophosphate addition to holo nFbpA results in a small blue shift in the visible absorbance as observed previously (153). Spectral blue shifts of absorbance peaks to a common wavelength have been observed for holo nFbpA bound with either phosphate or nitilotriacetate (NTA) following EDTA addition (41). For bFbpA:Fe:carbonate, a chelator:protein ratio of 41:1 reduces the initial absorbance reading by half (curve 1). The same reduction in initial absorbance reading is achieved using a chelator: protein ratio of 29:1 for holo nFbpA (curve 2), indicating that the iron binding constant of bFbpA:Fe:carbonate is within the same order of magnitude to that of nFbpA.

As for bFbpA:Fe:oxalate and bFbpA:Fe:citrate, the competition experiments were conducted in the presence of 3.6 mM oxalate and 1.3 mM citrate, as removal of these anions results in blue shifts to 416 nm. Following 1 mM pyrophosphate addition, blue

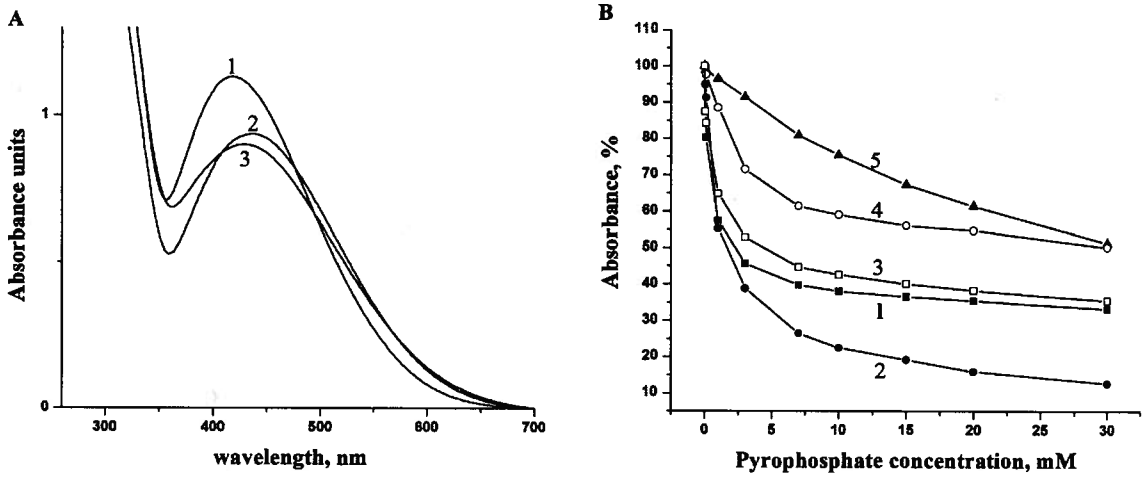

Figure 5-1 Iron binding properties of bFbpA:Fe:carbonate, bFbpA:Fe:oxalate, and bFbpA:Fe:citrate.

A, Absorbance spectra of bFbpA:Fe:carbonate (1), bFbpA:Fe:oxalate (3.6 mM oxalate) (2), and bFbpA:Fe:citrate (1.3 mM citrate) (3) in 200 mM NaCl, 20 mM Tris-HCl buffer, pH 7.0. The peak absorbance for bFbpA:Fe:carbonate, bFbpA:Fe:oxalate and bFbpA:Fe:citrate are 416 nm, 438 nm and 428 nm, respectively. B, Estimation of iron affinity of bFbpA by competition using sodium pyrophosphate. (1) bFbpA:Fe:carbonate, (2) holo nFbpA, (3) bFbpA:Fe:oxalate in buffer plus 3.6 mM oxalate, (4) bFbpA:Fe:citrate in buffer plus 1.3 mM citrate, and (5) bFbpA:Fe:carbonate in buffer plus 57 mM carbonate. Buffer contains 200 mM NaCl, 10 mM Tris-HCl, pH 7.4.

shifts of the absorbance peaks to 416 nm were also observed for the bFbpA:Fe:oxalate and bFbpA:Fe:citrate protein samples. In the presence of 3.6 mM oxalate, an increased chelator:protein ratio of 123:1 is needed (curve 3). For both of bFbpA:Fe:citrate in 1.3 mM citrate (curve 4) and bFbpA:Fe:carbonate in the presence of 1000 molar excess carbonate (57 mM, curve 5), a higher chelator:protein ratio of greater than 500:1 is required to reduce the initial absorbance reading by half. The effect of 57 mM carbonate on the affinity of bFbpA for iron indicates that carbonate is a synergistic anion for holo bFbpA. Carbonate has a similar role as a synergistic anion in iron binding by transferrin (14). Overall, the synergistic anions carbonate, oxalate and citrate increase iron affinity of bFbpA.

5.2.3 Overall structure of bFbpA

The bFbpA crystal structures consist of two globular domains linked by two anti-parallel β-strands containing a flexible hinge region (Figure 5-2). Residues 6 to 105 and 238 to 287 comprise the N-terminal domain whereas the C-terminal domain contains residues 106 to 237 and 288 to 323. Residues 228 to 232 form a flexible loop distant from the domain interface and are not modeled. Both domains are constructed from α-β-α units such that the core of the N-terminal domain is a six stranded β-sheet surrounded by six α-helices and the C-terminal domain contains a central four stranded β-sheet surrounded by eight α-helices. MAD data collection and refinement statistics for SeMet labelled apo bFbpA are shown in Table 5-1. Monochromatic data collection and refinement statistics for apobFbpA, bFbpA:Fe:oxalate and bFbpA:Fe:carbonate are shown in Table 5-2.

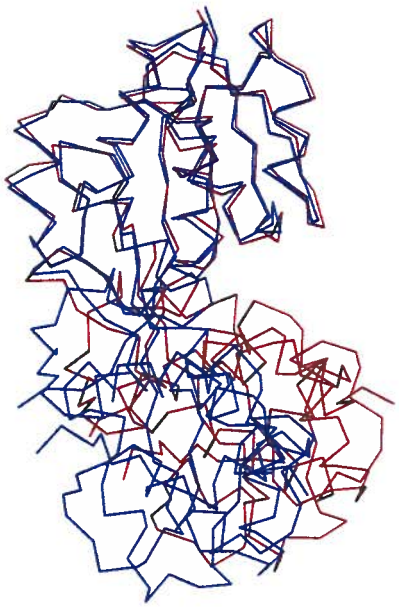

Figure 5-2 Least-squares superimposition of the N-terminal domains of apo bFbpA and bFbpA:Fe.

Apo bFbpA is represented by a blue α-carbon trace. bFbpA:Fe:carbonate is represented by a red α-carbon trace. Figures 5-2 and 5-3 were made using Molscript (87) and Raster3D (99).

Table 5-1 Multiwavelength anomalous dispersion (MAD) data collection statistics for SeMet labelled apo bFbpA.

Wavelength (Å)	0.978743	0.904965	0.979029
Resolution range (Å)	50.0 – 1.90	50.0 – 1.90	50.0 – 1.90
	(1.97 – 1.90)	(1.97 – 1.90)	(1.97 – 1.90)
R_{merge}	0.051 (0.213)	0.045 (0.229)	0.045 (0.294)
{I}/{σI}	12.2 (3.3)	14.2 (3.1)	15.37 (2.8)
Completeness (%)	93.5 (78.7)	93.4 (90.5)	92.8 (77.1)
Unique reflections	24456	24519	24585
Redundancy	10.9	11.3	10.9
No. of selenium sites	3/4		

Note: Values reported in parentheses refer to the highest resolution shell.

Table 5-2 Data collection and refinement statistics.

Crystal	Apo bFbpA	bFbpA:Fe:oxalate	bFbpA:Fe:carbonate
Wavelength (Å)	1.08000	0.97944	0.97944
Resolution (Å)	30.0 – 1.4	50.0 – 1.5	48.0 – 2.4
	(1.42 -1.40)	(1.54 – 1.49)	(2.49– 2.40)
R_{merge}	0.034 (0.270)	0.043 (0.184)	0.069 (0.276)
{I}/{σI}	36.9 (4.3)	13.2 (4.3)	26.9 (9.9)
Completeness (%)	92.2 (71.9)	91.6 (86.1)	95.6 (96.7)
Unique reflections	64747	101476	56375
Redundancy	12.5	2.3	5.3
R_{work}	0.166	0.184	0.175
R_{free}	0.188	0.208	0.242
r.m.s.d. bonds (Å)	0.01	0.01	0.01
Overall B factor ($Å^2$)	18.1	13.0	10.9
B-factor of iron ($Å^2$)	N/A	8.1	5.4
B-factor of waters ($Å^2$)	27.8	21.0	13.5
B-factor of anion(s) ($Å^2$)	N/A	8.8, 16.0	8.3
Wilson B-factor ($Å^2$)	15.7	12.7	21.4
Coordinate error[a] (Å)	0.03	0.04	0.18
PDB ID	1Y9U	2OWS	2OWT

Note: Values reported in parentheses refer to the highest resolution shell.

[a] Coordinate error derived from maximum likelihood refinement.

5.2.4 Apo bFbpA crystal structure

The two domains of the apo bFbpA crystal structure (PDB ID 1Y9U) interact only at the hinge region (Figure 5-2, blue). Near the hinge region is a cluster of tyrosine residues (Tyr143, Tyr199 and Tyr200) which are positioned at the N-termini of two α-helices of the C-terminal domain (Figures 5-3, panel A and 5-4, panel A). Minor alternate conformations are observed for the side chains of Tyr143 and Tyr199. These three tyrosines are conserved iron site residues (153) and thus this cluster is poised for iron binding in apo bFbpA. No potential synergistic anions are identified within the iron binding site (Figures 5-3, panel A and 5-4, panel A).

The residues that make up the domain interface (formed in the closed conformation) are involved in key hydrogen bond networks in the apo protein. Within the N-terminal domain, Arg14 is involved in a hydrogen bond network with Glu276 and Arg105 (Figure 5-3, panel A). Connecting the N- and C-terminal domains is a charge network involving Asn238, Asp63 and Arg309 (Figure 5-3, panel A). The apo bFbpA structure displays good stereochemistry, as shown by a Ramachandran plot, with 92.6 % of the residues residing in the most favored regions and 7.0 % of residues in the allowed regions (91). Asp63 is the only residue in the disallowed region which is located within a loop and forms an interdomain salt bridge with Arg309.

5.2.5 bFbpA:Fe:oxalate crystal structure

The crystal of bFbpA:Fe:oxalate was isomorphous with that of apo bFbpA. Least-squares superimposition of the α-carbons of the apo and bFbpA:Fe:oxalate (PDB ID 2OWS) structures show that both structures are in the same conformation (0.22 Å

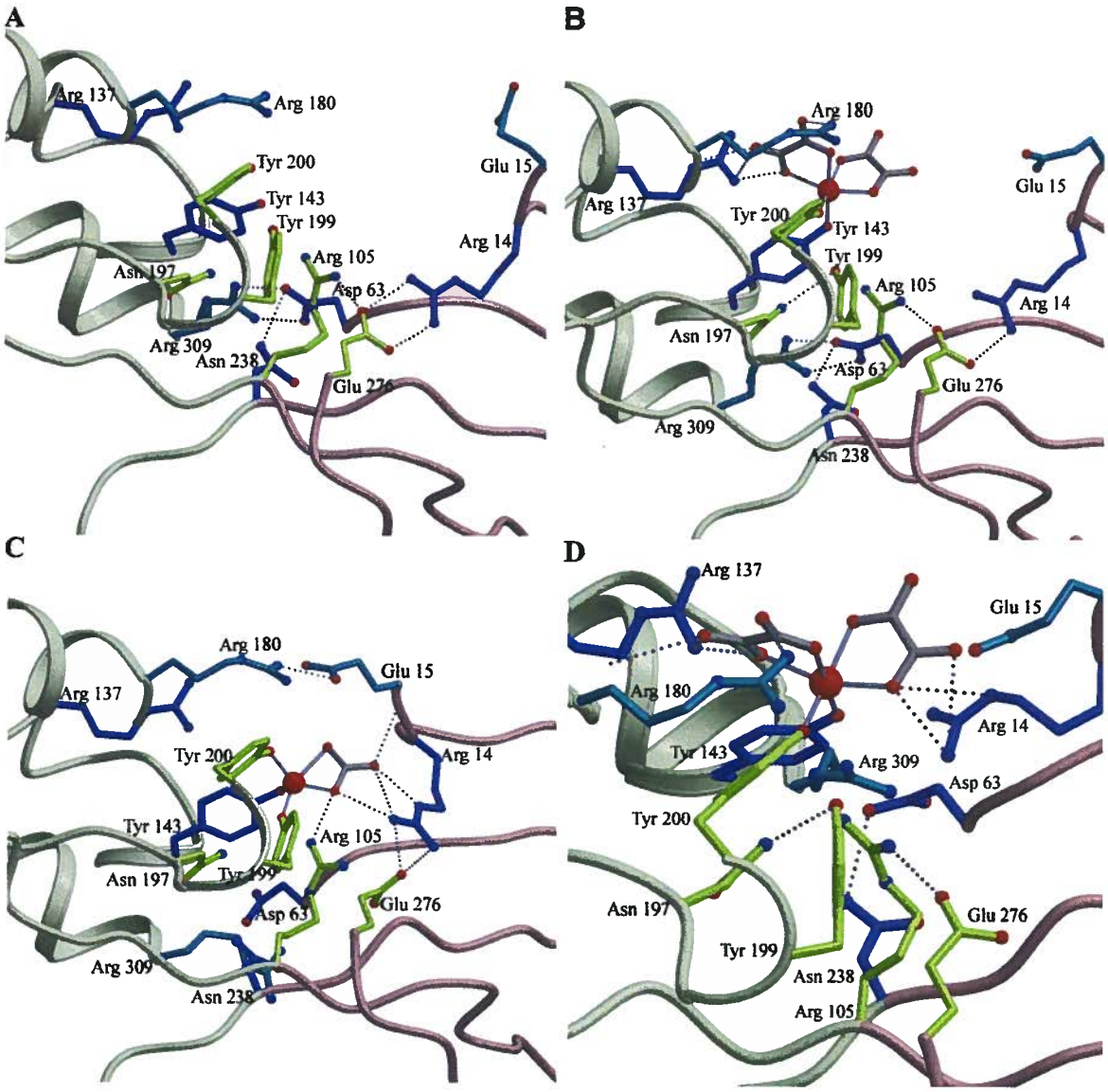

Figure 5-3 Comparison of the iron binding sites of the crystal structures of A, apo bFbpA B, bFbpA:Fe:oxalate and C, bFbpA:Fe:carbonate and of D, a model based on SAXS data of a bFbpA:Fe:oxalate.

The backbones of the N- and C-terminal domains are colored in light pink and khaki colours, respectively. The yellow residues are conserved among most FbpA proteins. Dark purple residues are conserved among Class II, III and IV FbpA. Cyan residues are conserved within the Class II cluster containing bFbpA. Synergistic anions are grey and iron is depicted as a red sphere. The nitrogen and oxygen atoms of the residue side chains are coloured blue and red, respectively. Ligand and H-bonds are indicated by solid and dotted lines, respectively.

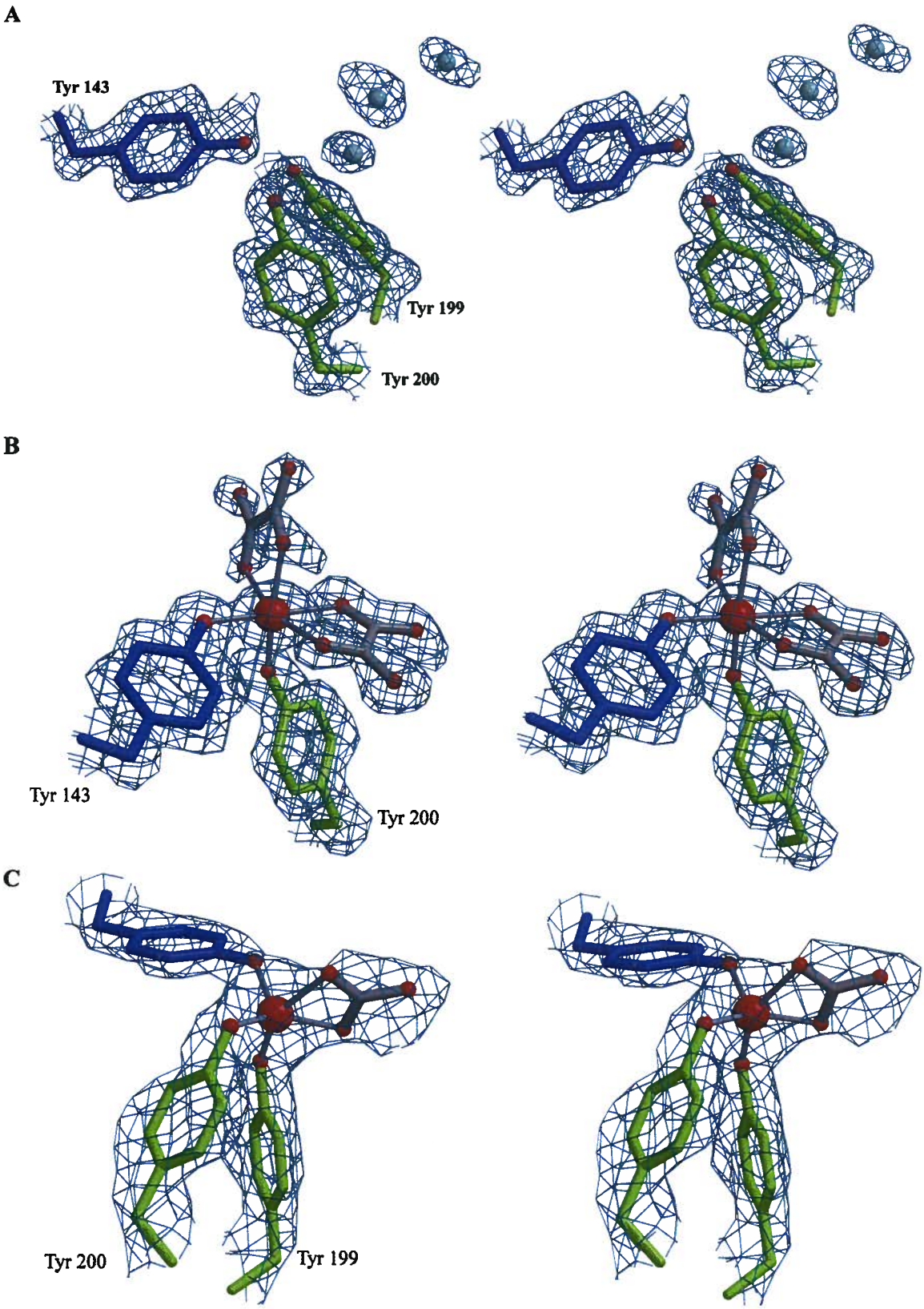
A
Tyr 143
Tyr 199
Tyr 200
B
Tyr 143
Tyr 200
C
Tyr 200
Tyr 199

Figure 5-4 Stereoviews of the iron binding sites of A, apo bFbpA B, bFbpA:Fe:oxalate and C, bFbpA:Fe:carbonate.

F_o-F_c omit electron density is contoured at 2.5 σ. Water molecules are represented by blue spheres. All other atoms are as represented in Figure 5-3. The iron site residues are labeled. This figure was made using Molscript (87) with changes by R. Esnouf and Raster3D (99).

Table 5-3 Geometry of the bFbpA:Fe:oxalate iron site.

Iron ligand angles	Degrees
Tyr200OH -FE- Tyr143OH	92.7
Tyr200OH-FE-Oxl325O1	91.1
Tyr200OH -FE- Oxl325O2	87.4
Tyr200OH -FE- Oxl326O2	102.7
Oxl326O1-FE- Oxl326O2	75.8
Oxl326O1-FE- Tyr143OH	93.3
Oxl326O1-FE- Oxl325O1	88.8
Oxl326O1-FE- Oxl325O2	86.7
Oxl325O1-FE- Oxl325O2	74.7
Oxl325O1-FE- Tyr143OH	106.0
Tyr143OH -FE- Oxl326O2	89.9
Oxl326O2-FE- Oxl325O2	89.5

r.m.s.d.) with little interaction between the two domains. Iron binding is six coordinate in a slightly distorted octahedral geometry (Table 5-3) involving two of the conserved Tyr residues (Tyr143 and Tyr200) from the C-terminal domain and bidentate binding by two oxalate anions (Figures 5-3, panel B and 5-4, panel B). The iron and oxalate molecules are modeled in at 70% occupancy. The OH atoms of the two coordinating Tyr residues are 2.1 and 1.9 Å from the iron and have comparable crystallographic B-factors (9.6 $Å^2$ and 10.7 $Å^2$) to that of the iron atom (8.1 $Å^2$). The oxygens of the oxalate molecules coordinate iron at bond lengths ranging from 2.1 to 2.2 Å and exhibit B-factors from 9.1 to 13.7 $Å^2$. Compared with the iron site residues of apo bFbpA, the OH atoms of Tyr199 and Tyr200 are shifted by 0.4 and 0.5 Å, respectively, whereas Tyr143 is in the same position (within error) as observed in the alternative conformation in the apo bFbpA structure.

Further comparison with the apo bFbpA structure shows that the interdomain hydrogen bonding network involving Arg309, Asp63 and Asn238 is fully conserved in the bFbpA:Fe:oxalate structure whereas the network involving Arg14, Glu276 and Arg105 is only partly conserved. Arg14 is less well ordered and the side-chain is modeled in three alternate conformations. Additional hydrogen bonding interactions are formed between one of the oxalate anions and Arg137 and Arg180. This oxalate molecule is the more ordered of the two and refined with lower B-factors. As well, a new hydrogen bond is observed between Asn197 and the iron site residue Tyr199 (Figure 5-3, panel B). Overall, the bFbpA:Fe:oxalate structure displays good stereochemistry, as shown by a Ramachandran plot, with 91.9 % of the residues residing in the most favored regions and

7.7 % of residues in the allowed regions (91). As observed for the apo bFbpA structure, Asp63 is the sole residue in the disallowed region of a Ramachandran plot (91).

5.2.6 bFbpA:Fe:carbonate crystal structure

The bFbpA:Fe:carbonate crystal was not isomorphous with either of the apo bFbpA or bFbpA:Fe:oxalate crystals. bFbpA:Fe:carbonate crystallized in the closed conformation (PDB ID 2OWT) (Figure 5-2, red) with the iron binding site located at an expanded domain interface (Figures 5-3, panel C and 5-4, panel C). The hinge region (residues 104 and 239) allows for an interdomain rotation from the conformation observed in the crystal structures of apo bFbpA and bFbpA:Fe:oxalate to this closed conformation.

The iron is coordinated in a distorted octahedral geometry with one absent site (Table 5-4) by the three conserved C- terminal domain Tyr residues (Tyr143, Tyr199 and Tyr200) and bidentate binding of a carbonate anion. The N-terminal domain interacts indirectly with the iron atom through hydrogen bond interactions between the carbonate anion and two arginine residues (Arg14 and Arg105). The OH atoms of the three coordinating Tyr residues are between 1.9 to 2.0 Å from the iron and exhibit B-factors similar to that of the iron atom (5.4 $Å^2$). The coordinating carbonate oxygens are 1.9 and 2.3 Å from the iron and have higher B-factors of 8.8 and 8.0 $Å^2$, respectively. Compared with apo bFbpA, the OH atoms of Tyr199 and Tyr200 are shifted by 0.5 and 0.7 Å, respectively, to occupy similar positions as observed in the bFbpA:Fe:oxalate structure, whereas the phenolic oxygen atom of Tyr143 is shifted by 0.9 Å to occupy a spatially unique position.

Table 5-4 Geometry of the bFbpA:Fe:carbonate iron site.

Iron ligand angles	Degrees
Tyr143OH-FE-Tyr199OH	98.7
Tyr143OH- FE-Tyr200OH	110.7
Tyr143OH- FE-CO_3O1	97.6
Tyr143OH- FE-CO_3O2	115.7
Tyr199OH- FE-Tyr200OH	106.7
Tyr199OH- FE-CO_3O2	92.1
Tyr200OH - FE-CO_3O1	86.8
CO_3O1- FE-CO_3O2	61.9

The hydrogen bond network involving Arg14, Arg105 and Glu276 in apo FbpA is disrupted in bFbpA:Fe:carbonate to allow the arginine residues to hydrogen bond to the carbonate anion. The interdomain network involving Asn238, Asp63 and Arg309, present in both apo bFbpA and bFbpA:Fe:oxalate, is abolished. Instead, a new electrostatic interaction is observed connecting the domains and is comprised of Glu15 from the N-terminal domain and Arg180 from the C-terminal domain (Figure 5-3, panel C). Notably, the new conformation of Asp63 is in the allowed region of the Ramachandran plot and no residues are observed in the disallowed region. Overall, the bFbpA:Fe:carbonate structure displays good stereochemistry as shown by a Ramachandran plot, with 92.3 % of the residues residing in the most favored regions and the remaining 7.7 % of residues in the allowed regions (91).

Least-squares superimposition of the N- and the C-terminal domains of apo bFbpA onto the respective domains of bFbpA:Fe:carbonate yields r.m.s. deviations on α-carbons of 0.98 and 0.51 Å, respectively. Within the C-terminal domain, shifts are observed primarily due to crystal contacts with other symmetry related molecules. Within the N-terminal domain of bFbpA:Fe:carbonate, significant intra-domain rearrangements are observed upon establishment of the closed conformation. These include a shift towards the iron site of an average 1.2 Å by the Cα atoms in an α-helix, formed by residues 15 to 31. As well, there is a conformational rearrangement of residues 270 to 276 (2.6 Å r.m.s.d on Cα atoms) which are located near the interdomain surface. In the apo bFbpA structure, residues 264 to 273 form an α-helix that is terminated with a turn comprised of residues 272 to 275. Within this turn, Asn274 forms an interdomain

interaction with His203. Also, within this region, additional intra-domain hydrogen bonding contacts are observed between Tyr270 and Ser240 (within the central β-sheet) as well as between Asp272 and Glu286. Upon forming the closed conformation, this region is restructured to avoid steric clashes between Asn274 with the phenyl group of the iron site residue Tyr199 and between Tyr275 with the carbonyl group of Gly202. In total, this region shifts away from the iron site and the α-helix is shortened by one amino acid, extending the turn to include residues 271 to 275.

5.2.7 SAXS analyses of bFbpA

SAXS data were collected at a pH (pH 7.0) similar to that of the periplasmic environment. For all of the bFbpA protein samples, slight inflections of the scattering curves in the very low angle region (Figure 5-5) are observed due to X-ray leakage around the beamstop and scattering from some aggregated protein. The radii of gyration were calculated over the momentum transfer range of 0.404 to 0.751 nm^{-1} (Table 5-5, Figure 5-6). Non-logarithmic difference curves show a close match between apo bFbpA and bFbpA:Fe:carbonate (Figure 5-5, panel A) and a clear systematic difference between bFbpA:Fe:oxalate (Figure 5-5, panel B) and bFbpA:Fe:citrate (Figure 5-5, panel C) from apo bFbpA. The overall shapes of the curves suggests that apo bFbpA and bFbpA:Fe:carbonate (Figure 5-5, panel A) are more extended whereas both bFbpA:Fe:oxalate (Figure 5-5, panel B) and bFbpA:Fe:citrate (Figure 5-5, panel C) are more globular and compact. Crossovers of the apo bFbpA SAXS curve with the bFbpA:Fe:oxalate (Figure 5-5, panel B) and bFbpA:Fe:citrate (Figure 5-5, panel C) curves are observed at approximately a momentum transfer of 1.4 nm^{-1}.

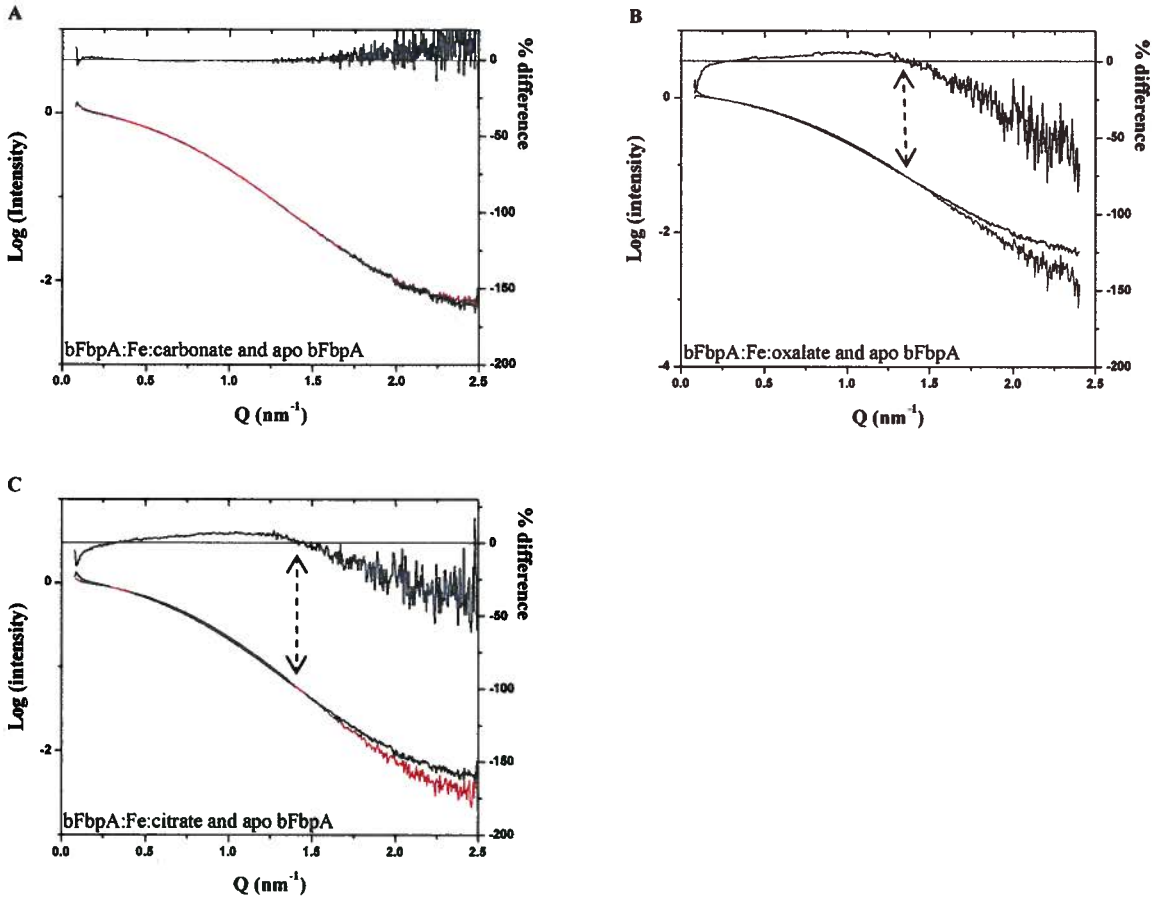

Figure 5-5 Experimental SAXS curves for bFbpA.

A, The SAXS curve for bFbpA:Fe:carbonate is similar to apo bFbpA showing that these protein samples adopt similar solution conformations. SAXS curves for B, bFbpA:Fe:oxalate and C, bFbpA:Fe:citrate show crossovers (indicated by dotted arrows) with the apo bFbpA curve at 1.4 nm^{-1}, illustrating large conformational changes. In each panel, the SAXS curves for the apo and iron loaded protein samples are in black and red, respectively. The scattering curves are represented as a plot of momentum transfer Q (a function of the scattering angle) versus the log of the scattering intensity. Differences between the holo and respective apo protein are plotted as a percentage of the apo protein signal.

Table 5-5 Radii of gyration for the SAXS protein samples.

Protein	Radius of gyration (Å)
Apo bFbpA	21.76 ± 0.01
bFbpA:Fe:carbonate	22.05 ± 0.01
bFbpA:Fe:oxalate	21.48 ± 0.01
bFbpA:Fe:citrate	21.25 ± 0.02

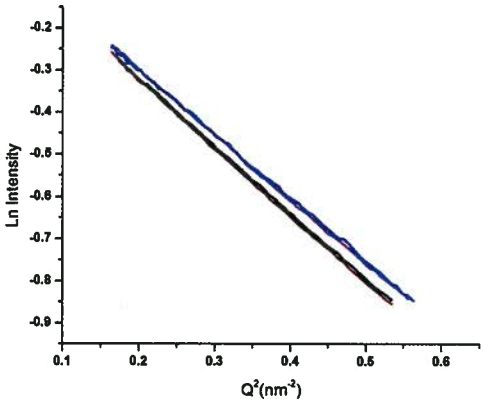

Figure 5-6. Guinier plots of apo bFbpA, bFbpA:Fe:carbonate, bFbpA:Fe:oxalate and bFbpA:Fe:citrate.

The Guinier plots of apo bFbpA (black), bFbpA:Fe:carbonate (red), bFbpA:Fe:oxalate (pink) and bFbpA:Fe:citrate (blue). The radius of gyration (Rg) was obtained from Crysol and was derived from the slopes of the Guinier plots.

For both apo bFbpA and bFbpA:Fe:carbonate, open models with interdomain angles greater than 50° can adequately model the SAXS data. Since the SAXS data for apo bFbpA and bFbpA:Fe:carbonate are almost identical, representative curves of the fit of the models to the SAXS data of apo bFbpA are discussed (Figure 5-7, panel A). For comparison, the fit of models to the SAXS data of bFbpA:Fe:carbonate are shown (Figure 5-7, panel C). The *in silico* open model with an interdomain angle of 56° provides a better fit to the apo bFbpA SAXS data (χ^2=2.1, Figure 5-7, panel A blue) than the ajar crystal structure with an interdomain angle of 25° (χ^2= 3.8, Figure 5-7, panel A purple) or the closed crystal structure (χ^2= 8.3, Figure 5-7, panel A red). As for bFbpA:Fe:citrate and bFbpA:Fe:oxalate, an *in silico* ajar model exhibiting an interdomain angle of 9° provides a good fit to the SAXS data for bFbpA:Fe:citrate (χ^2=1.6, Figure 5-7, panel B blue) and a reasonable fit for the bFbpA:Fe:oxalate SAXS data (χ^2=2.7, Figure 5-7, panel D blue). The fits of the ajar (χ^2=2.6, Figure 5-7, panel B purple) and closed (χ^2=3.0, Figure 5-7, panel B red) crystal structures to the bFbpA:Fe:citrate SAXS data are shown (for bFbpA:Fe:oxalate, see Figure 5-7, panel D).

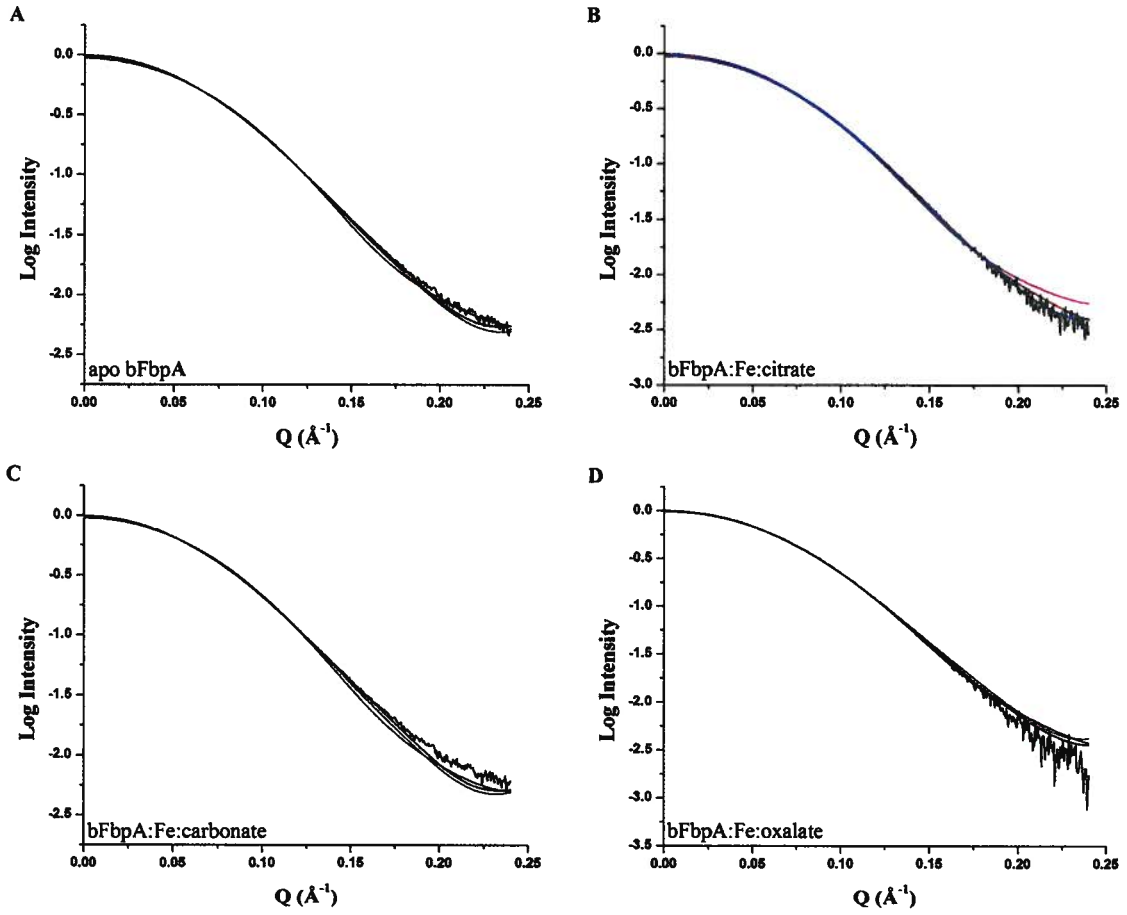

Figure 5-7 Comparison of the theoretical scattering from crystal structures and *in silico* models (colored lines) with SAXS data (black lines) from bFbpA using Crysol (146).

In all panels, the red curve refers to the closed crystal structure model, the purple curve refers to the ajar crystal structure model and the blue curve refers to the *in silico* model. The experimental SAXS curves are black. Interdomain angles for open and ajar models are given in parentheses. A, For the apo bFbpA SAXS data, fits of an *in silico* open model (56°), ajar crystal structure model (25°) and closed crystal structure model gave χ^2 values of 2.1, 3.8 and 8.3, respectively. B, For the bFbpA:Fe:citrate SAXS data, fits of an *in silico* ajar model (9°), ajar crystal structure model (25°) and closed crystal structure model gave χ^2 values of 1.6, 2.6 and 3.0, respectively. C, For the bFbpA:Fe:carbonate SAXS data, fits of an *in silico* open model (56°), ajar crystal structure model (25°) and closed crystal structure model gave χ^2 values of 4.1, 7.3 and 12.4, respectively. D, For the bFbpA:Fe:oxalate SAXS data, fits of an *in silico* ajar model (9°), ajar crystal structure model (25°) and closed crystal structure model gave χ^2 of 2.7, 3.2 and 3.9, respectively.

5.3 Discussion

5.3.1 Anion-dependent bFbpA undergoes large hinge motion in solution

Here, we show that the Class II FbpA from *Bordetella pertussis* (bFbpA) can use a variety of synergistic anions (carbonate, oxalate and citrate) for iron binding. All of these holo complexes yield distinct conformations from apo bFbpA. The closed conformation crystal structure is observed for the carbonate-bound holo bFbpA. bFbpA shows the classic crossing over of the apo and holo (bFbpA:Fe:oxalate and bFbpA:Fe:citrate) SAXS curves that is typically seen in periplasmic binding proteins which undergo large interdomain movement (138). Modeling of SAXS data show that apo bFbpA exhibits a large hinge angle (greater than 50°) compared with the closed conformation crystal structure whereas holo bFbpA treated with either oxalate or citrate is best modeled by a model exhibiting a 9° hinge angle.

Compared with the bFbpA:Fe:carbonate crystal structure, the greater hinge angle observed for the oxalate and citrate bound holo bFbpA proteins in solution likely reflects the binding of anions (citrate or oxalate) larger than carbonate in the iron site. For the bFbpA:Fe:oxalate solution model, this conformation may be stabilized by the N-terminal domain residue Arg14 which, in one of the three conformations present in the crystal structure, is available to hydrogen bond to oxalate (Figure 3, panel D). Within the respiratory tract, these anions may complex iron and provide alternate iron sources for bFbpA. Also, oxalate may be present under disease conditions resulting from infection with *Aspergillus niger* (51) or exposure to asbestos (52).

5.3.2 Conformational flexibility of bFbpA

Striking differences are observed between the conformations in crystal and in solution by SAXS. For holo bFbpA in the presence of ambient carbonate, a closed conformation is observed in crystal but this complex is primarily open in solution. This conformational difference suggests a modest energy barrier between the closed and open conformations. Alternatively, carbonate may not be bound stoichiometrically in solution under ambient carbonate concentrations at pH 7.0. Another factor is that the bFbpA:Fe:carbonate crystals were grown at pH 9.0 which likely favours ferric and carbonate binding. Furthermore, the crystal structures of apo bFbpA and bFbpA:Fe:oxalate share an ajar interdomain angle of 25° in crystal but in solution, apo bFbpA exhibits primarily an open conformation whereas bFbpA:Fe:oxalate and bFbpA:Fe:citrate are almost closed (9°). These differences are not uncommon in proteins that contain flexible interdomain hinges. For example, a closed unliganded form of the glucose/galactose periplasmic binding protein was crystallized, whereas in solution the average conformation is open (138). Furthermore, the congruence in interdomain angles observed in apo bFbpA and bFbpA:Fe:oxalate, nFbpA (24° for PDB ID 1R1N), hFbpA (20° for PDB ID 1D9V) and mFbpA (27° for PDB ID 1SI1) suggests that these crystal conformations may represent metastable states, albeit a minority species in solution, that favor crystal nucleation and growth.

5.3.3 Role of anion in conformation

Overall, these results show that holo bFbpA undergoes large hinge motion that is dependent on the synergistic anion. The SAXS data of holo bFbpA in the presence of

ambient carbonate suggests that iron alone is insufficient for increasing the stability of the closed conformation of bFbpA (Figures 5-5, panel A and 5-7, panel C). The synergistic anion likely has a crucial role in affecting the conformation of bFbpA and stabilizing the conformations of holo bFbpA species distinct from apo bFbpA. Similarly for the other Class II mFbpA, carbonate is proposed to facilitate domain closure of mFbpA (141). This proposal was based on the observation of a closed conformation crystal structure of formate bound apo mFbpA, showing formate bound in the carbonate binding site.

5.3.4 Iron transport model for Class II bFbpA

Conformational analyses of the Class II ferric binding protein system from *Bordetella pertussis* suggests that this system may function analogous to a histidine uptake system. This system is comprised of a periplasmic binding protein HisJ and the respective permease $HisQMP_2$. Similar to bFbpA, HisJ can bind a variety of ligands (L-His, L-Arg, L-Lys), all of which have distinct conformations in solution, as elucidated using conformational specific antibodies and decay of anisotropy of florescence (88, 163). Translocation of these different ligands across the permease has been demonstrated *in vitro* (94). For HisJ, the efficiency of transport is independent of the ligand binding affinity. Instead, the spatial relationship of the domains i.e. conformation dictates the efficiency of signal induction and subsequent ligand translocation across the permease. Following interaction with the permease, each specific HisJ ligand complex stimulates a different level of ATPase induction, which does not necessarily result in different levels of transport.

Using the histidine uptake system as a model for iron transport by bFbpA, iron translocation across the inner membrane is likely to be largely dependent on the conformation of the holo bFbpA complexes. Since the crystal conformation of bFbpA:Fe:carbonate, and the solution conformations of bFbpA:Fe:oxalate and bFbpA:Fe:citrate are distinct from that of apo bFbpA, each of these protein complexes may form productive interactions with the permease. These results suggest that bFbpA requires an anion for efficient iron transport *in vivo*. The visible spectroscopic studies suggest that the predominant holo bFbpA complex *in vivo* would be dependent on the anion composition and concentration in the periplasm. The periplasmic anion composition is expected to be diverse and reflect the external host environment (64). Hence, the holo bFbpA complexes are likely important for the efficient sequestration of available iron species in the periplasm.

Furthermore, under conditions that favor carbonate as the synergistic anion, citrate and oxalate may be involved in facilitating iron binding. Since, unlike carbonate, citrate and oxalate are also iron chelators, following iron entry into the periplasm, iron may be chelated by citrate and oxalate. bFbpA may then bind these iron sources, prior to synergistic anion exchange with carbonate. The oxalate-bound holo bFbpA crystal structure may therefore yield insights into the mechanism of iron loading *in vivo*. Compared with the carbonate-bound holo bFbpA, the bound iron is more surface exposed in the oxalate bound structure. As well, of the two absolutely conserved tyrosine ligands in FbpA members, only one is used to coordinate the iron. The oxalate-bound holo bFbpA structure suggests that iron loading of the tyrosines may be step-wise. Step-wise

ligation of iron by the tyrosines in the interdomain iron binding site has also been proposed for duck ovotransferrin (90). The closed conformation carbonate-bound holo bFbpA may then form a productive interaction with the permease.

Chapter Six: Overview and future directions

FbpA is the essential periplasmic component of a PBP-dependent ABC transport system. FbpA proteins are members of family 2 PBPs consisting of two domains connected by a pair of anti-parallel β strands containing a hinge region with the substrate binding site located at the domain interface (161). Due to interdomain hinge motion, FbpA proteins can exhibit varied conformations. In the substrate-bound closed conformation, the complete iron-binding site is observed. By homology with other PBP - dependent ABC transport systems, the closed conformation of FbpA likely facilitates productive interaction with the inner membrane permease (37, 68, 94, 95, 166). Although FbpA proteins share similar characteristics including tertiary structure and high affinity iron binding, FbpA proteins also exhibit significant differences in iron coordination and conformational behaviour which are likely to impact iron transport mechanisms (Table 6).

Table 6-1 Comparison of the iron binding characteristics of nFbpA, bFbpA and cFbpA.

FbpA Class	Representative Member	Closed conformation iron site ligands	Synergistic Anion(s)[a]	Hinge Motion[b]
I	nFbpA	Hexacoordinate: His, Glu, 2 Tyr residues, water and phosphate (PDB ID 1D9Y)	Phosphate	Phosphate bound holo nFbpA: Large
II	bFbpA	Pentacoordinate: 3 Tyr residues and carbonate (bidentate)	Carbonate, citrate, oxalate	Citrate or oxalate bound holo bFbpA: Large
III	cFbpA	Pentacoordinate: His and 4 Tyr residues	N/A (anion-independent)	Small

Note: All information reported in this table, except for the nFbpA crystal structure, resulted from work in this thesis. [a] The anions listed refer to anions that influence the holo FbpA conformation in crystal or solution. [b] The hinge motion refers to the conformational change between the holo and the apo protein in solution.

6.1 Classification of FbpA proteins

FbpA proteins exhibit significant variation in iron binding and utilization of a synergistic anion. A classification scheme was therefore sought to meaningfully group FbpA proteins and allow for comparisons within and across groups. Phylogenetic analyses of FbpA proteins allowed for the assignment of FbpA proteins into six classes based on conservation of iron site ligands and clustering (Figure 3-5). Class I FbpA members include the structurally characterized nFbpA and hFbpA in one cluster and YfuA in the other cluster. The closed conformation structures of holo nFbpA and holo hFbpA show iron bound using N-terminal domain His and Glu residues, two C-terminal domain Tyr, water and a phosphate synergistic anion (Figure 3-1, panel C). The closed conformation crystal structure of YfuA also shows iron coordinated similarly to nFbpA and hFbpA; however, instead of phosphate, an Asp is used to coordinate iron (Figure 1-4, panel B). Class II FbpA members include the structurally characterized bFbpA and mFbpA in separate clusters. The closed conformation crystal structures of these proteins show iron coordination using three C-terminal domain tyrosine residues with the N-terminal domain binding iron indirectly through a synergistic carbonate anion (Figures 3-1, panel D and 5-3, panel C). The structurally characterized members of Class III include cFbpA in one cluster and FutA1 and FutA2 in the other cluster. The closed conformation crystal structures show anion-indepenent iron binding using a histidine and a tyrosine from the N-terminal domain, and three C-terminal domain tyrosine residues (Figures 3-1, panel B and 1-4, panel C). Classes IV through VI do not contain any structurally characterized FbpAs. However, as a result of the classification scheme, each of these

classes is predicted to coordinate iron using a novel set of iron site ligands including the conserved C-terminal domain Tyr ligands.

6.2 Conformational differences across FbpA Classes

SAXS analyses showed that cFbpA, bFbpA and nFbpA exhibit differences in conformational behaviour in solution. Firstly, conformational differences were observed between anion-dependent and anion-independent FbpA proteins. The anion-dependent bFbpA and nFbpA undergo large hinge motion whereas the anion-independent cFbpA undergoes small hinge motion (Figure 4-7). These results support a role for the synergistic anion in bFbpA and nFbpA in facilitating iron binding by stabilizing an intermediate conformation. Previously, phosphate was proposed to enhance iron binding by nFbpA by stabilizing a specific protein tertiary structure (48). In addition, a conformational role of the anion was proposed for the Class II mFbpA based on the closed conformation crystal structure of the formate bound apo mFbpA (141).

Furthermore, the SAXS analyses showed that the anion-dependent bFbpA and nFbpA crystal structures provide poor overall representations of the conformations present in solution. Due to the poor fit of the crystal structures to the SAXS data, these results suggest that the anion-dependent holo FbpA proteins are not locked into the respective crystal structure closed conformations but are able to sample other conformations in solution. The ability to sample a range of conformations may facilitate the exchange of the bound anions with the anions in solution, as has been proposed for nFbpA (20).

The Class II holo bFbpA also exhibits varied conformations (distinct from apo conformations) when bound with different synergistic anions. The closed conformation crystal structure is observed for bFbpA:Fe:carbonate (Figure 5-3, panel C). Furthermore, in solution, oxalate (Figure 5-7, panel D) and citrate bound holo bFbpA (Figure 5-7, panel B) exhibit a hinge motion of approximately 9° compared with bFbpA:Fe:carbonate. In addition, the SAXS data of holo bFbpA collected at pH 7.0 in the presence of ambient carbonate suggests that iron alone is insufficient for the stabilization of the closed conformation (Figures 5-5, panel A and 5-7, panel C).

Overall, the differences in conformational behaviour between cFbpA, bFbpA and nFbpA suggest mechanistic differences in the initiation of iron translocation across the inner membrane. For cFbpA, the permease is proposed to form a productive interaction with only the closed conformation of anion-independent holo cFbpA. As for holo nFbpA and bFbpA, only the synergistic anions that effect holo FbpA conformations distinct from apo FbpA are proposed to have a role in promoting productive interactions with the inner membrane permease. Additionally for bFbpA, the synergistic anions may be required for efficient iron transport due to the inability of iron alone to stabilize the closed conformation.

6.3 FbpA mediated iron acquisition within bacteria

A role for cFbpA in iron transport in *C. jejuni* 81-176 was demonstrated by observing impaired growth of a Δ*cfbpA* strain under iron limited conditions compared to WT (Figure 4-3). Furthermore, *cfbpA* is transcribed in an operon with ABC transporter

genes (Figure 4-1), supporting iron uptake by a cFbpA-dependent ABC transporter system. Currently, the iron source for FbpA in *C. jejuni* 81-176 is unknown.

In general, the iron sources for most of the FbpABC transport systems are poorly characterized. The only FbpABC transport systems for which iron sources have been identified are from the human pathogens *H. influenzae*, *N. gonorrhoeae*, and *C. jejuni* NCTC 11168 (36, 78, 103). Furthermore, transferrin and lactoferrin are the only identified iron sources. The iron sources for FbpABC transport systems are likely underestimated especially considering that FbpA homologues are present in diverse prokaryotes including proteobacteria, cyanobacteria, Gram-positive bacteria, and archaea (Figure 3-5).

6.4 Future directions

This thesis suggests that the synergistic anion facilitates an intermediate conformation of bFbpA and nFbpA for iron binding. Future work into FbpA mediated iron transport can examine if the synergistic anion alone can produce an anion-dependent conformation of the apo protein. Observance of an anion-dependent conformation of apo FbpA would support a conformational role for the anion in facilitating iron binding. To elucidate the conformational effects of the synergistic anions in facilitating iron binding by bFbpA, SAXS experiments can be conducted for apo bFbpA in the presence of saturating concentrations of carbonate, citrate and oxalate. Similarly for nFbpA, SAXS experiments can be conducted for apo nFbpA in the presence of phosphate. For comparison to the anion-independent cFbpA, SAXS analyses of apo cFbpA can also be conducted in the presence of oxalate. Presumably, oxalate facilitates ferric iron binding

by cFbpA through chelating and solubilising the ferric iron. The SAXS experiments can elucidate if oxalate also has a conformational role in facilitating iron binding.

Another area for future work involves elucidating the mechanism of interaction between FbpA and the permease. Identification of residues from both domains of FbpA that interact with the permease would strongly suggest that conformation is important for initiating productive interactions with the permease. Co-crystallization of FbpA and the ABC transporter could be useful in identifying important interacting residues between FbpA and the permease. Similar co-crystallization experiments of MBP and BtuF with the respective permeases were successful in identifying the interacting residues of the PBPs with the respective permeases (19, 69, 111).

To further elucidate the function of these residues, site directed mutagenesis can be used to mutate these residues allowing for characterization of the mutated FbpA proteins. FbpA mutants may then be constructed in the respective bacteria and characterized. Impaired iron uptake and growth under iron limited conditions in a bioassay would support an important role for these residues in iron transport.

This thesis also explores the role of cFbpA in iron transport. In elucidating iron uptake in *C. jejuni*, strain considerations are important since variation is observed in the iron uptake system repertoire among the different strains (107). For all sequenced *C. jejuni* strains, FbpABC transport systems are identified. This thesis shows a functional role for cFbpA in iron transport in *C. jejuni* 81-176 under iron limited conditions. Additional studies in another *C. jejuni* strain NCTC 11168 have also shown that the permease component cFbpB facilitates iron acquisition supporting a functional link

between cFbpA and cFbpB. Furthermore, in *C. jejuni* NCTC 11168, cFbpB and two outer membrane proteins (OMPs) encoded by *cfrA* and *cj0178* were shown to facilitate iron acquisition from the transferrin protein family (103); however in *C. jejuni* 81-176, both of these OMPs are absent. Currently, the outer membrane components of the cFbpABC transport system in *C. jejuni* 81-176 are uncharacterized. In addition, the iron sources for the cFbpABC transport system in *C. jejuni* 81-176 are unknown.

Future work can elucidate the iron sources for cFbpA in *C. jejuni* 81-176. The iron sources for cFbpA in *C. jejuni* 81-176 may be identified using limited medium growth assays and radioactive iron uptake assays as described for *C. jejuni* NCTC 11168 (103). Impaired growth of the Δ*cfbpA* mutant compared with the WT strain in defined iron limited medium (minimal essential medium alpha [MEMα]) and supplemented with an iron source (eg. transferrin and lactoferrin) would show that cFbpA facilitates iron acquisition from the iron source. Radioactive iron uptake assays using radiolabelled iron sources (eg. ^{55}Fe-loaded transferrin) may also show acquisition of iron from the iron source.

This thesis also classifies FbpA proteins into six classes. The FbpA members of Classes IV, V, and VI have not been structurally characterized and likely coordinate iron differently than observed for the other classes. Future work can also involve elucidation of the iron binding modes of representative members from Classes IV, V, and VI by x-ray crystallography.

References

1. **Adhikari, P., S. D. Kirby, A. J. Nowalk, K. L. Veraldi, A. B. Schryvers, and T. A. Mietzner.** 1995. Biochemical characterization of a *Haemophilus influenzae* periplasmic iron transport operon. J. Biol. Chem. **270:**25142-25149.
2. **Alexeev, D., H. Zhu, M. Guo, W. Zhong, D. J. B. Hunter, W. Yang, D. J. Campopiano, and P. J. Sadler.** 2003. A novel protein-mineral interface Nat. Struct. Biol **10:**297-302.
3. **Altschul, S. F., W. Gish, W. Miller, E. W. Myers, and D. J. Lipman.** 1990. Basic local alignment search tool. J. Mol. Biol. **215:**403-410.
4. **Anderson, B. F., H. M. Baker, G. E. Norris, S. V. Rumball, and E. N. Baker.** 1990. Apolactoferrin structure demonstrates ligand-induced conformational change in transferrins. Nature **344:**784-787.
5. **Anderson, M. T., and S. K. Armstrong.** 2004. The BfeR regulator mediates enterobactin-inducible expression of *Bordetella* enterobacin utilization genes. J. Bacteriol. **186:**7302-7311.
6. **Anderson, M. T., and S. K. Armstrong.** 2006. The *Bordetella* Bfe system: growth and transcriptional response to siderophores, catechols, and neuroendocrine catecholamines. J. Bacteriol. **188:**5731-5740.
7. **Anderson, M. T., and S. K. Armstrong.** 2008. Norepinepherine mediates acquisition of transferrin-iron in *Bordetella bronchiseptica*. J. Bacteriol. **190:**3940-3947.
8. **Angerer, A., S. Gaisser, and V. Braun.** 1990. Nucleotide sequences of the sfuA, sfuB, and sfuC Genes of *Serratia marcescens* suggest a periplasmic-binding-protein-dependent iron transport mechanism. J. Bacteriol. **172:**572-578.
9. **Angerer, A., B. Klupp, and V. Braun.** 1992. Iron transport systems of Serratia marcescens. J. Bacteriol. **174:**1378-1387.
10. **Bacon, D. J., R. A. Alm, D. H. Burr, L. Hu, D. J. Kopecko, C. P. Ewing, T. J. Trust, and P. Guerry.** 2000. Involvement of a plasmid in virulence of *Campylobacter jejuni* 81-176. Infect Immun. **68:**4384-4390.
11. **Bacon, D. J., R. A. Alm, L. Hu, T. E. Hickey, C. P. Ewing, R. A. Batchelor, T. J. Trust, and P. Guerry.** 2002. DNA sequence and mutational analyses of the pVir plasmid of *Campylobacter jejuni* 81-176. Infect Immun. **70:**6242-6250.
12. **Badarau, A., S. J. Firbank, K. J. Waldron, S. Yanagisawa, N. J. Robinson, M. J. Banfield, and C. Dennison.** 2008. FutA2 is a ferric binding protein from *Synechocystis* PCC 6803. J. Biol. Chem. **283:**12520-12527.
13. **Bakel, H. v., M. Huynen, and C. Wijmenga.** 2004. Prokaryotic diversity of the *Saccharomyces cerevisiae* Atx1p-mediated copper pathway. Bioinformatics **20:**2644-2655.
14. **Baker, E. N.** 1994. Structure and Reactivity of Transferrins. Adv. Inorg. Chem. **41:**389-463.
15. **Baker, E. N., H. M. Baker, and R. D. Kidd.** 2002. Lactoferrin and transferrin: functional variations on a common structural framework. Biochem. Cell Biol. **80:**27-34.

16. **Beall, B., and G. N. Sanden.** 1995. A *Bordetella pertussis* fepA homologue required for utilization of exogenous ferric enterobactin. Microbiology **141:**3193-3205.
17. **Bekker, E. G., A. L. Creagh, N. Sanaie, F. Yumoto, G. H. Y. Lau, M. Tanokura, C. A. Haynes, and M. E. P. Murphy.** 2004. Specificity of the synergistic anion for iron binding by ferric binding protein from *Neisseria gonorrhoeae*. Biochemistry **43:**9195-9203.
18. **Blankenship, R. E.** 2002. Molecular Mechanisms of Photosynthesis. Blackwell Science Ltd, Malden.
19. **Borths, E. L., K. P. Locher, A. T. Lee, and D. C. Rees.** 2002. The structure of *Escherichia coli* BtuF and binding to its cognate ATP binding cassette transporter. Proc Natl Acad Sci USA. **99:**16642-16647.
20. **Boukhalfa, H., D. S. Anderson, T. A. Mietzner, and A. L. Crumbliss.** 2003. Kinetics and mechanism of iron release from bacterial ferric binding protein nFbp: exogenous anion influence and comparison with mammalian transferrin. J. Biol. Inorg. Chem. **8:**881-892.
21. **Bradford, M. M.** 1976. A rapid and sensitive method for the quantitation of microgram quantities of protein utilizing the principle of protein-dye binding. Anal Biochem. **72:**248-254.
22. **Braun, V., and C. Herrmann.** 2007. Docking of the periplasmic FecB binding protein to the FecCD transmembrane proteins in the ferric citrate transport system of *Escherichia coli*. J. Bacteriol. **189:**6913-6918.
23. **Braun, V., and H. Killman.** 1999. Bacterial solutions to the iron-supply problem. TIBS **24:**104-109.
24. **Brickman, T. J., M. T. Anderson, and S. K. Armstrong.** 2007. *Bordetella* iron transport and virulence. Biometals **20:**303-322.
25. **Brickman, T. J., and S. K. Armstrong.** 2005. *Bordetella* AlcS transporter functions in alcaligin siderophore export and is central to inducer sensing in positive regulation of alcaligin system gene expression. J. Bacteriol. **187:**3650-3661.
26. **Brickman, T. J., and S. K. Armstrong.** 1999. Essential role of the iron-regulated outer membrane receptor FauA in alcaligin siderophore-mediated iron uptake in *Bordetella* species. J. Bacteriol. **181:**5958-5966.
27. **Brickman, T. J., J.-G. Hansel, M. J. Miller, and S. K. Armstrong.** 1996. Purification, spectroscopic analysis and biological activity of the macrocyclic dihydroxamate siderophore alcaligin produced by *Bordetella pertussis* and *Bordetella bronchiseptica*. Biometals **9:**191-203.
28. **Brock, J. H., Arzabe, F., Lampreave, F., and Pineiro, A.** 1976. The effect of trypsin on bovine transferrin and lactoferrin. Biochim. Biophys. Acta **446:**214-225.
29. **Brown, J. S., and D. W. Holden.** 2002. Iron acquisition by Gram-positive bacterial pathogens. Microbes and Infection **4:**1149-1156.
30. **Brunger, A. T., P. D. Adams, G. M. Clore, W. L. DeLano, P. Gros, R. W. Grosse-Kunstleve, J.-S. Jiang, J. Kuszewski, M. Nilges, N. S. Pannu, R. J.**

Read, L. M. Rice, T. Simonson, and G. L. Warren. 1998. Crystallography and NMR system: a new software suite for macromolecular structure determination. Acta Crystallogr. D **54:**905-921.

31. **Bruns, C. M., D. S. Anderson, K. G. Vaughan, P. A. Williams, A. J. Norwalk, D. E. McRee, and T. A. Mietzner.** 2001. Crystallographic and biochemical analyses of the metal-free *Haemophilus influenzae* Fe3+ binding protein. Biochemistry **40:**15631-15637.
32. **Bruns, C. M., A. J. Norwalk, A. S. Arvai, M. A. McTigue, K. G. Vaughan, T. A. Mietzner, and D. E. McRee.** 1997. Structure of *Haemophilus influenzae* Fe+3 binding protein reveals convergent evolution within a superfamily. Nat. Struct. Biol. **4:**919-924.
33. **Butzler, J.-P.** 2004. *Campylobacter*, from obscurity to celebrity. Clin. Microbiol. Infect **10:**868-876.
34. **CCP4.** 1994. The CCP4 suite: programs for protein crystallography. Acta Crystallography D **50:**760-763.
35. **Chan, A. C. K., B. Lelj-Garolla, F. I. ROsell, K. A. Pedersen, A. G. Mauk, and M. E. P. Murphy.** 2006. Cofacial heme binding is linked to dimerization by a bacterial heme transport protein. J. Mol. Biol. **362:**1108-1119.
36. **Chen, C. Y., S. A. Berish, S. A. Morse, and T. A. Mietzner.** 1993. The ferric iron-binding protein of pathogenic Neisseria spp. functions as a periplasmic transport protein in iron acquisition from human transferrin. Mol. Microbiol. **10:**311-318.
37. **Chen, J., S. Sharma, F. A. Quiocho, and A. L. Davidson.** 2001. Trapping the transition state of an ATP-binding cassette transporter: evidence for a concerted mechanism of maltose transport. Proc. Natl. Acad. Sci. U S A **98:**1525-1530.
38. **Chin, N., J. Frey, C.-F. Chang, and Y.-F. Chang.** 1996. Identification of a locus involved in the utilization of iron by *Actinobacillus pleuropneumoniae*. FEMS Microbiol. Lett. **143:**1-6.
39. **Clarke, T. E., S.-Y. Ku, D. R. Duncan, H. J. Vogel, and L. W. Tari.** 2000. The structure of the ferric siderophore binding protein FhuD complexed with gallichrome. Nat. Struct. Biol **7:**287-291.
40. **CollaborativeComputationalProjectNumber4.** 1994. The CCP4 Suite: programs for protein crystallography. Acta Crystallogr. D **50:**760-763.
41. **Dhungana, S., D. S. Anderson, T. A. Mietzner, and A. L. Crumbliss.** 2005. Kinetics of iron release from ferric binding protein (FbpA): mechanistic implications in bacterial periplasm- to-cytosol Fe^{3+} transport. Biochemistry **44:**9606-9618.
42. **Dhungana, S., C. H. Taboy, D. S. Anderson, K. G. Vaughan, P. Aisen, T. A. Mietzner, and A. L. Crumbliss.** 2003. The influence of the synergistic anion on iron chelation by ferric binding protein, a bacterial transferrin. Proc. Natl. Acad. Sci. U S A **100:**3659-3664.
43. **Doherty, C. P.** 2007. Host-pathogen interactions: the role of iron. J. Nutr. **137:**1341-1344.

44. **Domenico, I. D., D. M. Ward, and J. Kaplan.** 2008. Regulation of iron acquisition and storage: consequences for iron-linked disorders. Nat Rev Mol Cell Biol. **9:**72-81.
45. **Ferreiros, C., M. T. Criado, and J. A. Gomez.** 1999. The neisserial 37 kDa ferric binding protein (FbpA). Comparative Biochemistry & Physiology. Part B, Biochemistry & Molecular Biology **123:**1-7.
46. **Field, L. H., V. L. Headley, S. M. Payne, and L. J. Berry.** 1986. Influence of iron on growth, morphology, outer membrane protein composition, and synthesis of siderophores in *Campylobacter jejuni*. Infect. Immun. **54:**126-132.
47. **Fontana, A., M. Zambonin, P. P. d. Laureto, V. D. Filippis, A. Clementi, and E. Scaramella.** 1997. Probing the conformational state of apomyoglobin by limited proteolysis. J. Mol. Biol. **266:**223-230.
48. **Gabricevic, M., D. S. Anderson, T. A. Mietzner, and A. L.Crumbliss.** 2004. Kinetics and mechanism of iron (III) complexation by ferric binding protein: the role of phosphate. Biochemistry **43:**5811-5819.
49. **Galindo, M. A., W. A. Day, B. H. Raphael, and L. A. Joens.** 2001. Cloning and characterization of a *Campylobacter jejuni* iron uptake operon. Curr Microbiol. **42:**139-143.
50. **Gaynor, E. C., S. Cawthraw, G. Manning, J. K. MacKichan, S. Falkow, and D. G. Newell.** 2004. The genome-sequenced variant of *Campylobacter jejuni* NCTC 11168 and the original clonal clinical isolate differ markedly in colonization, gene expression, and virulence-associated phenotypes. J. Bacteriol. **186:**503-517.
51. **Ghio, A. J., D. S. Peterseim, V. L. Roggli, and C. A. Piantadosi.** 1992. Pulmonary Oxalate Deposition Associated with *Aspergillus niger* iInfection. An Oxidant Hypothesis of Toxicity. Am. Rev. Respir. Dis. **145:**1499-1502.
52. **Ghio, A. J., V. L. Roggli, J. H. Richards, K. M. Crissman, J. D. Stonehuerner, and C. A. Piantadosi.** 2003. Oxalate Deposition on Asbestos Bodies. Hum. Pathol. **34:**735-736.
53. **Giardina, P. C., L.-A. Foster, S. I. Toth, B. A. Roe, and D. W. Dyer.** 1997. Analysis of the *alcABC* operon encoding alcaligin biosynthesis enzymes in *Bordetella bronchiseptica*. Gene **197:**19-24.
54. **Gorbach, S. L.** 1999. Clostridia, p. 215-216. *In* M. Schaechter, N. C. Engleberg, B. I. Eisenstein, and G. Medoff (ed.), Mechanisms of microbial disease, vol. third edition. Williams and Wilkins, Baltimore.
55. **Gorringe, A. R., G.Woods, and A. Robinson.** 1990. Growth and siderophore production by *Bordetella pertussis* under iron-restricted conditions. FEMS Microbiol. Lett. **66:**101-106.
56. **Grigg, J. C., C. L. Vermeiren, D. E. Heinrichs, and M. E. P. Murphy.** 2007. Heme coordination by *Staphylococcus aureus* IsdE. J. Biol. Chem. **282:**28815-28822.
57. **Grossmann, J. G., M. Neu, E. Pantos, F. J. Schwab, R. W. Evans, E. Townes-Andrews, P. F. Lindley, H. Appel, W. G. Thies, and S. S. Hasnain.** 1992. X-

ray solution scattering reveals conformational changes upon iron uptake in lactoferrin, serum and ovo-transferrins. J. Mol. Biol. **225:**811-819.

58. **Guerry, P., C. M. Szymanski, M. M. Prendergast, T. E. Hickey, C. P. Ewing, D. L. Pattarini, and A. P. Moran.** 2002. Phase variation of *Campylobacter jejuni* 81-176 lipooligosaccharide affects ganglioside mimicry and invasiveness *in vitro*. Infect. Immun. **70:**787-793.
59. **Gutteridge, J. M. C., D. A. Rowley, and B. Halliwell.** 1981. Superoxide-dependent formation of hydrosyl radicals in the presence of iron salts. Biochem. J. **199:**263-265.
60. **Hall, T. A.** 1999. BioEdit: a user-friendly biological sequence alignment editor and analysis program for Windows 95/98/NT. Nucleic Acids Symp. Ser. **41:**95-98.
61. **Hammersley, A. P., S. O. Svensson, M. Hanfland, A. N. Fitch, and D. Hausermann.** 1996. Two-dimensional detector software: From real detector to idealised image or two-theta scan. High Pressure Res. **14:**235-248.
62. **Hayward, S., and R. A. Lee.** 2002. Improvements in the analysis of domain motions in proteins from conformational change: DynDom version 1.50. J. Mol. Graph Model **3:**181-183.
63. **Hendrixson, D. R.** 2006. A phase-variable mechanism controlling the *Campylobacter jejuni* FlgR response regualor influences commensalism. Mol. Microbiol. **61:**1646-1659.
64. **Heymann, J. J., K. D. Weaver, T. A. Mietzner, and A. L. Crumbliss.** 2007. Sulfate as a synergistic anion facilitating iron binding by the bacterial transferrin FbpA: the origins and effects of anion promiscuity. J. Am. Chem. Soc. **129:**9704-9712.
65. **Higgins, D. G., J. D. Thompson, and T. J. Gibson.** 1996. Using CLUSTAL for multiple sequence alignments. Methods Enzymol. **266:**383-409.
66. **Ho, W. W., H. Li, S. Eakanunkul, Y. Tong, A. Wilks, M. Guo, and T. L. Poulos.** 2007. Holo- and apo-bound structures of bacterial periplasmic heme-binding proteins. J. Biol. Chem. **282:**35796-35802.
67. **Hofreuter, D., J. Tsai, R. O. Watson, V. Novik, B. Altman, M. Benitez, C. Clark, C. Perbost, T. Jarvie, L. Du, and J. E. Galan.** 2006. Unique features of a highly pathogenic *Campylobacter jejuni* strain. Infect. Immun. **74:**4694-4707.
68. **Hor, L.-I., and H. A. Shuman.** 1993. Genetic analyses of periplasmic binding protein dependent transport in *Escherichia coli*. Each Lobe of maltose-binding protein interacts with a different subunit of the MalFGK2 membrane transport complex. J. Mol. Biol. **233:**659-670.
69. **Hvorup, R. N., B. A. Goetz, M. Niederer, K. Hollenstein, E. Perozo, and K. P. Locher.** 2007. Asymmetry in the structure of the ABC transporter-binding protein complex BtuCD-BtuF. Science **317:**1387-1390.
70. **Jones, T. A., J.-Y. Zou, S. W. Cowan, and M. Kjeldgaard.** 1991. Improved methods for building protein models in electron density maps and the location of errors in these models. Acta Crystallogr. A **47:**110-119.

71. **Kammler, M., C. Schon, and K. Hankte.** 1993. Characterization of the ferrous iron uptake system in Escherichia coli. Journal of Bacteriology **175:**6212-6219.
72. **Katoh, H., N. Hagino, A. R. Grossman, and T. Ogawa.** 2001. Genes essential to iron transport in the cyanobacterium Synechocystis sp. strain PCC 6803. J. Bacteriol. **183:**2779-2784.
73. **Katoh, H., N. Hagino, and T. Ogawa.** 2001. Iron-binding affinity of FutA1 subunit of an ABC-type transporter in the cyanobacterium *Synechocystis* sp. strain PCC 6803. Plant Cell Physiol. **42:**823-827.
74. **Ketley, J. M.** 1997. Pathogenesis of enteric infection by *Campylobacter*. Microbiol. **143:**5-21.
75. **Khan, A. G., S. R. Shouldice, S. D. Kirby, R.-h. Yu, L. W. Tari, and A. B. Schryvers.** 2007. High-affinity binding by the periplasmic iron-binding protein from *Haemophilus influenzae* is required for acquiring iron from transferrin. Biochem. J. **404:**217-225.
76. **Khan, A. G., S. R. Shouldice, L. W. Tari, and A. B. Schryvers.** 2007. The role of the synergistic phosphate anion in iron transport by the periplasmic iron-binding protein from *Haemophilus influenzae*. Biochem. J. **403:**43-48.
77. **Khun, H. H., S. D. Kirby, and B. C. Lee.** 1998. A *Neisseria meningitidis fbpABC* mutant is incapable of using nonheme iron for growth. Infect. Immun. **66:**2330-2336.
78. **Kirby, S. D., S. D. Gray-Owen, and A. B. Schryvers.** 1997. Characterization of a ferric-binding protein mutant in *Haemophilus influenzae*. Mol. Microbiol. **25:**979-87.
79. **Kirby, S. D., F. A. Lainson, W. Donachie, A. Okabe, M. Tokuda, O. Hatase, and A. B. Schryvers.** 1998. The *Pasteurella haemolytica* 35 kDa iron-regulated protein is an FbpA homologue. Microbiology **144:**3425-36.
80. **Kirillina, O., A. G. Bobrov, J. D. Fetherston, and R. D. Perry.** 2006. Hierarchy of iron uptake systems: Yfu and Yiu are functional in *Yersinia pestis*. Infect. Immun. **74:**6171-6178.
81. **Klein, D. L.** 2000. From pertussis to tuberculosis: what can be learned? Clin Infect Dis. **30:**S302-S308.
82. **Konkel, M. E., B. J. Kim, V. Rivera-Amill, and S. G. Garvis.** 1999. Bacterial secreted proteins are required for the internalization of Campylobacter jejuni into cultured mammalian cells. Mol. Microbiol. **32:**691-701.
83. **Konkel, M. E., and K. Tilly.** 2000. Temperature-regulated expression of bacterial virulence genes. Microbes Infect. **2:**157-166.
84. **Kopecko, D. J., L. Hu, and K. J. M. Zaal.** 2001. *Campylobacter jejuni* - microtubule dependent invasion. Trends Microbiol. **9:**389-396.
85. **Korlath, J. A., M. T. Osterholm, L. A. Judy, J. C. Forfang, and R. A. Robinson.** 1985. A point-source outbreak of campylobacteriosis associated with consumption of raw milk. J. Infect. Dis. **152:**592-596.
86. **Koropatkin, N., A. M. Randich, M. Bhattacharyya-Pakrasi, and H. B. Pakrasi.** 2007. The structure of the iron-binding protein, FutA1, from *Synechocystis* 6803. J. Biol. Chem. **282:**27468-27477.

87. **Kraulis, P.** 1991. MOLSCRIPT, a program to produce both detailed and schematic plots of protein structures. J. Appl. Crystallogr. **24:**946-950.
88. **Kreimer, D. I., H. Malak, J. R. Lakowicz, S. Trakhanov, E. Villar, and V. L. Shnyrov.** 2000. Thermodynamics and dynamics of histidine-binding protein, the water-soluble receptor of histidine permease. Eur. J. Biochem. **267:**4242-4252.
89. **Krewulak, K. D., C. M. Shepherd, and H. J. Vogel.** 2005. Molecular dynamics simulations of the periplasmic ferric-hydroxamate binding protein FhuD. BioMetals **18:**375-386.
90. **Kuser, P., D. R. Hall, M. L. Haw, M. Neu, R. W. Evans, and P. F. Lindley.** 2002. The mechanism of iron uptake by transferrins: the X-ray structures of the 18kDa NII domain fragment of duck ovotransferrin and its nitrilotriacetate complex. Acta Crystallogr. D **58:**777-783.
91. **Laskowski, R. A., M. W. MacArthur, D. S. Moss, and J. M. Thornton.** 1993. PROCHECK: a program to check the stereochemical quality of protein structures. J. Appl. Cryst. **26:**283-291.
92. **Lau, G. H. Y., R. T. A. MacGillivray, and M. E. P. Murphy.** 2004. Characterization of a nucleotide-binding domain associated with neisserial iron transport. J. Bacteriol. **186:**3266-3269.
93. **Lee, J.-W., and J. D. Helmann.** 2007. Functional specialization within the Fur family of metalloregulators. Biometals **20:**485-499.
94. **Liu, C. E., P.-Q. Liu, A. Wolf, E. Lin, and G. F.-L. Ames.** 1999. Both lobes of the soluble receptor of the periplasmic histidine permease, an ABC transporter (traffic ATPase), interact with the membrane-bound complex. J. Biol. Chem. **274:**739-747.
95. **Lu, G., J. M. Westbrooks, A. L. Davidson, and J. Chen.** 2005. ATP hydrolysis is required to reset the ATP-binding cassette dimer into the resting -state conformation. Proc. Natl. Acad. Sci. U S A **102:**17969-74.
96. **MacGillivray, R. T., S. A. Moore, J. Chen, B. F. Anderson, H. Baker, Y. Luo, M. Bewley, C. A. Smith, M. E. Murphy, Y. Wang, A. B. Mason, R. C. Woodworth, G. D. Brayer, and E. N. Baker.** 1998. Two high-resolution crystal structures of the recombinant N-lobe of human transferrin reveal a structural change implicated in iron release. Biochemistry **37:**7919-7928.
97. **Marlovits, T. C., W. Haase, C. Herrmann, S. G. Aller, and V. M. Unger.** 2002. The membrane protein FeoB contains a intramolecular G protein essential for Fe(II) uptake in bacteria. Proc Natl Acad Sci USA. **99:**16243-16248.
98. **Menard, R., P. J. Sansonetti, and C. Parsot.** 1993. Nonpolar mutagenesis of the *ipa* genes defines IpaB, IpaC, and IpaD as effectors of *Shigella flexneri* entry into epithelial cells. J. Bacteriol. **175:**5899-5906.
99. **Merritt, E. A., and D. J. Bacon.** 1997. Raster3D: Photorealistic Molecular Graphics. Method. Enzymol. **277:**505-524.
100. **Michel, L.-P., and E. K. Pistorius.** 2004. Adaptation of the photosynthetic electron transport chain in cyanobacteria to iron deficiency: The function of IdiA and IsiA. Physiol. Plantarum **120:**36-50.

101. **Miethke, M., and M. A. Marahiel.** 2007. Siderophore-based iron acquisition and pathogen control. Microbiol Mol Biol Rev. **71:**413-451.
102. **Mietzner, T. A., S. B. Teneza, P. Adhikari, K. G. Vaughan, and A. J. Nowalk.** 1998. Fe(III) periplasm-to-cytoplasm transporters of Gram-negative pathogens. Curr. Top. Microbiol. **225:**113-135.
103. **Miller, C. E., J. D. Rock, K. A. Ridley, P. H. Williams, and J. M. Ketley.** 2008. Utilization of lactoferrin-bound and transferrin-bound iron by *Campylobacter jejuni*. J. Bacteriol. **190:**1900-1911.
104. **Muller, A., A. J. Wilkinson, K. S. Wilson, and A.-K. Duhme-Klair.** 2006. An $[\{Fe(mecam)\}]^{6-}$ bridge in the crystal structure of a ferric enterobactin binding protein. Angew. Chem. **118:**5256-5260.
105. **Murshudov, G. N., A. A. Vagin, and E. J. Dodson.** 1997. Refinement of macromolecular structures by the maximum-likelihood method. Acta Crystallogr. D **53:**240-255.
106. **Nachamkin, I., B. M. Allos, and T. Ho.** *1998. Campylobacter* species and Guillain-Barre syndrome. Clin. Microbiol. Rev. **11:**555-567.
107. **Naikare, H., K. Palyada, R. Panciera, D. Marlow, and A. Stintzi.** 2006. Major role for FeoB in *Campylobacter jejuni* ferrous iron acquisition, gut colonization, and intracellular survival. Infect. Immun. **74:**5433-5444.
108. **Nowalk, A. J., S. B. Tencza, and T. A. Mietzner.** 1994. Coordination of iron by the ferric iron-binding protein of pathogenic Neisseria is Homologous to the transferrins. Biochemistry **33:**12769-12775.
109. **Nowalk, A. J., K. G. Vaughan, B. W. Day, S. B. Tencza, and T. A. Mietzner.** 1997. Metal-dependent conformers of the periplasmic ferric ion binding protein. Biochemistry **36:**13054-13059.
110. **O'Brien, D. K., and S. B. Melville.** 2000. The anaerobic pathogen Clostridium perfringens can escape the phagosome of macrophages under aerobic conditions. Cell Microbiol. **2:**505-519.
111. **Oldham, M. L., D. Khare, F. A. Quiocho, A. L. Davidson, and J. Chen.** 2007. Crystal structure of a catalytic intermediate of the maltose transporter. Nature **450:**515-521.
112. **Ollinger, J., K.-B. Song, H. Antelmann, M. Hecker, and J. D. Helmann.** 2006. Role fo the Fur regulon in iron transport in *Bacillus subtilis*. J. Bacteriol. **188:**3664-3673.
113. **Otwinowski, Z., and W. Minor.** 1997. Processing of X-ray diffraction data collected in oscillation mode. Method. Enzymol. **276:**307-326.
114. **Page, R. D. W.** 1996. TreeView: An application to display phylogenetic trees on personal computers. Comput. Appl. Biosci. **12:**357-358.
115. **Palyada, K., D. Threadgill, and A. Stintzi.** 2004. Iron acquisition and regulation in *Campylobacter jejuni*. J. Bacteriol. **186:**4714-4729.
116. **Parkhill, J., M. Sebaihia, A. Preston, L. D. Murphy, N. Thomson, D. E. Harris, M. T. Holden, C.M.Churcher, S. D. Bentley, K. L. Mungall, A. M. Cerdeño-Tárraga, L. Temple, K. James, B. Harris, M. A. Quail, M. Achtman, R. Atkin, S. Baker, D. Basham, N. Bason, I. Cherevach, T.**

Chillingworth, M. Collins, A. Cronin, P. Davis, J. Doggett, T. Feltwell, A. Goble, N. Hamlin, H. Hauser, S. Holroyd, K. Jagels, S. Leather, S. Moule, H. Norberczak, S. O'Neil, D. Ormond, C. Price, E. Rabbinowitsch, S. Rutter, M. Sanders, D. Saunders, K. Seeger, S. Sharp, M. Simmonds, J. Skelton, R. Squares, S. Squares, K. Stevens, L. Unwin, S. Whitehead, B. G. Barrell, and D. J. Maskell. 2003. Comparative analysis of the genome sequences of *Bordetella pertussis*, *Bordetella parapertussis* and *Bordetella bronchiseptica*. Nat Genet. **35:**32-40.

117. **Patch, M. G., and C. J. Carrano.** 1981. The origin of the visible absorption in metal transferrins. Inorg. Chim. Acta **56:**71-73.
118. **Pickett, C. L., T. Auffenberg, E. C. Pesci, V. L. Sheen, and S. S. Jusuf.** 1992. Iron acquisition and hemolysin production by Campylobacter jejuni. Infection and Immunity **60:**3872-3877.
119. **Poly, F., D. Threadgill, and A. Stintzi.** 2005. Genomic diversity in *Campylobacter jejuni*: identification of *C. jejuni* 81-176-specific genes. J. Clin. Microbiol. **43:**2330-2338.
120. **Pradel, E., N. Guiso, and C. Locht.** 1998. Identification of AlcR, an AraC-type regulator of alcaligin siderophore synthesis in *Bordetella bronchiseptica* and *Bordetella pertussis*. J. Bacteriol. **180:**871-880.
121. **Pradel, E., N. Guiso, F. D. Mennozi, and C. Locht.** 2000. *Bordetella pertussis* TonB, a Bvg-independent virulence determinant. Infection and Immunity **68:**1919-1927.
122. **Quiocho, F. A., and P. S. Ledvina.** 1996. Atomic structure and specificity of bacterial periplasmic receptors for active transport and chemotaxis: variation of common themes. Mol. Microbiol. **20:**17-25.
123. **Ratledge, C., and L. G. Dover.** 2000. Iron metabolism in pathogenic bacteria. Annu. Rev. Microbiol. **54:**881-941.
124. **Redhead, K., and T. Hill.** 1991. Acquisition of iron from transferrin by *Bordetella pertussis*. FEMS Microbiol. Lett. **77:**303-308.
125. **Richardson, P. T., and S. F. Park.** 1995. Enterochelin acquisition in Campylobacter coli: characterization of components of a binding protein-dependent transport system. Microbiology **141:**3181-3191.
126. **Ridley, K. A., J. D. Rock, Y. Li, and J. M. Ketley.** 2006. Heme utilization in *Campylobacter jejuni*. J. Bacteriol. **188:**7862-7875.
127. **Rock, J. D., A. H. M. v. Vliet, and J. M. Ketley.** 2001. Haemin uptake in *Campylobacter jejuni*. Int. J. Med. Microbiol. **291:**125.
128. **Rosa, M. C. D., C. C. Alinovi, A. Galtieri, A. Russo, and B. Giardina.** 2008. Allosteric properties of hemoglobin and the plasma membrane of the erythrocyte: new insights in gas transport and metabolic modulation. IUBMB Life **60:**87-93.
129. **Roulhac, P. L., K. D. Weaver, P. Adhikari, D. S. Anderson, P. D. DeArmond, T. A. Meitzner, A. L. Crumbliss, and M. C. Fitzgerald.** 2008. *Ex vivo* analysis of synergistic anion binding to FbpA in Gram-negative bacteria. Biochemistry **47:**4298-4305.

130. **Sanders, J. D., L. D. Cope, and E. J. Hansen.** 1994. Identification of a Locus Involved in Utilization of Iron by Haemophilus influenzae. Infection & Immunity **62:**4515-4525.
131. **Schaechter, M., N. C. Engleberg, B. I. Eisenstein, and G. Medoff.** 1999. *Bordetella pertussis* and whooping cough, 3 ed. Lippencott Williams and Williams, Philadelphia.
132. **Schmidt, H. A., K. Strimmer, M. Vingron, and A. v. Haeseler.** 2002. TREE-PUZZLE: maximum likelihood phylogenetic analysis using quartets and parallel computing. Bioinformatics **18:**502-504.
133. **Schroder, I., E. Johnson, and S. d. Vries.** 2003. Microbial ferric iron reductases. FEMS Microbiol Rev. **27:**427-447.
134. **Schryvers, A. B., and I. Stojiljkovic.** 1999. Iron acquisition systems in the pathogenic *Neisseria*. Mol. Microbiol. **32:**117-123.
135. **Schwede, T., J. Kopp, N. Guex, and M. C. Peitsch.** 2003. SWISS-MODEL: an automated protein homology-modeling server. Nucleic Acids Res. **31:**3381-3385.
136. **Sclabach, M. R., and G. W. Bates.** 1975. The synergistic binding of anions and Fe3+ by transferrin. J. Biol. Chem. **250:**2182-2188.
137. **Sebastian, S., and C. A. Genco.** 1999. FbpC is not essential for iron acquisition in Neisseria gonorrhoeae. Infection & Immunity **67:**3141-5.
138. **Shilton, B. H., M. M. Flocco, M. Nilsson, and S. L. Mowbray.** 1996. Conformational changes of three periplasmic receptors for bacterial chemotaxis and transport: the maltose-, glucose/galactose- and ribose-binding proteins. J. Mol. Biol. **264:**350-363.
139. **Shilton, B. H., H. A. Shuman, and S. L. Mowbray.** 1996. Crystal structures and solution conformations of a dominant-negative mutant of *Escherichia coli* maltose-binding protein. J. Mol. Biol. **264:**364-376.
140. **Shouldice, S. R., D. R. Dougan, R. J. Skene, L. W. Tari, D. E. McRee, R.-h. Yu, and A. B. Schryvers.** 2003. High resolution structure of an alternate form of the ferric ion binding protein from *Haemophilus influenzae*. J. Biol. Chem. **278:**11513-11519.
141. **Shouldice, S. R., D. R. Dougan, P. A. Williams, R. J. Skene, G. Snell, D. Scheibe, S. Kirby, D. J. Hosfield, D. E. McRee, A. B. Schryvers, and L. W. Tari.** 2003. Crystal Structure of *Pasteurella haemolytica* Ferric binding protein A reveals a novel class of bacterial iron-binding proteins. J. Biol. Chem. **278:**41093-41098.
142. **Shouldice, S. R., D. E. McRee, D. R. Dougan, L. W. Tari, and A. B. Schryvers.** 2005. Novel anion-independent iron coordination by members of a third class of bacterial periplasmic ferric ion-binding proteins. J. Biol. Chem. **280:**5820-5827.
143. **Shouldice, S. R., R. J. Skene, D. R. Dougan, D. E. McRee, L. W. Tari, and A. B. Schryvers.** 2003. Presence of ferric hydroxide clusters in mutants of *Haemophilus influenzae* ferric-ion binding protein A. Biochemistry **42:**11908-11914.

144. **Shouldice, S. R., R. J. Skene, D. R. Dougan, G. Snell, D. E. McRee, A. B. Schryvers, and L. W. Tari.** 2004. Structural basis for iron binding and release by a novel class of periplasmic iron binding proteins found in Gram-negative pathogens. J. Bacteriol. **186:**3903-3910.
145. **Studier, F. W., and B. A. Moffatt.** 1986. Use of bacteriophage T7 RNA polymerase to direct selective high-level expression of cloned genes. J. Mol. Biol. **189:**113-130.
146. **Svergun, D. I., C. Barberato, and M. H. J. Koch.** 1995. CRYSOL - a program to evaluate X-ray solution scattering of biological macromolecules from atomic coordinates. J. Appl. Crystallogr. **28:**768-773.
147. **Svergun, D. I., and M. H. J. Koch.** 2003. Small-angle scattering studies of biological macromolecules in solution. Rep. Prog. Phys. **66.**
148. **Tam, R., and M. H. Saier.** 1993. Structural, functional, and evolutionary relationships among extracellular solute-binding receptors of bacteria. Microbiol. Rev. **57:**320-346.
149. **Telmer, P. G., and B. H. Shilton.** 2003. Insights into the conformational equilibria of maltos- binding protein by analysis of high affinity mutants. J. Biol. Chem. **278:**34555-34567.
150. **Terwilliger, T. C., and J. Berendzen.** 1999. Automated MAD and MIR structure solution. Acta Crystallogr. D **55:**849-861.
151. **Thompson, J. D., D. G. Higgins, and T. J. Gibson.** 1994. CLUSTAL W: improving the sensitivity of progressive multiple sequence alignment through sequence weighting, position-specific gap penalties and weight matrix choice. Nucleic Acids Research **22:**4673-80.
152. **Tolle, J., K.-P. Michel, J. Kruip, U. Kahmann, A. Preisfeld, and E. K. Pistorius.** 2002. Localization and function of the idiA homologue Slr1295 in the cyanobacterium Synechocystis sp. strain PCC 6803. Microbiology **148:**3293-3305.
153. **Tom-Yew, S. A. L., D. T. Cui, E. G. Bekker, and M. E. P. Murphy.** 2005. Anion-independent iron coordination by the *Campylobacter jejuni* ferric binding protein. J. Biol. Chem. **280:**9283-9290.
154. **Tsolis, R. M., A. J. Baumler, F. Heffron, and I. Stojiljkovic.** 1996. Contribution of TonB- and Feo-mediated iron uptake to growth of *Salmonella typhimurium* in the mouse. Infect. Immun. **64:**4549-4556.
155. **Vagin, A., and A. Teplyakov.** 1997. MOLREP: an automated program for molecular replacement. J. Appl. Crystallogr. **30:**1022-1025.
156. **Van Duyne, G. D., R. F. Standaert, P. A. Karplus, S. L. Schreiber, and J. Clardy.** 1993. Atomic structures of the human immunophilin FKBP-12 complexes with FK506 and rapamycin. J. Mol. Biol. **229:**105-124.
157. **Vanderpool, C. K., and S. K. Armstrong.** 2001. The *Bordetella bhu* locus is required for heme iron utilization. J. Bacteriol. **183:**4278-4287.
158. **Vliet, A. H. M. v., J. M. Ketley, S. F. Park, and C. W. Penn.** 2002. The role of iron in *Campylobacter* gene regulation, metabolism and oxidative stress defense. FEMS Microbiol Rev. **26:**173-186.

159. **Vliet, A. H. M. V., A. C. Wood, K. Wooldridge, J. M. Ketley, and J. Henderson.** 1998. Genetic manipulation of enteric *Camplobacter* species. Method Microbiol. **27:**407-419.
160. **Weinberg, E. D.** 1978. Iron and infection. Microbiol. Mol. Biol. Rev. **42:**45-66.
161. **Wilkinson, A. J., and K. H. G. Verschueren.** 2003. Crystal structures of periplasmic solute-binding proteins in ABC transport complexes illuminate their function, p. 187 - 209. *In* I. B. Holland, S. P. C. Cole, K. Kuchler, and C. F. Higgins (ed.), ABC proteins from bacteria to man. Elsevier Science Ltd.
162. **Wilks, A., and K. A. Burkhard.** 2007. Heme and virulence: how bacterial pathogens regulate, transport and utilize heme. Nat. Prod. Rep. **24:**511-522.
163. **Wolf, A., K. C. Lee, J. F. Kirsch, and G. F.-L. Ames.** 1996. Ligand-dependent conformational plasticity of the periplasmic histidine-binding protein HisJ. J. Biol. Chem. **271:**21243-21250.
164. **Wooldridge, K. G., and J. M. Ketley.** 1997. Campylobacter-host cell interactions. Trends Microbiol. **5:**96-102.
165. **Young, K. T., L. M. Davis, and V. J. DiRita.** 2007. *Campylobacter jejuni*: molecular biology and pathogenesis. Nat. Rev. Microbiol. **5:**665-679.
166. **Zhang, Y., D. E. Mannering, A. L. Davidson, N. Yao, and M. D. Manson.** 1996. Maltose-binding protein containing an interdomain disulfide bridge confers a dominant-negative phenotype for transport and chemotaxis. J. Biol. Chem. **271:**17881-17889.
167. **Zhu, M., M. Valdebenito, G. Winkelmann, and K. Hantke.** 2005. Functions of the siderophore esterases IroD and IroE in iron-salmochelin utilization. Microbiology **151:**2363-2372.

Appendix I: Co-authorship Statement

Scientific collaborations have provided valuable support for the research conducted in this thesis. Below is a summary of the contributions from other scientists.

The majority of chapter 3 was largely published in: **Tom-Yew, S. A. L., D. T. Cui, E. G. Bekker, and M. E. P. Murphy.** 2005. Anion-independent iron coordination by the *Campylobacter jejuni* ferric binding protein. J. Biol. Chem. **280:**9283-9290. The cloning, protein expression and purification and crystallization of cFbpA were accomplished by Diana T. Cui. I solved the as isolated cFbpA crystal structure. Visible spectroscopic characterization was conducted by Diana T. Cui and Dr. Elena G. Bekker. I conducted the phylogenetic analyses of FbpA proteins. I also prepared the initial draft of the manuscript and all figures. All co-authors read the manuscript and provided valuable feedback.

Chapter 4 is a modified draft of a manuscript that will be submitted as: **Tom-Yew, S. A. L., Shilton, B. H., Bekker, E. G., Gaynor, E. C. and M. E. P. Murphy.** Small hinge motion by the anion-independent ferric binding protein from *Campylobacter jejuni*. Dr. Elena G. Bekker cloned the *cFbpA* disruption construct in pBluescript. I performed all of the work involving manipulations of *C. jejuni* 81-176, including construction of the Δ*cfbpA* strain, reverse transcription PCR experiments and iron-limited growth studies of the Δ*cfbpA* and WT strains. I conducted all of the work with *C. jejuni* 81-176 in the laboratory of Dr. E. C. Gaynor. Introduction to working with *C. jejuni* was provided by Dr. E. C. Gaynor and members of her lab, including Heather Candon, Sarah Svensson and Meghan McLennan. Dr. Elena G. Bekker crystallized and solved the

structure of iron reconstituted cFbpA. I prepared the SAXS nFbpA and cFbpA protein samples. Dr. Brian Shilton collected the SAXS data and conducted initial analyses. I further analysed the SAXS data, prepared SAXS models and modeled the SAXS data. I wrote the initial draft of this manuscript, prepared all figures and have received valuable feedback from all co-authors.

Chapter 5 is a modified draft of a manuscript that will be submitted as **Tom-Yew, S. A. L., Shilton, B. H., Bekker, E. G., Tocheva, E. I. and M. E. P. Murphy.** Influence of synergistic anions on conformation of the ferric binding protein from *Bordetella pertussis*. Dr. Rachel Fernandez supplied the *B. pertussis* Tohama I genomic DNA. Dr. Elitza Tocheva cloned the bFbpA gene into pBluescript. Using the pBluescript construct containing the bFbpA gene, I cloned the bFbpA gene into the expression vector pET28a(+). I also expressed and purified the bFbpA protein. I conducted the visible spectroscopic analyses and affinity experiments of bFbpA. Dr. Elena G. Bekker offered helpful advice for the visible spectroscopic experiments. I also prepared, crystallized and collected x-ray data for the SeMet incorporated apo bFbpA, apo bFbpA, bFbpA:Fe:carbonate, and bFbpA:Fe:oxalate protein samples. I solved all of the crystal structures. Dr. Michael E. P. Murphy helped in the determination of the initial phases for the SeMet incorporated apo bFbpA crystal structure. I also prepared all of the protein samples for SAXS. Dr. Brian H. Shilton collected the data and performed initial analyses. I further analysed the SAXS data, prepared SAXS models and modeled the SAXS data. I wrote the initial draft of this manuscript, prepared all figures and have received valuable feedback from all co-authors.